

Doctoral Dissertation

博士論文

Milligram-Scale Optomechanical Systems for Macroscopic Quantum Experiments

(巨視的量子実験のためのミリグラムスケール機械光学系)

A Dissertation Submitted for the Degree of Doctor of Philosophy
December 2021

令和3年12月 博士(理学) 申請

Department of Physics, Graduate School of Science, The University of Tokyo

東京大学大学院理学系研究科物理学専攻

Takuya Kawasaki

川崎 拓也

Abstract

Milligram-scale optomechanical systems are unique systems that have the potential to realize macroscopic yet quantum phenomena. To achieve a sensitivity that reaches the dominant region of quantum mechanics, we propose a system in which the optical radiation pressure traps the mirror in the rotational degrees of freedom even in a suspended linear cavity, and a high power laser beam can be coupled to it.

An optomechanical system consists of mechanical oscillators and optical fields coupled to it. It is suitable for macroscopic quantum experiments because even a macroscopic oscillator's displacements can be read out with a precision greater than the wavelength of light. As mechanical oscillators, pendulums are often used above the milligram scale since they are resistant to environmental vibrations.

However, when a linear cavity is built with a suspended mirror, the rotational motion of the mirrors become unstable due to the optical radiation pressure inside the cavity, a phenomenon known as Sidles-Sigg instability. To avoid the Sidles-Sigg instability, experiments were conducted using triangular cavities or rigid suspensions that reduce the effect of radiation pressure. However, quantum fluctuation was concealed by thermal noise in the complicated part of the system. Linear cavities consisting of only two mirrors are advantageous for high sensitivity reaching the quantum fluctuation.

In this research, we find that even in a linear cavity, the Sidles-Sigg instability can be overcome if the masses of the two mirrors are unbalanced and the curvatures of the mirrors are shorter than the cavity length. We succeed in constructing a linear cavity with the smallest suspended mirror with curvature. Our optomechanical system becomes a highly sensitive force sensor by using a tiny 8-mg mirror as a test mass. With this system, we quantitatively evaluate the optical torsional spring effect due to the radiation pressure in the cavity, and validate our configuration. Furthermore, we demonstrate a quantum noise reduction technique by injecting classical intensity noise that imitates quantum noise. Improvements in the sensitivity are observed, and they are consistent with theoretical predictions. In addition, as a prospect for improving the sensitivity of our system towards the quantum regime, we discuss the idea of modifying the simple pendulum to a torsional pendulum, and show its promise. As a consequence, we establish a class of linear cavities, and present that these systems are competent for

macroscopic quantum experiments.

Thesis Supervisor: Masaki Ando (Associate Professor)

Thesis Title: Milligram-Scale Optomechanical Systems for Macroscopic Quantum Experiments

要旨

ミリグラムスケールの機械光学系は、巨視的でありながら量子的な現象を実現できる可能性をもつ特異な系である。量子力学が支配的な領域に到達する感度をえるため我々は、懸架された線形共振器であっても光輻射圧がねじれ方向に鏡をトラップし、ハイパワーのレーザー光を結合させることが可能な系を提案した。

そもそも機械光学系は、機械振動子とそれに結合する電磁場からなる系である。巨視的な振動子の変位であっても、光の波長以上の精度で読み出すことができるので、巨視的な量子実験に適している。ミリグラムスケール以上の機械光学系では、環境的な振動雑音に強い機械振動子として、振り子がよく使われる。しかしながら、懸架された鏡をもちいて線形光共振器を構成すると、共振器内の光輻射圧により、鏡の回転運動が不安定になる現象が、Sidles-Sigg 不安定性という名前で知られている。これまで、Sidles-Sigg 不安定性を回避するために三角共振器をもちいた系や、懸架を強固にして輻射圧の影響を小さくする系での実験がおこなわれてきたが、系をより複雑にしたことに起因する熱雑音により、量子ゆらぎが覆い隠されていた。量子ゆらぎにせまるまでの感度のためには、2つの鏡のみからなる線形共振器が有利である。そこで本研究では、線形共振器であっても、構成する2つの鏡の質量が偏っていて、かつ鏡の曲率が共振器長よりも短いような構成では、Sidles-Sigg 不安定を克服できることを見いだした。実際に我々は、考案した構成により、世界最小の曲率つき懸架鏡をもちいて線形光共振器を構築することに成功した。この機械光学系は、8 mg の微小な鏡がテストマスとなることにより、高感度の力センサーとなる。構築した機械光学系をもちいて、共振器内の輻射圧がねじれ方向に対してばね的にふるまうことを定量的に評価し、構成の有効性を実証した。さらにこの系をもちいて、量子雑音を低減する手法を、量子雑音にもした古典的な強度雑音を注入するという方法でデモンストレーションし、理論的な予測と矛盾しない感度の向上を観測した。加えて、我々の系を量子領域の感度に向上させるための展望として、振り子をねじれ振り子に変更する案を議論し、その有用性を示した。以上の研究により我々は、今までミリグラムスケールでは困難であった線形共振器の構成を確立し、その系が量子実験にふさわしいことを示した。

指導教員：安東正樹（准教授）

論文題目：巨視的量子実験のためのミリグラムスケール機械光学系

Acknowledgements

This work has been supported by many people. I would like to express my appreciation for it.

I am grateful to my supervisor Masaki Ando for his continuous support. He organizes the laboratory and provides suitable environment for laboratory members to concentrate their researches. Through my research life, He gave me a lot of insightful advice. He was kind enough to help me whenever I was struggling.

I am also grateful to Yuta Michimura, an associate professor of Ando laboratory, for various supports. He have been taken care of me since I was an undergraduate student. Also, I visited foreign laboratories with him, and his active footwork in research inspired me.

Kentaro Komori is the catalyst for this research. He gave me a lot of advice for this experiment even when he worked at MIT and JAXA. Without him, this work had never been accomplished.

I am grateful to Koji Nagano, who is the former member of Ando laboratory. When I joined the laboratory, I was engaged in the research project he was doing. He taught me all basic techniques of optical experiments. I am also grateful to Shotaro Wada, who is the former member of Ando laboratory. He was also leading the research project with Koji Nagano, and he was kindly doing the experiment with me.

I also thank our group members. Ching Pin Ooi is not only familiar with his research, but also familiar with cosmology. I had many discussions with him, and they were always fun. I would like to thank him deeply. Satoru Takano have been a colleague in the same year in our group. I talked with him so many times about my questions, his ideas, and so on. I was lucky to have a chance to work with him in the same group. Yuki Fujimoto is a talented colleague. He is sincere in physics, and his keen calculations frequently helped my research. Yuka Oshima always proceed with experiments steadily. I respect her earnestness. Masaya Ono was a new member of our group, and he kindly shared his interesting topics of research.

Shigemi Otsuka and Togo Shimozawa in the machine shop made mechanical parts for the experiment. They also advised me on the design of the parts.

I thank Mayuko Niwata and Kyoko Tanaka for the office work. They were so resourceful that I could maintain my comfortable research environment.

I have been financially supported by Japan Society for the Promotion of Science (JSPS)

fellowship DC1. This work was supported by KAKENHI Grant No. 19J21861 from JSPS.

Takuro Ideguchi, Katsuaki Asano, Masamitsu Hayashi, Shinji Miyoki, and Norikatsu Mio were referees of the dissertation. I would like to thank their insightful comments.

Some illustrations in the dissertation are drawn with the component library by Alexander Franzen.

Finally, I would like to thank my parents, who have been always with me. They have been supported my entire life. They gave me opportunities to do what I want to do, and actually I did whatever I desired. I sincerely thank them.

Please note that this research was also supported by many other people, whom this margin is too narrow to contain.

Contents

Glossary	xiii
1. Introduction	1
2. Optomechanical system	5
2.1. Concepts	5
2.2. Noise sources	6
2.2.1. Quantum noise	6
2.2.2. Thermal noise	6
2.2.3. Other noises	8
2.3. Uses for macroscopic quantum experiments	9
2.3.1. Testing macroscopic quantum mechanics	10
2.3.2. Platform for demonstrating advanced technologies in gravitational wave detectors	11
2.4. Previous works	12
2.4.1. Observation of quantum radiation pressure fluctuation	12
2.4.2. Impediments to improvement of the sensitivity at milligram scale	13
2.5. Summary of this chapter	14
3. Quantum noise in optomechanical systems	17
3.1. Conceptual overview of quantum noise	17
3.1.1. Quantum shot noise	17
3.1.2. Quantum radiation pressure noise	17
3.1.3. Standard Quantum Limit	18
3.2. Quantized electromagnetic fields	19
3.2.1. Quantization of electromagnetic fields	19
3.2.2. Two photon formalism	21
3.2.3. Quantum states of the optical field	23
3.3. Optomechanical systems	24
3.3.1. Dynamics of the electromagnetic field	25

3.4. Modeling of a linear cavity	26
3.4.1. Free mass mirror	27
3.4.2. Linear cavity	28
3.5. Summary of this chapter	31
4. Experimental setup	33
4.1. Design of the experiment	33
4.1.1. Goal and the paths	33
4.1.2. 8-mg mirror as the test mass	34
4.1.3. Design sensitivity	34
4.1.4. Overview of the setup	37
4.2. Main cavity	38
4.2.1. Test mass mirror	38
4.2.2. Controlled input mirror	41
4.2.3. Cavity properties	44
4.3. Auxiliary optics	44
4.3.1. Input optics	44
4.3.2. Output optics	45
4.4. Feedback controls	46
4.4.1. Laser frequency stabilization	46
4.4.2. Laser intensity stabilization	47
4.5. Environmental-noise isolation	47
4.5.1. Vibration isolation	47
4.5.2. Vacuum system	49
4.6. Summary of this chapter	49
5. Angular trapping of a linear-cavity mirror with an optical torsional spring	51
5.1. Preface	51
5.2. Theoretical description of the trapping scheme	51
5.3. Experimental demonstration	55
5.3.1. Method	56
5.3.2. Results and discussion	57
5.4. Summary of this chapter	60
6. Proof-of-principle demonstration of quantum noise cancellation	61
6.1. Preface	61
6.2. Principle of quantum noise cancellation	61

6.3. Proof-of-principle experiment	67
6.3.1. Method	67
6.3.2. Result	68
6.3.3. Discussion	70
6.4. Summary of this chapter	73
7. Prospects for observing quantum radiation pressure fluctuation: the torsional pendulum	75
7.1. Sensitivity with the simple pendulum	75
7.1.1. Current sensitivity with the simple pendulum	75
7.1.2. Estimation of the quantum radiation pressure fluctuation	76
7.1.3. Calibration	77
7.1.4. Noise analysis	79
7.2. Upgrading with the torsional pendulum	80
7.2.1. Idea of using a torsional pendulum	80
7.2.2. Advantages of an optomechanical torsional pendulum	80
7.2.3. Design sensitivity with the torsional pendulum	81
7.3. Towards experimental realization	83
7.3.1. Development of the torsional pendulum	83
7.4. Summary of this chapter	84
8. Conclusion	87
8.1. Summary	87
8.2. Future prospects	88
8.3. Conclusion	89
A. Classical feedback-control theory	91
A.1. Linear system	91
A.1.1. Definition	91
A.1.2. Transfer function	91
A.1.3. Block diagram	91
A.2. Feedback control	92
A.3. Measuring the open-loop transfer function	93

Glossary

Symbols

i	imaginary unit
π	pi: $\pi = 3.1415926535 \dots$
c	speed of light: $c = 299792458$ m/s
g	gravitational acceleration: $g = 9.80665$ m/s ²
h	Planck's constant: $h = 6.626070040(81) \times 10^{-34}$ J s
\hbar	Dirac's constant: $\hbar = h/2\pi = 1.054571800(13) \times 10^{-34}$ J s
k_B	Boltzmann constant: $k_B = 1.38064852(79) \times 10^{-23}$ J/K
f	Fourier frequency
ω	Fourier angular frequency
Ω	Sideband angular frequency
f_0	laser frequency
ω_0	laser angular frequency
λ	wavelength
P	laser power
f_m	mechanical resonant frequency
ω_m	mechanical angular resonant frequency
m	mass of an oscillator
Q	Q value
\mathcal{F}	fineness
κ	cavity decay rate
L	cavity length
T	temperature of thermal bath
S_x	displacement power spectral density
S_f	force power spectral density

Abbreviations

AOM	Acousto-Optical Modulator
BS	Beam Splitter

Contents

EOM	Electro Optical Modulator
FI	Faraday Isolator
FSR	Free Spectral Range
FWHM	Full Width at Half Maximum
HWP	Half Wave Plate
PBS	Polarizing Beam Splitter
PD	Photo Detector
PDH	Pound-Drever-Hall
PZT	Piezoelectric transducer
QPD	Quadrant Photo Detector
QWP	Quarter Wave Plate
RMS	Root Mean Square
SQL	Standard Quantum Limit
UGF	Unity Gain Frequency

1. Introduction

Quantum mechanics is an established theory in modern physics. Many phenomena that cannot be explained in the frame of classical mechanics are described explicitly in the quantum theory [1–4]. For some time after quantum mechanics was formulated, the microscopic world was the main playing field of quantum mechanics [5]. Even now, the boundary between the macroscopic world, where classical mechanics is dominant, and the microscopic world, where quantum mechanics is crucial, is a critical issue in physics.

It is not entirely clear what makes classical systems classical. Some classical theories were derived from quantum mechanics by the approximation at macroscopic systems with many assumptions [6]. However, in particular, how to incorporate gravitational effects into quantum mechanics has not yet been clarified. Theories including quantized gravity are exemplified by string theory [7–14] or loop quantum gravity [15–23]. However, these theories are not complete. It is unknown in string theory whether the extra dimensions can be chosen to satisfy the standard model, and loop quantum gravity has not yet been able to reproduce general relativity [24] in the classical limit. Apart from quantum gravity, there are proposed theories to explain decoherence in macroscopic systems to explain the absence of a macroscopic quantum phenomena, such as gravitational decoherence [25–27] or continuous spontaneous localization models [28, 29]. These proposed theories modify quantum mechanics by introducing a mechanism of spontaneous decoherence in macroscopic systems, so that macroscopic systems are projected to classical states. We note that although Bose-Einstein condensates [30] or superfluidity of liquid helium are a sort of macroscopic phenomena, massive objects, not many-body systems, are also essential to elucidate the unification of gravitational interaction or the modified quantum mechanics. Thus, in the dissertation, we will use the word *macroscopic* in the sense of mass scale.

These theoretical approaches to study macroscopic quantum mechanics leads to a demand for the realization of a macroscopic quantum system to test proposed theories. However, experimental observation of macroscopic quantum phenomena, such as implication of superposition state, have been limited up to nanogram scale. The situation has been changing. Recent progress in experimental techniques provides a suitable opportunity to realize a macroscopic quantum system. In particular, optomechanical systems have been increasingly attracting at-

1. Introduction

tention for precision measurements [31]. An optomechanical system is composed namely of mechanical oscillators and optical fields coupling to the oscillators. Radiation pressure of light acts for coupling an optical field to a mechanical oscillator. By utilizing the interference of optical fields, optomechanical systems measure the displacement of the oscillator precisely.

Among optomechanical systems, milligram scale optomechanical systems are suitable for macroscopic quantum experiments. The oscillator is more massive than the Planck mass for macroscopic quantum experiments, and the precision can be limited by quantum fluctuations to elucidate the nature of quantum mechanics. Methods to inspect the quantum nature of gravity with optomechanical systems are being actively discussed [32–37].

Macroscopic quantum systems are also important from the aspect of experimental applications. The best example is gravitational wave detectors. Gravitational waves are waves of warping spacetime predicted by Einstein [38, 39], and gravitational wave detectors measure the strain of them. While gravitational waves are unique signals that give us information about black holes [40–43], the equation of state of neutron stars, and the Big Bang [44], detecting gravitational waves is difficult because of their small amplitudes. Even relatively large gravitational waves that are emitted by coalescence of binary stars or explosions of supernova, the amplitude of the strain is about the order of 10^{-21} .

To detect such a weak gravitational wave, the modern and future gravitational wave detectors become huge experimental instruments [45, 46]. Nevertheless, their sensitivities are so precise that quantum effects have to be taken into account. In other words, the sensitivity will be limited by quantum noise in broadband frequencies. In particular, quantum radiation pressure noise, which is one of quantum noises, limits the sensitivity in the range between 10 Hz and 100 Hz, which is important band for gravitational waves from compact stars. Consequently, the gravitational wave detectors can be seen as a part of macroscopic quantum experiments. To enhance the future sensitivity, quantum noise must be reduced. Therefore, platforms of researching the characteristics of quantum noise in macroscopic optomechanical systems are desired.

These two motivations from macroscopic quantum experiments lead the active development of optomechanical systems, and pendulums are often used as the oscillators of milligram-scale, or more massive optomechanical systems. A pendulum is robust to the environmental vibration, and favorable for experiments of precise measurements. However, a suspended mirror in a linear cavity suffers from the instability due to the radiation pressure inside the cavity. This instability is called *Sidles-Sigg instability* [47]. In the dissertation, a stable configuration of a linear cavity that overcomes the Sidles-Sigg instability is presented and realized with a milligram-scale mirror. We report the evaluation of the stability of our optomechanical system, Furthermore, we demonstrate a quantum noise reduction technique as the proof of utility for

our setup. In addition, the practical feasibility of reaching quantum regime is discussed.

Outline of the dissertation

This dissertation is organized as follows. In Chapter 2, optomechanical systems are reviewed focusing on the sensitivity and the uses as precise sensors. The previous works are also reviewed, and the issues of them are pointed out. In Chapter 3, we pay attention to quantum noises in an optomechanical system. A method for the theoretical calculation of quantum noises are introduced. Chapter 4 shows our experimental setup. This chapter includes the concept and design of the linear cavity. Chapter 5 describes and discusses the stable configuration of a suspended linear cavity in detail. Chapter 6 shows the results of the experiment for demonstrating a quantum noise reduction technique. Chapter 7 discusses the current sensitivity of our optomechanical system and the possible upgrade for observing quantum radiation pressure fluctuation to reach quantum regime. Chapter 8 summarizes the results, future prospects, and concludes the dissertation. The conceptual diagram of the structure of the dissertation is shown in Fig. 1.1.

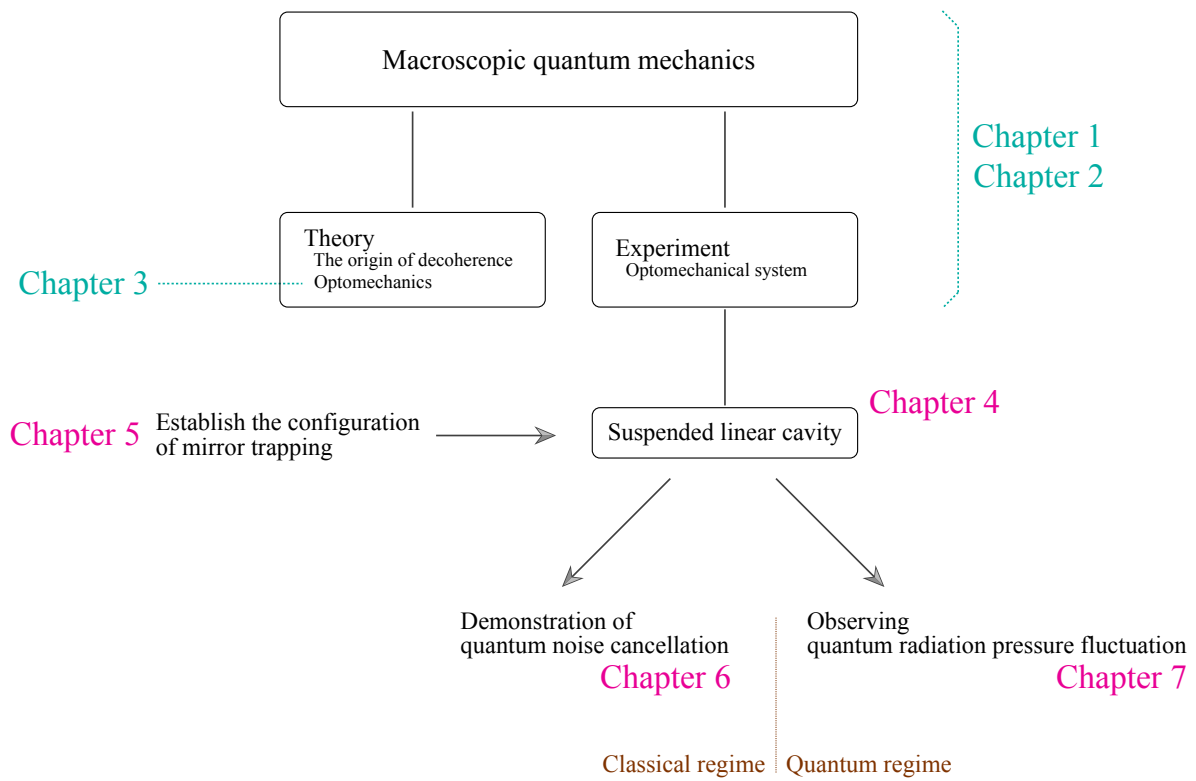


Figure 1.1.: Background and structure of the dissertation. The chapters written in green text compose the review part. The chapters written in magenta text are the main part representing the achievement of the dissertation.

2. Optomechanical system

2.1. Concepts

An optomechanical system consists of mechanical oscillators and optical fields. They are connected with the radiation pressure of the optical fields. The interaction via the radiation pressure is enhanced with optical cavities. For this reason, cavities are often used in optomechanical systems, and in particular, the study for such systems is called cavity optomechanics. The conceptual drawing of the model of an typical optical system is described in Fig. 2.1.

Optomechanical systems can be used for precise measurements. The displacement of the oscillator is read out by utilizing the interference of the optical field. Therefore, even if the mechanical oscillator is massive, its displacement is measured on a scale better than the wavelength. Since it is a favorable precise displacement/force sensor, optomechanical systems are utilized as, for example, gravitational wave detectors [48–50] and dark matter detection [51–56].

The characteristic of optomechanical systems is related to quantum experiments. Since the energy scale of the photon $\hbar\omega_0$ of a laser beam is much larger than the environmental energy scale of $k_B T$, the laser light propagates without decoherence. Therefore, the quantum nature of the mechanical oscillator can be efficiently extracted. In other words, the sensitivity of optomechanical systems has the potential to reach the quantum regime. To discuss the quantumness of

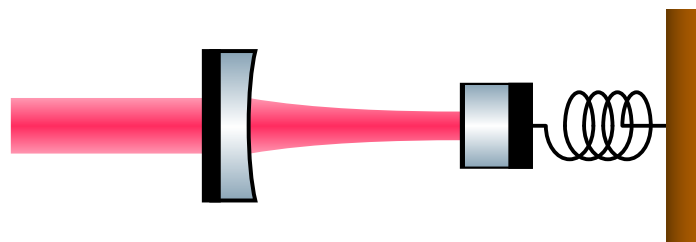


Figure 2.1.: Schematic drawing of an optomechanical system that consists of a linear cavity. The right mirror is the mechanical oscillator, which is in the harmonic potential. The laser beam enters from the left side. After interacting with the mechanical oscillator, the beam returns towards left side to be measured.

2. Optomechanical system

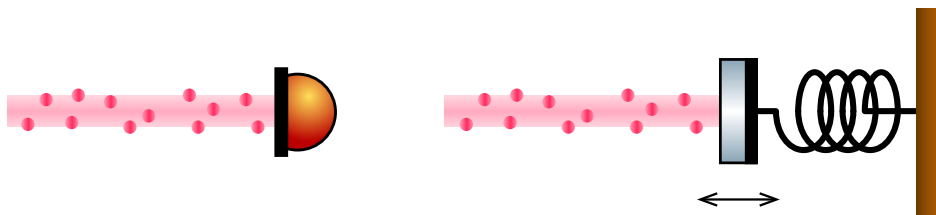


Figure 2.2.: Schematic picture of quantum noise. The quantum shot noise is a sensor noise due to the photon number fluctuation itself at the photo detector (left panel). The quantum radiation pressure noise is a force noise for the oscillator that the photon number fluctuation makes via optical radiation pressure (right panel).

an optomechanical system, let us introduce noise sources in optomechanical systems including quantum noise in the next section.

2.2. Noise sources

An optomechanical system measures the displacement of the mechanical oscillator. However, oscillators are subject to the undesirable forces as well as the external force that we try to measure. In addition, noises associated with the sensing is also indistinguishable from the displacement of the oscillator. In this section, let us view these noises one by one.

2.2.1. Quantum noise

Quantum fluctuations in the optical field and the oscillator of an optomechanical system introduce a principal noise into the system. Such noise is called quantum noise. There are two types of quantum noise: quantum shot noise and quantum radiation pressure noise. Quantum shot noise is a sensor noise that originates from the quantum fluctuation in the photon number of the laser beam. Quantum radiation pressure noise is a force noise that the photon number fluctuation produces via optical radiation pressure. The conceptual picture is shown in Fig. 2.2. The quantum radiation pressure is also called quantum radiation pressure fluctuation, or quantum back-action noise. The more detailed introduction and calculations of quantum noise are described in Chapter 3.

2.2.2. Thermal noise

Thermal noise is a class of noise sources that arise from the thermal motion of the oscillator or other environments. Typical thermal noises are those of the mirror substrate and coating and

those caused by the residual gas. The power spectral density of thermal noise $S_x(\omega)$ is obtained by the fluctuation-dissipation theorem as

$$S_x(\omega) = -\frac{4k_B T}{\omega} \text{Im}[H(\omega)]. \quad (2.1)$$

where k_B is the Boltzmann constant, T is the temperature of the thermal bath coupling to the system, ω is the angular frequency of the motion, and H is the transfer function from the force to the displacement x of the oscillator. For example, the transfer function of a simple pendulum is described by

$$H(\omega) = \frac{1}{m [\omega_0^2(1 + i\phi(\omega)) - \omega^2]}, \quad (2.2)$$

where ω_0 is the resonant angular frequency, and $\phi(\omega)$ is the loss angle. Loss angle is a parameter to characterize the energy dissipation of the system. Equation (2.1) leads to the noise spectrum,

$$S_x(\omega) = \frac{4k_B T}{m\omega} \frac{\omega_0^2 \phi(\omega)}{(\omega^2 - \omega_0^2)^2 + \omega_0^4 \phi^2(\omega)}. \quad (2.3)$$

There are two dissipation models; one is called viscous-damping model, and the other is called structure-damping model. The viscous-damping model is a model where the oscillation energy is decayed with a force in proportion to its velocity. In the structure-damping model, the internal structure cause the energy loss. The loss angles and decay rates in Fourier space are expressed in each model as follows:

$$\text{viscous-damping model : } \phi(\omega) = \frac{\omega}{Q\omega_0}, \quad \gamma = \frac{\omega_0}{Q}, \quad (2.4)$$

$$\text{structure-damping model : } \phi = \frac{1}{Q}, \quad \gamma(\omega) = \frac{\omega_0^2}{Q\omega}. \quad (2.5)$$

Let us consider examples in the following part of this section.

Suspension thermal noise

When we use a pendulum for the oscillator, the pendulum mode has its thermal noise. This suspension thermal noise is a structure thermal noise of a pendulum. According to Eq. (2.3), the noise spectrum S_{sus} is expressed as

$$S_x^{\text{sus}}(\omega) = \frac{4k_B T_{\text{th}} \omega_{\text{pend}}^2 \phi_{\text{pend}}}{m\omega^5}, \quad (2.6)$$

where ω_{pend} is the resonant angular frequency and ϕ_{pend} is the loss angle of the pendulum, and we assume that the frequency band of interest is much higher than the resonant frequency.

2. Optomechanical system

Mirror substrate/coating thermal noise

To calculate the mirror substrate/coating thermal noise, it is convenient to introduce the Levin's reciprocal approach [57], instead of Eq. (2.1). With this approach, the power spectral density is described by the following form:

$$S_x(\omega) = -\frac{8k_B}{\omega^2} \sum_i \frac{T_i W_{\text{diss},i}}{F_0^2}, \quad (2.7)$$

where F_0 is the amplitude of an imaginary sinusoidal test force whose distribution is identical to that of the laser beam intensity. T_i is the temperature of each thermal bath, and $W_{\text{diss},i}$ is the energy loss per unit time to the corresponding thermal bath while the imaginary force is applied. By using Levin's approach, the thermal noise of the mirror substrate/coating, S_x^{sub} , S_x^{coat} , are obtained as [58, 59]

$$S_x^{\text{sub}}(\omega) = \frac{4k_B T}{\omega} \frac{\phi_s}{\sqrt{\pi} w_0} \frac{(1 - \nu_s^2)}{Y_s}, \quad (2.8)$$

$$S_x^{\text{coat}}(\omega) = \frac{4k_B T}{\omega} \frac{d_c \phi_c}{\pi w_0^2} \frac{Y_c^2 (1 + \nu_s)^2 (1 - 2\nu_s)^2 + Y_s^2 (1 + \nu_c)^2 (1 - 2\nu_c)}{Y_s^2 Y_c (1 - \nu_c)^2}, \quad (2.9)$$

where ϕ is the loss angle of the mirror substrate, w_0 is the beam radius on the mirror, ν is the Poisson ratio, Y is the Young modulus, and d_c is the coating thickness. The subscription s indicates the mirror substrate, while c indicates the mirror coating.

Residual gas noise

When an oscillator is in a less than perfect vacuum, the residual gas becomes a resistive force proportional to the velocity of the oscillator. Therefore, the residual gas noise is modeled by the viscous-damping model. It is known that the Q value of the residual gas is described by [60]

$$Q = \frac{C m \omega_0}{SP} \sqrt{\frac{k_B T}{m_{\text{mol}}}}, \quad (2.10)$$

where S is the area of the surface, P is the pressure of the gas, m_{mol} is the molecular mass of the gas, and C is the factor depending on the shape of the oscillator, which is nearly unity for cylinder-shaped mirrors.

2.2.3. Other noises

Laser frequency noise

Since the optomechanical system utilize the interferometry to measure the phase of the light to sense the displacement of the oscillator, laser frequency fluctuation is a noise source indis-

tinguishable from the oscillator's displacement. For the laser angular frequency ω_0 , the phase rotation ϕ through a distance of L variate as

$$2d\phi = \frac{2L\omega_0}{c} \left(\frac{dL}{L} + \frac{d\omega_0}{\omega_0} \right). \quad (2.11)$$

Therefore, the displacement spectrum of the laser frequency noise S_x^{freq} is expressed by

$$\sqrt{S_x^{\text{freq}}(f)} = L \frac{\sqrt{S_f^{\text{freq}}(f)}}{f_0}, \quad (2.12)$$

where $S_f^{\text{freq}}(f)$ is the power spectral density of the laser frequency fluctuation, and f_0 is the laser frequency.

Seismic noise

The ground on the Earth continuously vibrate, and the oscillator's seismic motion introduce a displacement noise that is called seismic noise. The typical spectrum of the seismic motion is

$$\sqrt{S_{\text{seis}}(f)} \sim \begin{cases} 10^{-5} \text{ m}/\sqrt{\text{Hz}} & (f < 0.1 \text{ Hz}) \\ 10^{-7} \times \left(\frac{1 \text{ Hz}}{f}\right)^2 \text{ m}/\sqrt{\text{Hz}} & (f > 0.1 \text{ Hz}) \end{cases}. \quad (2.13)$$

To reduce the seismic noise, a vibration isolation system for the oscillator is necessary. For example, a multiple suspension system (n -stage pendulum) can suppress the seismic noise by the factor of f^{-2n} above the resonant frequencies.

2.3. Uses for macroscopic quantum experiments

Optomechanical systems are suitable for macroscopic quantum experiments. By utilizing the interference, optomechanical systems can sense the oscillator's displacement on a scale better than the wavelength of the optical field even if the oscillator is massive. The joint characteristics lead to the quantumness and macroscopicity of the system simultaneously. In this section, let us see some examples for uses of optomechanical systems for macroscopic quantum experiments. The examples indicate the supremacy of milligram-scale optomechanical systems for their purpose. They cannot be conducted with large scale systems, such as gravitational wave detectors, due to the lack of flexibility. On the other hand, the small scale below the Planck mass is not enough heavy to observe gravitational effects or mass dependency in the modified quantum theories.

2. Optomechanical system

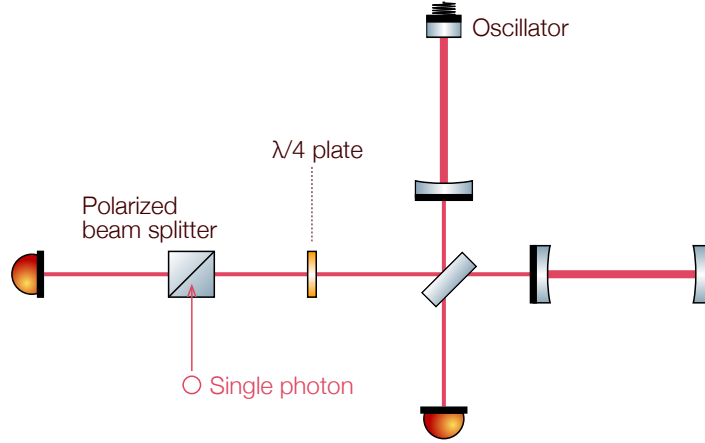


Figure 2.3.: Proposed experiment to measure the decoherence time of a superposition state of a massive object by *Marshall et al.* [61].

2.3.1. Testing macroscopic quantum mechanics

Quantum mechanics is an established theory in modern physics. Many microscopic phenomena are explained precisely according to quantum mechanics. However, although quantum mechanics itself does not limit the scope by a mass scale, no quantum phenomenon indicating the superposition state of a massive object has been observed. It is an open question whether quantum mechanics holds valid along all the mass scale, or quantum mechanics breaks at some mass scale and needs to be modified. Therefore, experimental tests are desired by realizing macroscopic quantum systems.

Let us introduce proposed optomechanical experiments of a superposition state with a massive object. After developing macroscopic quantum optomechanical systems, the following experiments will come true and will be able to test macroscopic quantum mechanics.

Marshall et al. [61] proposed an experiment to measure the decoherence time of the superposition state of the massive mirror in an optomechanical system. The optomechanical system is a Michelson interferometer, whose arms have linear cavities, as described in Fig. 2.3. The target mirror that will be observed in a superposition state is placed at the end of a linear cavity. The other end mirror is fixed. By injecting a single photon, the state would be

$$|\psi(0)\rangle = \frac{|0\rangle_A |1\rangle_B + |1\rangle_A |0\rangle_B}{\sqrt{2}}, \quad (2.14)$$

where the subscriptions A , B refer to each system of the arms. The state describes the superposition of a state where the photon exists in the arm A and a state where the photon exists in the arm B .

If the target mirror is cooled down to its ground state $|0\rangle_m$, the state will evolve with time t

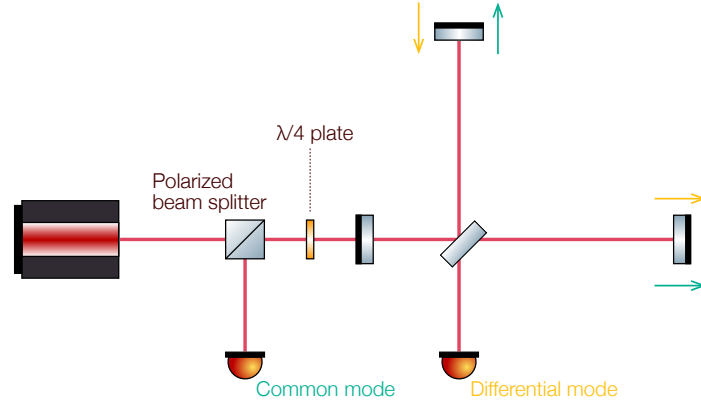


Figure 2.4.: Proposed experiment to realize a superposition state with massive mirrors by Müller-Ebhardt *et al.* [62].

as

$$|\psi(t)\rangle = \frac{1}{\sqrt{2}} \left[|0\rangle_A |1\rangle_B |0\rangle_m + e^{i\zeta^2(\omega_m t - \sin \omega_m t)} |1\rangle_A |0\rangle_B \left| \zeta \left(1 - e^{-i\omega_m t} \right) \right\rangle_m \right], \quad (2.15)$$

where we define $\zeta = (\omega_0/L\omega_m) \sqrt{(\hbar/2m\omega_m)}$, and ω_m is the angular resonant frequency of the target mirror, m is the mass of the mirror, L is the cavity length, and ω_0 is the angular frequency of the single photon. The decoherence time is measured by the visibility of the interferometer. While the entangled state holds, the visibility should oscillate with the mirror oscillation. After the decoherence, the visibility will keep zero.

Müller-Ebhardt *et al.* [62] proposed an experiment to realize the entangled state with massive mirrors. The proposed configuration, based on that of gravitational wave detectors, is shown in Fig. 2.4. When the sensitivity of the interferometer reach the standard quantum limit, the common mode and the differential mode of the interferometer will be entangled. The displacements of the common and differential modes are measured by photo detectors placed at the each port, respectively. The entanglement can be evaluated by the logarithmic negativity of the system. An finite logarithmic negativity implies the existence of the entangled state between the massive end mirrors.

2.3.2. Platform for demonstrating advanced technologies in gravitational wave detectors

Gravitational wave detectors are one of the representative optomechanical systems. The sensitivity of the gravitational wave detectors are, and will be limited by quantum noises. Quantum noises are fundamental noises and can not be reduced by classical manipulation. Although

2. Optomechanical system

several advanced techniques to reduce quantum noises were proposed, a number of techniques are waiting their experimental demonstrations.

Table-top scale experimental platform to demonstrate advanced techniques are crucial in the gravitational wave detectors. The modern gravitational wave detectors are typically huge experimental apparatus; they consists of kilo-meter scale interferometers. It takes much efforts to incorporate and install new technologies into them. Thus, it is consequential to assure the validity of the techniques before the actual installation.

Let us give an example of advanced technologies of quantum noise reduction. Typical gravitational wave detectors are based on a Michelson interferometer. To enhance its sensitivity, a mirror that is called signal recycling mirror is installed at the output port of the Michelson interferometer. The signal recycling mirror composes a cavity to enhance gravitational wave signals. This cavity is called signal recycling cavity. In conventional configurations, the phase delay can be ignored between the signal recycling mirror and the beam splitter in the Michelson interferometer. However, recently, it was proposed that the quantum noise could be reduced by using a long recycling cavity by considering the effect of the phase delay. Although the technique has not yet been validated experimentally, there is a proposals to incorporate the effect into the proposed future gravitational wave detector [63]. Therefore, the experimental demonstration with a table-top scale system is desired.

2.4. Previous works

We have seen the uses of optomechanical systems for macroscopic quantum experiments. In this section, we will review previous works that experimented with optomechanical systems that were aimed to be conducted in the quantum regime.

2.4.1. Observation of quantum radiation pressure fluctuation

One criteria of quantum regime for optomechanical systems are observing quantum radiation pressure fluctuation. Quantum shot noise is observed even in the absence of optomechanical interactions, and have been already observed or reduced with squeezed light at various mass scales [64–66]. However, dominance of quantum radiation pressure fluctuation was realized only below the nanogram scale.

In 2013, *Purdy et al.* reported observation of quantum radiation pressure fluctuation with 7 ng membrane. In 2018, *Cripe et al.* observed quantum radiation pressure fluctuation with a 50 ng cantilever. This was the most macroscopic system that succeeded in the direct observation. The line width of the observation was 500 kHz and the mechanical resonant frequency

was 876 Hz. The resonant frequency increased to 10 kHz with an optical spring effect. The observation is realized in broadband frequencies, though it is at the mechanical resonant region.

In 2020, the gravitational wave detectors, Advanced LIGO and Advanced Virgo also reported the effect of quantum radiation pressure fluctuation [67, 68]. Although quantum radiation pressure noise is not dominant, they observed the increases in noise spectra due to quantum radiation pressure noise. For quantum macroscopic experiments, direct observation of quantum radiation pressure fluctuation is necessary, and this has been achieved in experiments below the nanogram scale. It is expected to expand the mass range where direct observation of quantum radiation pressure fluctuation is possible. In particular, the milligram scale is a key scale because it is inferred that the displacement induced by the gravitational coupling can be sensed in milligram scale optomechanical systems with realistic parameters [69]. In other words, the milligram scale is the unique scale that has the potential to simultaneously observe quantumness and gravitational effects; this feature is essential for fundamental physics as we have seen in the Chapter 1.

2.4.2. Impediments to improvement of the sensitivity at milligram scale

Let us review macroscopic optomechanical systems over microgram scale. The direct observation of quantum radiation pressure fluctuation has not yet been accomplished in this mass range. However, several groups are actively working towards this goal.

Suspended pendulum

Suspended pendulums are often adopted as mechanical oscillators in optomechanical systems over microgram scale [67, 69–77], while membranes and cantilevers are widely used in many experiments of smaller mass scales [78–80]. An advantage to use suspended pendulums is a feature that they can be well isolated from the environment. In other words, pendulums are resistant to seismic noise and thermal noise. In addition, pendulums have a broad free-mass region over the resonant frequency. For this reason, in general, pendulums have a wide sensitive frequency range.

Sidles-Sigg instability

However, the issue of suspended pendulums as mechanical oscillators is their instability in the rotational degree of freedom. The yaw rotational motion of suspended mirrors changes the beam spot position of the laser inside a cavity. Due to the change in the position of the beam spot, the radiation pressure in the cavity can behave as an anti-restoring torque and destabilize

2. Optomechanical system

the cavity. In particular, either of two degrees of freedom in a rotational direction is unstable, and it is so called Sidles-Sigg instability [47].

In the case that the mechanical restoring torque is dominant in the rotational degree of freedom, Sidles-Sigg instability does not matter because the radiation pressure torque would be too weak to make a pendulum unstable. Thus, several experiments used multiple wires to suspend a mirror to stiffen the pendulum in the rotational degree of freedom [75, 76, 81]. However, increase of wires induces a stronger coupling to a thermal bath. As the result, the thermal noise due to the suspension can get larger. In addition, suspension with multiple wires is technically difficult to suspend a pendulum symmetrically. For example, *Neben et al.* [76] built a linear cavity with 1 g suspended mirror to observe quantum radiation pressure fluctuation. The mirror is suspended with two fibers to overcome Sidles-Sigg instability. However, the thermal noise at the bonding of the fiber covered quantum radiation pressure fluctuation.

Another way to deal with Sidles-Sigg instability is introducing feedback control in the rotational motion [82, 83]. If an oscillator has actuators applying torque on it, the unstable rotational motion can be suppressed by a feedback control. However, milligram or gram scale oscillators are often too small to attach actuators to [74]. In such cases, more complicated feedback systems were required to actuate a tiny oscillator remotely [84, 85].

As a different approach, some experiments used triangular cavities to avoid Sidles-Sigg instability [71–73]. When the number of mirrors consisting in the cavity is odd, the radiation pressure behaves as a positive restoring torque, as shown in Fig. 2.5. Thus, the Sidles-Sigg instability does not exist. However, additional mirrors are noise sources. Actually, *Komori* [73, 86] reported that the sensitivity of their system with triangular cavities was limited by thermal noises of the additional mirror in the broad region of several hundred Hz. For the best sensitivity, a cavity with only two mirrors—a linear cavity—is favorable. Therefore, a stable configuration of linear cavities is desired. In other words, more sensitive milligram-scale optomechanical systems can be realized by designing a stable trapping of a linear cavity mirror.

2.5. Summary of this chapter

Optomechanical systems are suitable for precise measurements. In particular, it is expected that milligram-scale optomechanical systems can be used for macroscopic quantum experiments. Up to the nanogram scale, there are experiments that realized a quantum optomechanical system. However, over the microgram scale, the instability due to the radiation pressure inside a linear cavity impeded observation of quantum radiation pressure fluctuation.

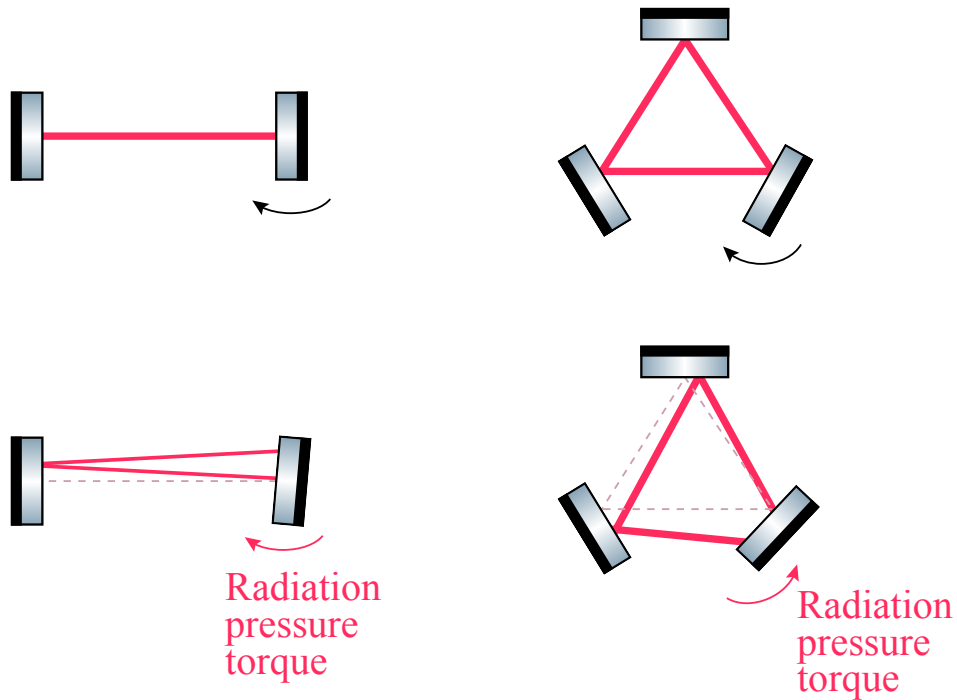


Figure 2.5.: Triangular cavity to avoid Sidles-Sigg instability. In the case of a linear cavity, tilt of a flat cavity mirror causes changes in the cavity axis. As the result, the tilting mirror is subject to radiation pressure torque in the same direction as the tilt direction. Thus, the tilt becomes larger, and the system is unstable. On the other hand, in a triangular cavity, the tilting angle is flipped by additional mirror. The resulting radiation pressure torque acts as a positive restoring torque. Therefore, the system is stabilized with the radiation pressure.

3. Quantum noise in optomechanical systems

In this chapter, we review the basic concepts of quantum noise in optomechanical systems. In addition, the mathematical description and calculations of them are introduced.

3.1. Conceptual overview of quantum noise

There are two types of quantum noise: quantum shot noise and quantum radiation pressure noise. This section provides an overview of them one by one.

3.1.1. Quantum shot noise

According to quantum electrodynamics, the photon number of an optical field is an observable, and photon number can have the quantum fluctuation. Shot noise originates from the uncertainty of the photon counting due to the quantum fluctuation on the photon number. In case that an optical field is in a coherent state, the outcome of the measurement on the photon number follows the Poisson distribution. That is, the probability of finding n photons is

$$P_n = \frac{\langle n \rangle^n}{n!} e^{-\langle n \rangle}, \quad (3.1)$$

where $\langle n \rangle$ is the expected value of the photon number. This is the Poisson distribution with variance $\langle n \rangle$. The Poissonity implies that the shot noise has a flat spectrum.

3.1.2. Quantum radiation pressure noise

Let us consider a harmonic oscillator that couples to an optical field. The oscillator is subjected to radiation pressure from the optical field. The radiation pressure F_{rad} is given by

$$F_{\text{rad}} = \frac{2P}{c}, \quad (3.2)$$

3. Quantum noise in optomechanical systems

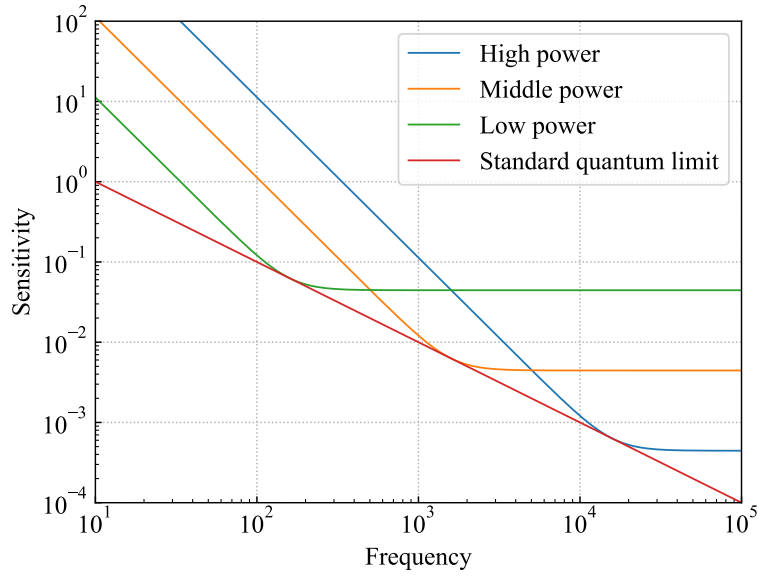


Figure 3.1.: Standard quantum limit with quantum shot noise and quantum radiation pressure noise. The sensitivity is limited by the SQL even when the laser power is changed.

where P is the power of the optical field. Therefore, when P fluctuates as quantum shot noise, the radiation pressure also fluctuates. This force noise is called quantum radiation pressure noise.

3.1.3. Standard Quantum Limit

Before moving onto the detailed calculation of quantum noise, we introduce a concept called standard quantum limit (SQL). The standard quantum limit is a fundamental limit of the sensitivity for optomechanical systems. It is defined as the sum of quantum shot noise and quantum radiation pressure noise.

The signal to noise ratio of quantum shot noise is in proportion to $1/\sqrt{P}$ since it follows a Poisson distribution. On the other hand, the signal to noise ratio of quantum radiation pressure noise is proportional to \sqrt{P} . Therefore, there is a lower bound on the sum of quantum shot noise and quantum radiation pressure noise independently to the laser power. This lower bound is the standard quantum limit. The plot for the standard quantum limit is shown in Fig. 3.1.

3.2. Quantized electromagnetic fields

In optomechanical systems, optical fields are coupled to mechanical oscillators. To describe optomechanical systems, firstly we review the mathematical description of quantized electromagnetic fields.

3.2.1. Quantization of electromagnetic fields

The Maxwell's equations in vacuum are:

$$\nabla \cdot \mathbf{E}(\mathbf{r}, t) = 0, \quad (3.3)$$

$$\nabla \cdot \mathbf{B}(\mathbf{r}, t) = 0, \quad (3.4)$$

$$\nabla \times \mathbf{E}(\mathbf{r}, t) = -\frac{\partial \mathbf{B}}{\partial t}, \quad (3.5)$$

$$\nabla \times \mathbf{B}(\mathbf{r}, t) = \frac{1}{c^2} \frac{\partial \mathbf{E}}{\partial t}, \quad (3.6)$$

where $\mathbf{E}(\mathbf{r}, t)$ is the electric field and $\mathbf{B}(\mathbf{r}, t)$ is the magnetic field (magnetic flux density). The electric and magnetic fields can be also represented using the scalar potential $\phi(\mathbf{r}, t)$ and the vector potential $\mathbf{A}(\mathbf{r}, t)$ as

$$\mathbf{E}(\mathbf{r}, t) = -\frac{\partial \mathbf{A}}{\partial t} - \nabla \phi, \quad (3.7)$$

$$\mathbf{B}(\mathbf{r}, t) = \nabla \times \mathbf{A}. \quad (3.8)$$

When we use the Coulomb gauge, $\nabla \cdot \mathbf{A} = 0$, the vector potential follows the wave equation as

$$\left(\nabla^2 - \frac{1}{c^2} \frac{\partial^2}{\partial t^2} \right) \mathbf{A}(\mathbf{r}, t) = 0. \quad (3.9)$$

The solutions imply the existence of electromagnetic waves. The wave vector \mathbf{k} of the solution is orthogonal to its vector potential $\mathbf{A}(\mathbf{k})$, and we define the unit vectors in the directions of polarizations, $\mathbf{e}_\mu(\mathbf{k})$ ($\mu = 1, 2$), so that they are orthogonal to the unit vector $\hat{\mathbf{k}}$ of the propagating direction as $\hat{\mathbf{k}} = \mathbf{e}_1(\mathbf{k}) \times \mathbf{e}_2(\mathbf{k})$. Then, the vector potential is written with the angular frequency of the electromagnetic wave as

$$\mathbf{A}(\mathbf{r}, t) = \sum_{\mu, \mathbf{k}} \left(A_{\mathbf{k}}^\mu e^{-i(\omega_{\mathbf{k}} t - \mathbf{k} \cdot \mathbf{r})} + \left(A_{\mathbf{k}}^\mu \right)^* e^{i(\omega_{\mathbf{k}} t - \mathbf{k} \cdot \mathbf{r})} \right) \mathbf{e}_\mu(\mathbf{k}). \quad (3.10)$$

3. Quantum noise in optomechanical systems

Therefore, the electric field is described with $\omega_{\mathbf{k}}$ by

$$\mathbf{E}(\mathbf{r}, t) = \sum_{\mu, \mathbf{k}} i\omega_{\mathbf{k}} \left(A_{\mathbf{k}}^{\mu} e^{-i(\omega_{\mathbf{k}} t - \mathbf{k} \cdot \mathbf{r})} - \left(A_{\mathbf{k}}^{\mu} \right)^* e^{i(\omega_{\mathbf{k}} t - \mathbf{k} \cdot \mathbf{r})} \right) \mathbf{e}_{\mu}(\mathbf{k}), \quad (3.11)$$

while the magnetic field is

$$\mathbf{B}(\mathbf{r}, t) = \sum_{\mu, \mathbf{k}} ik \left(A_{\mathbf{k}}^{\mu} e^{-i(\omega_{\mathbf{k}} t - \mathbf{k} \cdot \mathbf{r})} - \left(A_{\mathbf{k}}^{\mu} \right)^* e^{i(\omega_{\mathbf{k}} t - \mathbf{k} \cdot \mathbf{r})} \right) \hat{\mathbf{k}} \times \mathbf{e}_{\mu}(\mathbf{k}). \quad (3.12)$$

Note that $k = |\mathbf{k}|$. Let us calculate the energy of the electromagnetic wave in a cube of the volume V and the side length l . The integrations of

$$\int \mathbf{E}^2 d\mathbf{r} = V \sum_{\mu, \nu, \mathbf{k}} \left[-\omega_{\mathbf{k}} \omega_{-\mathbf{k}} \left(A_{\mathbf{k}}^{\mu} A_{-\mathbf{k}}^{\nu} e^{-i(\omega_{\mathbf{k}} + \omega_{-\mathbf{k}})t} + \left(A_{\mathbf{k}}^{\mu} \right)^* \left(A_{-\mathbf{k}}^{\nu} \right)^* e^{i(\omega_{\mathbf{k}} + \omega_{-\mathbf{k}})t} \right) \mathbf{e}_{\mu}(\mathbf{k}) \cdot \mathbf{e}_{\nu}(-\mathbf{k}) \right. \\ \left. + 2\omega_{\mathbf{k}}^2 \left(A_{\mathbf{k}}^{\mu} \right)^* A_{\mathbf{k}}^{\mu} \right] \quad (3.13)$$

and

$$\int \mathbf{B}^2 d\mathbf{r} = V \sum_{\mu, \nu, \mathbf{k}} k^2 \left[\left(A_{\mathbf{k}}^{\mu} A_{-\mathbf{k}}^{\nu} e^{-i(\omega_{\mathbf{k}} + \omega_{-\mathbf{k}})t} + \left(A_{\mathbf{k}}^{\mu} \right)^* \left(A_{-\mathbf{k}}^{\nu} \right)^* e^{i(\omega_{\mathbf{k}} + \omega_{-\mathbf{k}})t} \right) \mathbf{e}_{\mu}(\mathbf{k}) \cdot \mathbf{e}_{\nu}(-\mathbf{k}) \right. \\ \left. + 2 \left(A_{\mathbf{k}}^{\mu} \right)^* A_{\mathbf{k}}^{\mu} \right] \quad (3.14)$$

indicate the energy H is

$$H = \int \left(\frac{1}{2} \varepsilon_0 \mathbf{E}^2 + \frac{1}{2\mu_0} \mathbf{B}^2 \right) = \sum_{\mu, \mathbf{k}} 2\varepsilon_0 \omega(\mathbf{k})^2 V \left(A_{\mathbf{k}}^{\mu} \right)^* A_{\mathbf{k}}^{\mu}. \quad (3.15)$$

To derive the above expression, we should use the dispersion relation $\omega(\mathbf{k}) = ck$. By defining the generalized coordinate $Q_{\mathbf{k}}^{\mu}$ and the generalized momentum $P_{\mathbf{k}}^{\mu}$ as

$$Q_{\mathbf{k}}^{\mu} = 2\sqrt{\varepsilon_0 V} \operatorname{Re} \left(A_{\mathbf{k}}^{\mu} \right), \quad (3.16)$$

$$P_{\mathbf{k}}^{\mu} = 2\omega_{\mathbf{k}} \sqrt{\varepsilon_0 V} \operatorname{Im} \left(A_{\mathbf{k}}^{\mu} \right), \quad (3.17)$$

the energy is rewritten by

$$H = \frac{1}{2} \sum_{\mu, \mathbf{k}} \left[\left(P_{\mathbf{k}}^{\mu} \right)^2 + \omega_{\mathbf{k}}^2 \left(Q_{\mathbf{k}}^{\mu} \right)^2 \right], \quad (3.18)$$

which is identical to the hamiltonian of a harmonic oscillator. Thereby, let us impose the following commutation relation:

$$[\hat{Q}_k^\mu, \hat{P}_{k'}^\nu] = i\hbar\delta_{\mathbf{k},\mathbf{k}'}\delta_{\mu\nu} \quad (3.19)$$

to describe the quantized hamiltonian of the electromagnetic field as

$$\hat{H} = \frac{1}{2} \sum_{\mu,\mathbf{k}} \left[\left(\hat{P}_k^\mu \right)^2 + \omega_k^2 \left(\hat{Q}_k^\mu \right)^2 \right]. \quad (3.20)$$

As we often do with harmonic oscillators, we define the annihilation operator by

$$\hat{a}_k^\mu = \sqrt{\frac{\omega_k}{2\hbar}} \hat{Q}_k^\mu + i \frac{1}{\sqrt{2\hbar\omega_k}} \hat{P}_k^\mu. \quad (3.21)$$

Since the vector potential operator is written by

$$\hat{A}_k^\mu = \sqrt{\frac{\hbar}{2\epsilon_0\omega_k V}} \hat{a}_k^\mu, \quad (3.22)$$

the expressions of the quantized electric field and magnetic field are

$$\hat{\mathbf{E}}(\mathbf{r}, t) = \sum_{\mu,\mathbf{k}} i \sqrt{\frac{\hbar\omega_k}{2\epsilon_0 V}} \left(\hat{a}_k^\mu e^{-i(\omega_k t - \mathbf{k}\cdot\mathbf{r})} - \left(\hat{a}_k^\mu \right)^\dagger e^{i(\omega_k t - \mathbf{k}\cdot\mathbf{r})} \right) \mathbf{e}_\mu(\mathbf{k}), \quad (3.23)$$

$$\hat{\mathbf{B}}(\mathbf{r}, t) = \sum_{\mu,\mathbf{k}} i \sqrt{\frac{\mu_0\hbar\omega_k}{2V}} \left(\hat{a}_k^\mu e^{-i(\omega_k t - \mathbf{k}\cdot\mathbf{r})} - \left(\hat{a}_k^\mu \right)^\dagger e^{i(\omega_k t - \mathbf{k}\cdot\mathbf{r})} \right) \hat{\mathbf{k}} \times \mathbf{e}_\mu(\mathbf{k}). \quad (3.24)$$

The commutation relations between the creation operator $(\hat{a}_k^\mu)^\dagger$ and the annihilation operator \hat{a}_k^μ are

$$\left[\hat{a}_k^\mu, (\hat{a}_{k'}^\nu)^\dagger \right] = \delta_{\mathbf{k}\mathbf{k}'}\delta_{\mu\nu}, \quad (3.25)$$

while the commutation relations of the other combinations are zero.

3.2.2. Two photon formalism

In the previous section, we discuss the canonical quantization of the electromagnetic field. In the case that we focus on the optomechanical systems, it is often useful to adopt two photon formalism [87–89]. In this section, we review the two photon formalism; two photon formalism is derived by transformation of the annihilation operator.

Firstly, let us consider an electromagnetic wave propagating in the direction of z axis in free space. To deal with free space propagating as $l \rightarrow \infty$, the summation is replaced by

3. Quantum noise in optomechanical systems

the integration over the continuous values of the frequency as $\sum_k \rightarrow 1/(2\pi c/l) \int d\omega$. The Eq. (3.23) is simplified as

$$\hat{E}(t) = \int_0^\infty \sqrt{\frac{\hbar\omega}{4\pi\epsilon_0 c \mathcal{A}}} \left(\hat{a}_\omega e^{-i\omega t} + \hat{a}_\omega^\dagger e^{i\omega t} \right) d\omega, \quad (3.26)$$

where \mathcal{A} is the effective cross section area of the propagating beam, and the annihilation operator corresponding to the angular frequency ω is defined by $\hat{a}_\omega = i\sqrt{2\pi c/l} \hat{a}_k \exp(i\omega z/c)$. Correspondingly, the commutation relation for the continuous case is

$$[\hat{a}_\omega, \hat{a}_{\omega'}^\dagger] = 2\pi\delta(\omega - \omega'), \quad (3.27)$$

and the commutation relations of the other combinations are zero.

Considering an optomechanical system, when an external force of angular frequency Ω is applied to the oscillator, sideband lights of angular frequency $\omega_0 + \Omega$ and $\omega_0 - \Omega$ generate around the carrier light angular frequency ω_0 . Thus, the quantum noise that contribute to limit the sensitivity is at the sideband frequencies. Therefore, it is convenient to use the creation and annihilation operators at the sideband frequencies. In the case of $\Omega \ll \omega_0$, and the quantized electric field is rewritten by

$$\hat{E}(t) = \sqrt{\frac{\hbar\omega_0}{4\pi\epsilon_0 c \mathcal{A}}} \int_0^\infty \left[e^{-i\omega_0 t} \left(\hat{a}_+ e^{-i\Omega t} + \hat{a}_- e^{i\Omega t} \right) + e^{i\omega_0 t} \left(\hat{a}_+^\dagger e^{i\Omega t} + \hat{a}_-^\dagger e^{-i\Omega t} \right) \right] d\Omega, \quad (3.28)$$

where the $\hat{a}_+ = \hat{a}_{\omega_0+\Omega}$ is the annihilation operator of the upper sideband and $\hat{a}_- = \hat{a}_{\omega_0-\Omega}$ is the annihilation operator of the lower sideband. The commutation relations are calculated as

$$[\hat{a}_+, \hat{a}_+^\dagger] = 2\pi\delta(\Omega - \Omega'), \quad [\hat{a}_-, \hat{a}_-^\dagger] = 2\pi\delta(\Omega - \Omega'). \quad (3.29)$$

The commutation relations of the other combinations are zero.

The quantized electric field can be decomposed into the quadratures as

$$\hat{E}(t) = \sqrt{\frac{4\pi\hbar\omega_0}{\epsilon_0 c \mathcal{A}}} [\hat{a}_1(t) \cos(\omega_0 t) + \hat{a}_2(t) \sin(\omega_0 t)]. \quad (3.30)$$

Therefore, the quantized amplitude quadrature \hat{a}_1 and the quantized phase quadrature \hat{a}_2 are described by

$$\hat{a}_1(\Omega) = \frac{\hat{a}_+ + \hat{a}_-^\dagger}{\sqrt{2}}, \quad (3.31)$$

$$\hat{a}_2(\Omega) = \frac{\hat{a}_+ - \hat{a}_-^\dagger}{\sqrt{2}i}, \quad (3.32)$$

where

$$\hat{a}_j(t) = \int_0^\infty \left(\hat{a}_j(\Omega) e^{-i\Omega t} + \hat{a}_j(\Omega)^\dagger e^{i\Omega t} \right) \frac{d\Omega}{2\pi} \quad (j = 1, 2). \quad (3.33)$$

These are the Fourier transformations of the quadratures since $\hat{a}_j(-\Omega) = \hat{a}_j^\dagger(\Omega)$. The commutation relations are

$$\left[\hat{a}_1(\Omega), \hat{a}_2^\dagger(\Omega') \right] = - \left[\hat{a}_2(\Omega), \hat{a}_1^\dagger(\Omega') \right] = i2\pi\delta(\Omega - \Omega'), \quad (3.34)$$

while the commutation relations of the other combinations are zero.

3.2.3. Quantum states of the optical field

So far, we have seen the expressions of the electric field operators. To calculate the expectation values and fluctuations of the electric field, it is necessary to specify not only the operators, but also the quantum states. In this section, we will see two characteristic states: *vacuum state* and *coherent state*. These two states is the typical quantum states for optical systems with laser beams.

Vacuum state

The vacuum state $|0\rangle$ is defined as the state without any excitation at every frequency; $\hat{a}_\omega |0\rangle = 0$.

Let us consider the power spectral density of the signal to noise ratio of the external force signal and quantum noise for the vacuum state. For the pair of operators \hat{O}_1 and \hat{O}_2 , the single sided spectral density $S_{\hat{O}_1\hat{O}_2}(f)$ is defined by

$$\frac{1}{2} \langle 0 | (\hat{O}_1(\Omega)\hat{O}_2^\dagger(\Omega') + \hat{O}_2^\dagger(\Omega')\hat{O}_1(\Omega)) | 0 \rangle = \frac{1}{2} 2\pi\delta(\Omega - \Omega') S_{\hat{O}_1\hat{O}_2}(f). \quad (3.35)$$

The commutation relations of Eq. (3.29) and Eq. (3.34) show

$$\frac{1}{2} \langle 0 | (\hat{a}_j\hat{a}_k^\dagger + \hat{a}_k^\dagger\hat{a}_j) | 0 \rangle = \frac{1}{2} 2\pi\delta(\Omega - \Omega') \delta_{jk}. \quad (3.36)$$

Therefore, when the operator of the signal to noise ratio is described as the form of $x_{\text{snr}}(\Omega) = \eta_1\hat{a}_1 + \eta_2\hat{a}_2$, the power spectral density can be obtained by

$$S_x(f) = |\eta_1|^2 + |\eta_2|^2. \quad (3.37)$$

3. Quantum noise in optomechanical systems

Coherent state

The coherent state $|\alpha\rangle$ is defined by

$$|\alpha\rangle = \hat{D}(\alpha)|0\rangle \quad (3.38)$$

$$= \exp\left[\int_0^\infty \frac{d\omega}{2\pi} (\alpha_\omega \hat{a}_\omega^\dagger - \alpha_\omega^* \hat{a}_\omega)\right] |0\rangle. \quad (3.39)$$

The coherent state is the eigenstate of the eigenvalue α : $\hat{a}_\omega |\alpha\rangle = \alpha(\omega) |\alpha\rangle$. The operator $\hat{D}(\alpha)$ is called *the displacement operator*, and it is unitary: $\hat{D}^\dagger \hat{D} = \hat{I}$. Thus, we can replace the coherent state with the vacuum state by transforming the electric field according to

$$|\alpha\rangle \rightarrow |0\rangle, \quad \hat{E} \rightarrow \hat{D}^\dagger \hat{E} \hat{D}, \quad (3.40)$$

without changing physical quantities.

The single mode laser beam is modeled by the coherent state of $\alpha = A_0/\sqrt{2} \times 2\pi\delta(\omega - \omega_0)$. The electric field operator that incorporates the displacement operator is

$$\hat{E}_c(t) = \sqrt{\frac{4\pi\hbar\omega_0}{\varepsilon_0 c \mathcal{A}}} [(A_0 + a_1(t)) \cos \omega_0 t + a_2(t) \sin \omega_0 t], \quad (3.41)$$

which implies that it is the sum of a classical amplitude and quantum quadratures. The classical intensity of the electric field $P_A = |A_0|^2 \hbar\omega_0/2$.

3.3. Optomechanical systems

In this section, we review mathematical treatment of optomechanical systems. Firstly, we define a general definition for operators of optical fields. For an electromagnetic field \hat{A} , we write the expectation value as \mathbf{A} and the fluctuation as \mathbf{a} with quadrature decomposition:

$$\hat{A} = \sqrt{\frac{4\pi\hbar\omega_0}{\varepsilon_0 c \mathcal{A}}} (\mathbf{A} + \mathbf{a}) \cdot \begin{pmatrix} \cos \omega_0 t \\ \sin \omega_0 t \end{pmatrix}. \quad (3.42)$$

\mathbf{A} and $\mathbf{a}(\Omega)$ are vectors that consist of their amplitude quadrature and the phase quadrature:

$$\mathbf{A} = \begin{pmatrix} A_1 \\ A_2 \end{pmatrix}, \quad (3.43)$$

$$\mathbf{a} = \begin{pmatrix} a_1 \\ a_2 \end{pmatrix}. \quad (3.44)$$

\mathbf{A} consists of classical numbers, while \mathbf{a} can be a vector of operators.

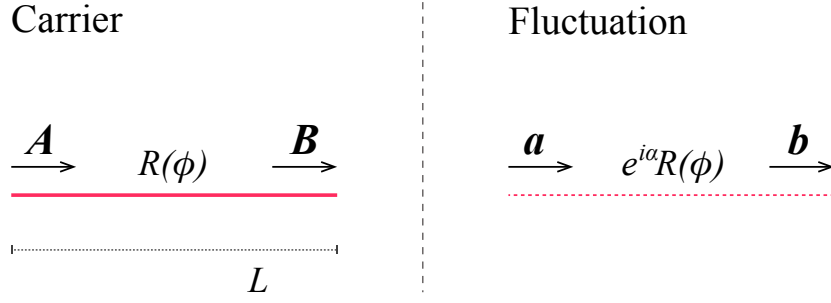


Figure 3.2.: Free space propagation

3.3.1. Dynamics of the electromagnetic field

Free space propagation

Let us consider the case of an electric field propagating in free space over a distance L , as shown in Fig 3.2. Since this is equivalent to time delay by $\tau = L/c$,

$$\hat{B}(t) = (A_1 + a_1(t - \tau)) \cos \omega_0(t - \tau) + (A_2 + a_2(t - \tau)) \sin \omega_0(t - \tau). \quad (3.45)$$

By calculating this equation, the output field is expressed as

$$B = R(\phi)A, \quad (3.46)$$

$$b(t) = R(\phi)a(t - \tau), \quad (3.47)$$

where $\phi = \omega_0\tau \pmod{2\pi}$ is the phase rotation by the propagation, and $R(\phi)$ is the rotational matrix:

$$R(\phi) = \begin{pmatrix} \cos \phi & -\sin \phi \\ \sin \phi & \cos \phi \end{pmatrix}. \quad (3.48)$$

The Fourier transform of the fluctuation of output electric field is

$$b(\Omega) = e^{i\alpha}R(\phi)a(\Omega), \quad (3.49)$$

where $\alpha = -\Omega\tau$ is the phase delay at the angular frequency Ω .

Transmission and reflection on a mirror

A mirror can be regarded as an optical element with two inputs and two outputs as shown in Fig. 3.3. Let the amplitude reflectivity and the amplitude transmissivity be r and t . When

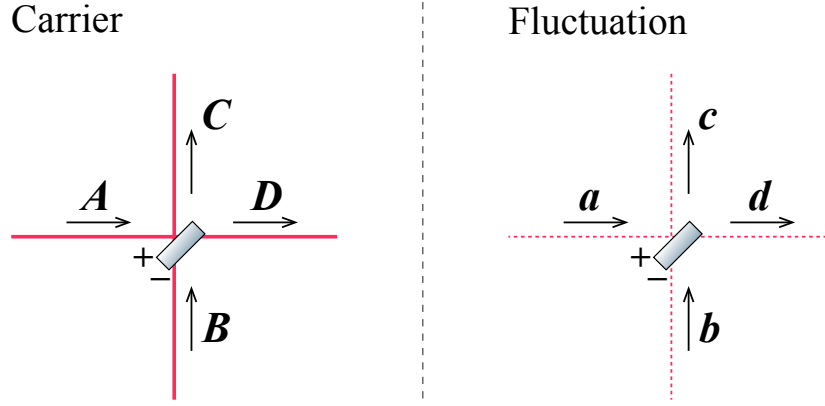


Figure 3.3.: Transmission and reflection on a mirror.

optical loss at the mirror is zero, $r^2 + t^2 = 1$ according to the energy conservation. The output fields are

$$\hat{C}(t) = r\hat{A}(t) + t\hat{B}(t), \quad (3.50)$$

$$\hat{D}(t) = t\hat{A}(t) - r\hat{B}(t). \quad (3.51)$$

Therefore, their quadratures and the fluctuations are

$$C = rA + tB, \quad (3.52)$$

$$D = tA - rB, \quad (3.53)$$

$$c(\Omega) = ra(\Omega) + tb(\Omega), \quad (3.54)$$

$$d(\Omega) = ta(\Omega) - rb(\Omega). \quad (3.55)$$

3.4. Modeling of a linear cavity

Cavities are a class of interferometer. Cavities allow light to circulate between mirrors that consist in them. Linear cavities are a simple cavity with two mirrors facing each other, as shown in Fig. 3.5. In this section, we review the mathematical description of the linear cavity and calculate quantum noise in it.

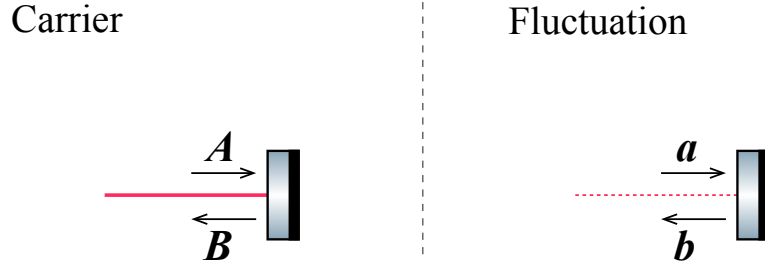


Figure 3.4.: Reflection on a free mass mirror.

3.4.1. Free mass mirror

To calculate the response of a linear cavity, firstly we consider the reflected light field on a free mass mirror, as described in Fig. 3.4. Here, we assume that the displacement of the mirror δx is small. The reflected light field will be

$$B(t) \simeq (A_1 + a_1(t) - 2A_2 k_0 \delta x(t)) \cos \omega_0 t + (A_2 + a_2(t) + 2A_1 k_0 \delta x(t)) \sin \omega_0 t, \quad (3.56)$$

where k_0 is the wave number of the optical field. This leads to

$$B = A, \quad (3.57)$$

$$b(t) = a(t) + 2k_0 \begin{pmatrix} -A_2 \\ A_1 \end{pmatrix} \delta x(t). \quad (3.58)$$

To obtain the Fourier transformation of Eq. (3.58), let us consider the equation of motion of the mirror. The radiation pressure due to the momentum transfer of the photons at the reflection is

$$F_{\text{rp}}(t) = 2\hbar k_0 \times \frac{1}{2} \left((A_1 + a_1(t))^2 + (A_2 + a_2(t))^2 \right). \quad (3.59)$$

The constant part of the radiation pressure is balanced by the mechanical restoring force. Thus, we need to consider only the fluctuation part of the radiation pressure: $\delta F_{\text{rp}}(t) \simeq 2\hbar k_0 (A_1 a_1(t) + A_2 a_2(t))$. When the external force $m \frac{d^2 x_{\text{ex}}(t)}{dt^2}$ is introducing the mirror displacement,

$$m \frac{d^2(\delta x(t))}{dt^2} = \delta F_{\text{rp}} + m \frac{d^2 x_{\text{ex}}(t)}{dt^2}. \quad (3.60)$$

We consider small displacements of the mirror; therefore, the equation of motion is identical to the one of classical theory, though the variables are replaced by the operators. The Fourier transform of this equation of motion leads to

$$\delta x(\Omega) = -\frac{2\hbar k_0}{m\Omega^2} (A_1 a_1(\Omega) + A_2 a_2(\Omega)) + x_{\text{ex}}(\Omega). \quad (3.61)$$

3. Quantum noise in optomechanical systems

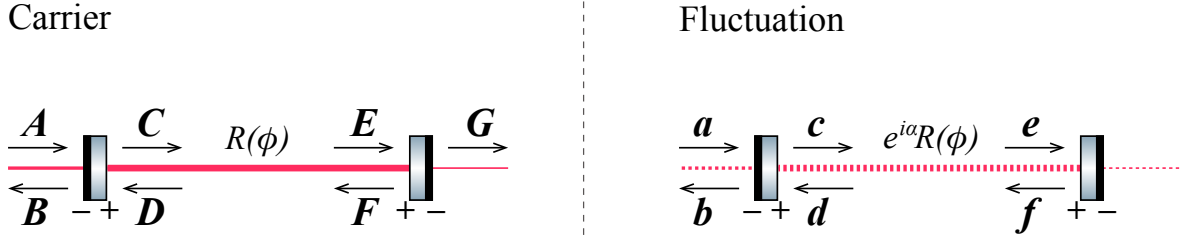


Figure 3.5.: A linear cavity.

Therefore, the Eq. (3.58) in the frequency domain is obtained as

$$b(\Omega) = P(\mathfrak{f}, \xi_A) a(\Omega) + \frac{\sqrt{2\mathfrak{f}}}{x_{\text{SQL}}} n_{A_{\perp}} x_{\text{ex}}(\Omega), \quad (3.62)$$

where we define

$$P(\mathfrak{f}, \xi_A) = R(\xi_A) \begin{pmatrix} 1 & 0 \\ -\mathfrak{f} & 1 \end{pmatrix} R(-\xi_A), \quad (3.63)$$

and the unit vector that perpendicular to the \mathbf{A} as

$$\mathbf{n}_{A_{\perp}} = \begin{pmatrix} -\sin \xi_A \\ \cos \xi_A \end{pmatrix}, \quad \xi_A = \arctan(A_2/A_1). \quad (3.64)$$

Here, \mathfrak{f} is represented by

$$\mathfrak{f} = \frac{8P_A \omega_0}{mc^2 \Omega^2}, \quad (3.65)$$

and called the optomechanical coupling constant. We also define the standard quantum limit of the mirror mass of m as

$$x_{\text{SQL}} = \sqrt{\frac{2\hbar}{m\Omega^2}}. \quad (3.66)$$

3.4.2. Linear cavity

Finally, we introduce quantum noise in a linear cavity as described in Fig. 3.5. Let the amplitude reflectivities of the input mirror and the end mirror be r_I and r_E , respectively. The amplitude transmissivities are $t_I = \sqrt{1 - r_I^2}$ and $t_E = \sqrt{1 - r_E^2}$. The cavity length is L , and the phase rotation due to propagating one way is $\phi = L\omega_0/c \pmod{2\pi}$.

For the classical electric fields, the relations between them are written as

$$\mathbf{B} = -r_1\mathbf{A} + t_1\mathbf{D}, \quad \mathbf{C} = t_1\mathbf{A} + r_1\mathbf{D}, \quad \mathbf{D} = R(\phi)\mathbf{F}, \quad \mathbf{E} = R(\phi)\mathbf{C}, \quad \mathbf{F} = r_E\mathbf{E}, \quad \mathbf{G} = t_E\mathbf{E}. \quad (3.67)$$

These relations lead to

$$\mathbf{B} = [-r_1I + t_1^2 r_E [I - r_1 r_E R(2\phi)]^{-1} R(2\phi)] \mathbf{A}, \quad (3.68)$$

$$= -r_1 A_0 \begin{pmatrix} 1 \\ 0 \end{pmatrix} + \frac{t_1^2 r_E A_0}{1 + r_1^2 r_E^2 - 2r_1 r_E \cos 2\phi} \begin{pmatrix} \cos 2\phi - r_1 r_E \\ \sin 2\phi \end{pmatrix}, \quad (3.69)$$

$$\mathbf{G} = t_1 t_E [I - r_1 r_E R(2\phi)]^{-1} R(\phi) \mathbf{A}, \quad (3.70)$$

$$= \frac{t_1 t_E A_0}{1 + r_1^2 r_E^2 - 2r_1 r_E \cos 2\phi} \begin{pmatrix} (1 - r_1 r_E) \cos 2\phi \\ (1 + r_1 r_E) \sin 2\phi \end{pmatrix}. \quad (3.71)$$

Since the light intensity is proportional to the square of the amplitude of the electric field, the (classical) intensity of the reflected light P_B , the (classical) intensity of the transmitted light P_G , and the (classical) intensity of the intracavity light P_E are written by

$$P_B = \frac{r_1^2 + r_E^2 - 2r_1 r_E \cos 2\phi}{1 + r_1^2 r_E^2 - 2r_1 r_E \cos 2\phi} P_A, \quad (3.72)$$

$$P_G = \frac{t_1^2 t_E^2}{1 + r_1^2 r_E^2 - 2r_1 r_E \cos 2\phi} P_A, \quad (3.73)$$

$$P_E = \frac{t_1^2}{1 + r_1^2 r_E^2 - 2r_1 r_E \cos 2\phi} P_A. \quad (3.74)$$

As inferred from the energy conservation, $P_B + P_G = P_A$. When $2\phi = 0 \pmod{2\pi}$, the intracavity (and the transmitted light) intensity is at its maximum, and the cavity is said to be resonant. The interval at which the resonance appears is called the Free Spectral Range (FSR), and the frequency interval of FSR f_{FSR} is

$$f_{\text{FSR}} = \frac{c}{2L}. \quad (3.75)$$

The Full Width at Half Maximum (FWHM) of the resonant peak f_{FWHM} is

$$f_{\text{FWHM}} = \frac{1 - r_1 r_E}{\pi \sqrt{r_1 r_E}} f_{\text{FSR}}, \quad (3.76)$$

while we assume the reflectivities of the mirrors are high (≈ 1). Finesse is a characteristic parameter of the cavity that is defined by the ratio of the FSR and the FWHM as

$$\mathcal{F} = \frac{f_{\text{FSR}}}{f_{\text{FWHM}}} = \frac{\pi \sqrt{r_1 r_E}}{1 - r_1 r_E} \approx \frac{2\pi}{t_1^2 + t_E^2}. \quad (3.77)$$

3. Quantum noise in optomechanical systems

Hereafter, we consider the case of the input mirror is fixed, and the end mirror behaves as a free mass. The reflectivity of the end mirror is one to maximize intracavity power ($r_1 = r$, $t_1 = t$, $r_E = 1$). The input-output relation for the fluctuations of the electric fields are

$$\mathbf{b} = -r\mathbf{a} + t\mathbf{d}, \quad \mathbf{c} = t\mathbf{a} + r\mathbf{d}, \quad \mathbf{d} = e^{i\alpha} R(\phi)\mathbf{f}, \quad (3.78)$$

$$\mathbf{e} = e^{i\alpha} R(\phi)\mathbf{c}, \quad \mathbf{f} = P(\xi, \xi_E)\mathbf{e} + \frac{\sqrt{2\mathfrak{f}}}{x_{\text{SQL}}}\mathbf{n}_{E\perp}x_{\text{ex}}(\Omega), \quad (3.79)$$

where $\alpha = -L\Omega/c$ is the phase rotation for the one way path. When the cavity is on resonance ($\phi = 0$), the coupling constant is reduced to be $\mathfrak{f} = 8P_E\omega_0/(mc^2\Omega^2) \simeq 16\mathcal{F}P_A\omega_0/(\pi mc^2\Omega^2)$. By solving Eq. (3.78) and Eq. (3.79) for \mathbf{b} ,

$$\mathbf{b} = \left[-rI + \frac{t^2 e^{2i\alpha}}{(1 - r e^{2i\alpha})^2} \begin{pmatrix} 1 - r e^{2i\alpha} & 0 \\ -\mathfrak{f} & 1 - r e^{2i\alpha} \end{pmatrix} \right] \mathbf{a} + \frac{t e^{i\alpha}}{(1 - r e^{2i\alpha})^2} \frac{\sqrt{2\mathfrak{f}}}{x_{\text{SQL}}} \begin{pmatrix} 0 \\ 1 - r e^{2i\alpha} \end{pmatrix} x_{\text{ex}}(\Omega). \quad (3.80)$$

If the transmission of the mirror t^2 and the phase delay α is small, then the fluctuation of the output field is reduced to

$$\mathbf{b} \simeq \frac{\gamma - i\Omega}{\gamma + i\Omega} \begin{pmatrix} 1 & 0 \\ -\frac{\gamma\iota}{\Omega^2(\gamma^2 + \Omega^2)} & 1 \end{pmatrix} \mathbf{a} + \frac{\gamma - i\Omega}{\sqrt{\gamma^2 + \Omega^2}} \frac{\sqrt{\frac{2\gamma\iota}{\Omega^2(\gamma^2 + \Omega^2)}}}{x_{\text{SQL}}} \begin{pmatrix} 0 \\ 1 \end{pmatrix} x_{\text{ex}}(\Omega), \quad (3.81)$$

where

$$\gamma = \frac{t^2 c}{4L}, \quad (3.82)$$

$$\iota = \frac{8P_E\omega_0}{mLc}. \quad (3.83)$$

By defining

$$\mathfrak{R} = \frac{\gamma\iota}{\Omega^2(\gamma^2 + \Omega^2)}, \quad (3.84)$$

$$\beta = \arctan(-\Omega/\gamma), \quad (3.85)$$

Eq. (3.81) is expressed by the simple form:

$$\mathbf{b} = e^{2i\beta} \begin{pmatrix} 1 & 0 \\ -\mathfrak{R} & 1 \end{pmatrix} \mathbf{a} + e^{i\beta} \frac{\sqrt{2\mathfrak{R}}}{x_{\text{SQL}}} \begin{pmatrix} 0 \\ 1 \end{pmatrix} x_{\text{ex}}(\Omega). \quad (3.86)$$

The first term represent the fluctuation of the electric field, and the second term represent the external force signal. The fluctuation of the electric field can be regarded as the noise. Then, the operator of the signal to noise ratio is

$$x_{\text{snr}}(\Omega) = \frac{x_{\text{SQL}}}{\sqrt{2\mathfrak{R}}} (-\mathfrak{R}a_1 + a_2) e^{i\beta}. \quad (3.87)$$

Thus, as we have seen in Eq. (3.37), the sensitivity for the external signal is described by the single sided power spectral density $S_x(\Omega)$:

$$S_x(\Omega) = \frac{x_{\text{SQL}}^2}{2} \left(\mathfrak{R} + \frac{1}{\mathfrak{R}} \right) > x_{\text{SQL}}^2. \quad (3.88)$$

The first term of Eq. (3.88) comes from the fluctuation in the amplitude quadrature of the input field, which is converted to the fluctuation in the phase quadrature through the response of the mirror. Thus, it corresponds to quantum radiation pressure fluctuation. On the other hand, the second term of Eq. (3.88) is the direct consequence of the fluctuation in the phase quadrature of the input field. Therefore, this noise corresponds to shot noise. There is a trade-off between these two quantum noises, with the standard quantum limit as the lower limit.

3.5. Summary of this chapter

In this chapter, we review calculations of quantum noise in optomechanical systems. For optomechanical systems, it is convenient to use two photon formalism. The basic dynamics of the optical field are free space propagation and reflection/transmission on a mirror. The dynamics in a linear cavity can be calculated by combining the two basic dynamics. The calculation results show that quantum noise can be divided into quantum shot noise and quantum radiation pressure noise based on the quadrature of its origin, and quantum noise limit the sensitivity by the standard quantum limit.

4. Experimental setup

As we have seen in Chapter 2, the milligram-scale optomechanical system is unique and crucial for macroscopic quantum experiment. In this chapter, we describe the experimental setup for realizing the milligram-scale optomechanical system. In Section 4.1, the design concept of our experiment is introduced. In particular, the cavity geometry is carefully designed to overcome the Sidles-Sigg instability. In Section 4.2, we focus on the main cavity in detail, while we discuss the auxiliary optics in Section 4.3. In Section 4.4, the feedback control systems that we use are introduced. The feedback control systems are used to keep the cavity resonance or to reduce noises for precise measurements. In Section 4.5, the systems to avoid environmental noises are introduced. In Section 4.6, let us summarize this chapter.

4.1. Design of the experiment

4.1.1. Goal and the paths

The goal of this research is to establish a class of precise optomechanical systems that are suspended linear cavities of milligram scale. We look ahead to macroscopic quantum experiments. Therefore, our experimental setup is designed to be sensitive for observing quantum radiation pressure fluctuation; as shown in Chapter 2, limitation by quantum radiation pressure fluctuation is one criterion of the quantum regime.

The first step for the goal is identifying a stable configuration of a suspended linear cavity. As we have seen in Section 2.4.2, a suspended linear cavity suffers from the Sidles-Sigg instability. To overcome the Sidles-Sigg instability, our optomechanical system has two characteristics. One is that the cavity is in the negative- g regime, and the other is the unbalanced masses of the cavity mirrors. The effectiveness and the experimental validation of our configuration is discussed in more detail in Chapter 5.

To complement our goal, we validate that the sensitive milligram-scale optomechanical systems are worthwhile for elucidating the nature of quantum mechanics. As a concrete implementation, we demonstrate one quantum noise reduction technique with our system, which is discussed in Chapter 6.

4. Experimental setup

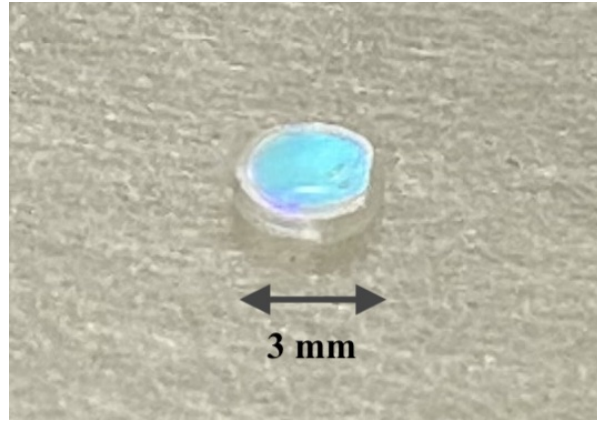


Figure 4.1.: Photographs of the 8-mg mirror. The high reflective coating and the anti-reflective coating are coated for each side, respectively.

Observation of quantum radiation pressure is the final aim for our experiment. Therefore, we propose and design a more suitable optomechanical oscillator for this purpose. The oscillator is a torsional pendulum. By constructing two linear cavities on the two edges of the torsional pendulum, the optomechanical system will be more robust against classical noises. We discuss replacing the simple pendulum with the torsional pendulum in Chapter 7.

4.1.2. 8-mg mirror as the test mass

To accomplish our goal, an 8 mg concave mirror is selected as the test mass. The small mass is advantageous to improve its force sensitivity, and the 8-mg mirror is the smallest suspended mirror with a curvature to the best of our knowledge.

The one side has the concave curvature with the high reflective coating. The curvature plays a crucial role for the stability of the rotational degrees of freedom of the cavity mirrors. The photograph of the 8-mg mirror is shown in Fig. 4.1.

4.1.3. Design sensitivity

We design the linear cavity with the sensitivity that is limited by quantum radiation pressure noise. The parameters for the design sensitivity to reach the quantum radiation pressure fluctuation are listed in Table 4.1. The calculated design sensitivity is described in Fig. 4.2. To estimate the mirror substrate and coating thermal noise, we refer to the material properties that are also listed in Table 4.1.

The calculation indicates that the quantum radiation pressure stands out if the input laser power is more than 10 mW. The other expected noises are estimated below the quantum radi-

Table 4.1.: Parameters for the design sensitivity towards observation of the quantum radiation pressure fluctuation.

Test mass mirror		
mass		8 mg
diameter		3 mm
radius of curvature		100 mm
reflectivity		99.99%
Q value		10^5
beam radius		0.21 mm
Young's modulus	substrate	73 GPa
	SiO ₂	73 GPa
	TiO ₂ :Ta ₂ O ₅	140 GPa
Poisson ratio	substrate	0.17
	SiO ₂	0.17
	TiO ₂ :Ta ₂ O ₅	0.28
loss angle	substrate	1×10^{-5}
	SiO ₂	1×10^{-4}
	TiO ₂ :Ta ₂ O ₅	4×10^{-4}
refractive index	substrate	1.45
	SiO ₂	1.45
	TiO ₂ :Ta ₂ O ₅	2.07
Input mirror		
mass		60 g
radius of curvature		100 mm
reflectivity		99.9%
Cavity		
cavity length		110 mm
finesse		5000
intracavity power		14 W
Laser		
wavelength		1064 nm
input power		10 mW
frequency noise		$10 \text{ Hz}/f \text{ Hz}/\sqrt{\text{Hz}}$
temperature		300 K
air pressure		10^{-4} Pa

4. Experimental setup

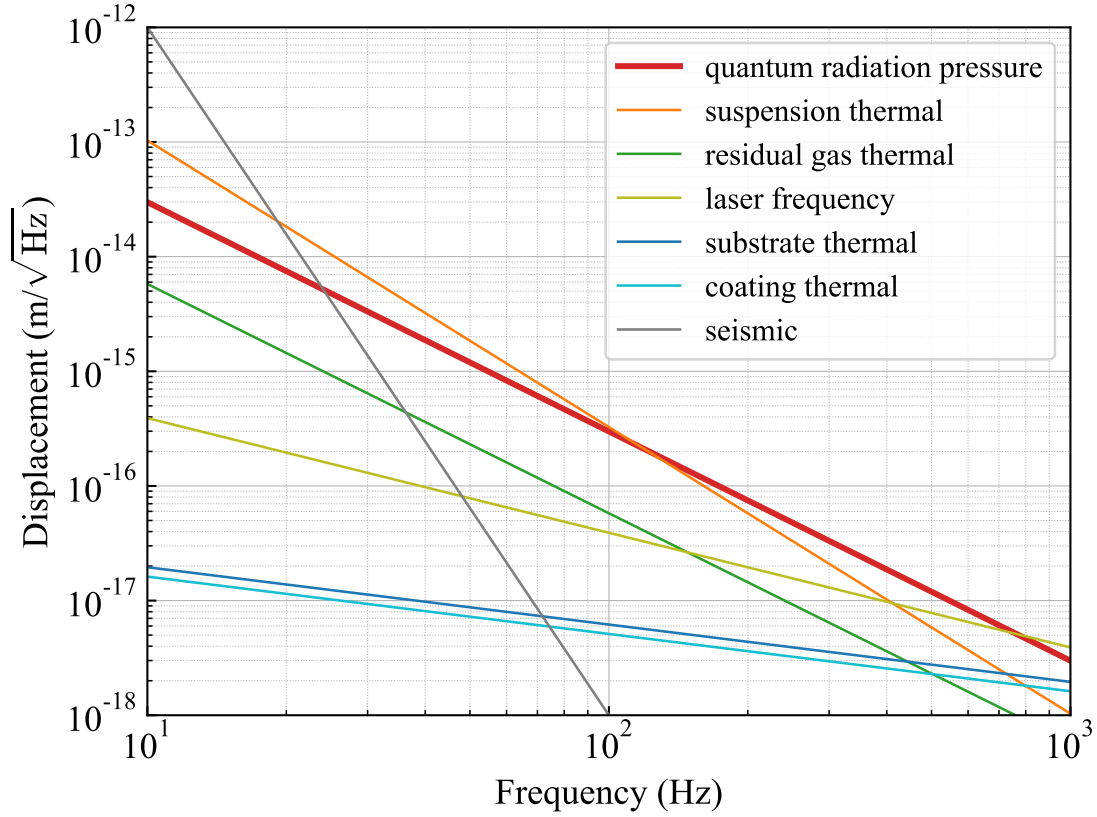


Figure 4.2.: Design sensitivity of the linear cavity for observing quantum radiation pressure fluctuation. The quantum radiation pressure fluctuation can be observed in the range between 120 Hz and 750 Hz. Quantum radiation pressure noise is calculated as shown in Chapter 3. The suspension thermal noise is estimated by using Eq. (2.6). The residual gas thermal noise is based on Eq. (2.6), while the laser frequency noise is determined by the cavity length and the laser frequency stability as shown in Eq. (2.12). The mirror substrate and coating thermal noises are evaluated using Eq. (2.8) and Eq. (2.9), respectively. The seismic noise is introduced in Eq. (2.13).

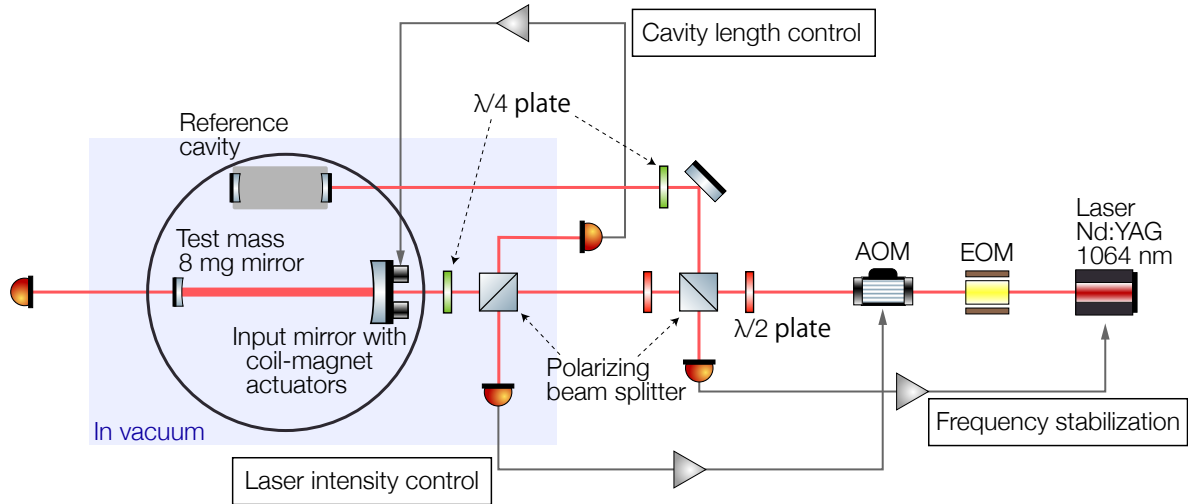


Figure 4.3.: Schematic drawings of the experimental setup.

ation pressure fluctuation in the frequency band between 120 Hz and 750 Hz.

Before moving onto the overview of the experimental setup, we have a note for the classical radiation pressure noise, which is omitted from the plotting. We assume a feedback control for the laser intensity stabilization. For the intensity stabilization, a part of the input laser beam towards the main cavity is picked up, and the intensity is measured with a photo detector. The measured intensity fluctuation is the error signal of the feedback control. The intensity stability will be limited by the shot noise level of the picked up light. Thus, the higher the power of the picked up light gets, the closer the classical radiation pressure noise is to the quantum radiation pressure noise. When the half power of light is picked up, the classical radiation pressure noise is above the quantum radiation pressure noise by the factor of $\sqrt{2}$. The design value of the input power is 10 mW, and our laser source is 2 W power. Therefore, we assume that the intensity stabilization can utilize enough high laser power, and when the classical radiation pressure noise is equal to the quantum radiation pressure noise, we regard the sensitivity of the system as reaching the quantum radiation pressure noise.

4.1.4. Overview of the setup

In this section, our whole experimental setup is outlined. Figure. 4.3 describes the schematic drawings of our experimental setup. The setup consists of the following four parts: the main cavity, the auxiliary optics, the feedback control systems, and the environmental noise isolation systems.

4. *Experimental setup*

The main cavity is a suspended linear cavity. The 8 mg test mass mirror and the input mirror of a half-inch mirror are suspended as double pendulums on the platform. The auxiliary optics include the input optics and the output optics. The laser source is an Nd:YAG laser of wavelength 1064 nm. The phase of the laser beam is modulated for the cavity length control through the electro-optical modulator (EOM). The amplitude of the laser is also modulated for the intensity stabilization through acousto-optical modulator (AOM). From the input optics, two laser beams are injected towards the vacuum chamber where the main platform is built. The transmitted lights from the cavities come out through the vacuum chamber and detected by photo detectors.

We introduce three feedback controls. One is the main cavity length control to keep the resonance or to sustain a certain locking point. The other one is the laser intensity stabilization. A part of the laser beam is picked up for the intensity stabilization before entering the main cavity. For the laser frequency stabilization, the reference cavity is on the platform next to the main cavity. The laser frequency is feedback controlled to the frequency reference, which is the resonant frequency of the reference cavity.

The platform is suspended as a double pendulum with coil springs in the vacuum chamber. The spring suspension is introduced to reduce the seismic noise in both vertical and horizontal directions. The vacuum chamber prevent the air turbulence and the residual gas noise.

By calibrating the photo detector signal of the reflected light from the main cavity, we can estimate the displacement of the test mass mirror. The displacement is due to residual noises for the external forces since we do not apply intended external forces in this experiment. After the classical noises are suppressed enough, the quantum radiation pressure noise dominates.

4.2. Main cavity

The central optomechanical system in the experiment is the main cavity with the 8-mg mirror. In this section, we focus on the main cavity. The main cavity is a suspended linear cavity and composes of the suspended 8-mg mirror and the suspended input mirror. Let us describe one by one in the following sections.

4.2.1. Test mass mirror

Substrate

The test mass mirror is the 8-mg mirror that is suspended with a fiber. The mirror is cylindrical in shape, with a diameter of 3 mm and a thickness of 0.5 mm. The dimensions of the test mass mirror are decided to prevent the larger clipping of the beam. One side of it is coated with a

Table 4.2.: Material properties of the fibers used in the experiment.

	Carbon fiber	Tungsten fiber	CuBe fiber
Tensile strength	5.9 GPa	3.8 GPa	1.4 GPa
Young's modulus	294 GPa	345 GPa	130 GPa
Density	$1.81 \times 10^3 \text{ kg/m}^3$	$19.3 \times 10^3 \text{ kg/m}^3$	$8.25 \times 10^3 \text{ kg/m}^3$

high reflective coating whose reflectivity is 99.99 (+0.005/−0.02)%. The other side is coated with an anti-reflective coating whose reflectivity is less than 0.15%. The mirror is concave on the side of the high reflective coating. The radius of curvature is 100 mm.

The test mass should be as light as possible for a precise force measurement. However, it is not easy to achieve both the requirement of the small mass and with curvature, and 8 mg is the smallest suspended mirror with curvature. The mirror is produced by Sigma-koki company based on custom order.

Suspension system

The suspension fiber should be thin to reduce its suspension thermal noise. We can use a thin fiber by choosing a high tensile strength fiber. Consequently, a carbon fiber is selected to suspend the test mass mirror. The carbon fiber is attached to the mirror with ultraviolet curing resin. Although a tungsten fiber is also a high tensile strength fiber, a metal fiber has a residual stress that curves the fiber. Thus, carbon fiber is preferable for suspending a tiny mirror. The properties of the fiber are listed in Table 4.2. The carbon fiber is also advantageous by its low density. The suspension thermal noise of the violin mode can be reduced by making the violin mode frequency high enough. Since the frequency of the violin mode is inversely proportional to the square root of the density, we avoid the effect of suspension thermal noise of the violin mode by using low-density fiber whose density is one-tenth that of a metal fiber.

The measured intrinsic Q value of the carbon fiber is $\sim 2.5 \times 10^3$. The Q value of the pendulum is enhanced by the gravitational dilution effect. For the pendulum mode, a fiber has energy loss only near the clamp point. Thus, the Q value is improved by a dilution factor than the intrinsic Q value of the fiber. The dilution factor α_{di} is described as

$$\alpha_{\text{di}} = \frac{l_f}{\phi_f^2} \sqrt{\frac{128mg}{\pi E_f}}, \quad (4.1)$$

where l_f is the fiber length, ϕ_f is the diameter, E_f is the Young's modulus of the fiber, and m is the mass of the pendulum. In our experiment, we have a benefit of $\alpha_{\text{di}} \sim 60$ as the dilution

4. Experimental setup

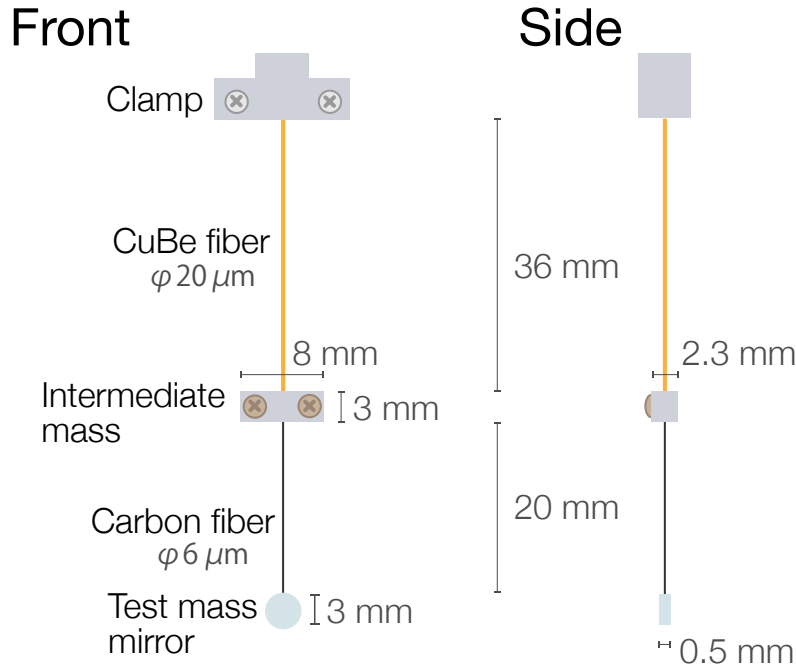


Figure 4.4.: Schematic drawings of the suspended test mass mirror.

factor. Therefore, the Q value in the pendulum mode is expected to be $\sim 1.5 \times 10^5$, which satisfies the requirement value of the experimental design of 10^5 .

The test mass mirror is suspended as a double pendulum for locking the cavity by suppressing the residual motion of test mass mirror. The schematic drawings of the suspended test mass is shown in Fig. 4.4. For the intermediate mass in the double pendulum, we introduce magnetic damping to suppress the residual motion of the test mass mirror. The intermediate mass is surrounded by a ring neodymium magnet. To avoid unwanted magnetic attraction, the intermediate mass is made of highly pure aluminum of 99.999% (5N). The carbon fiber is fixed to the intermediate mass with a pure aluminum lid and peak screws. The mass of the intermediate mass is measured to be 129.5 ± 0.1 mg. For the optimal damping, the mass should approach the mass of the test mass mirror. Therefore, the intermediate mass is designed to be small, while it also needs to work as a clamp.

The intermediate mass is suspended from the clamp with a CuBe fiber. The CuBe fiber is attached to the intermediate mass with ultraviolet curing resin. The CuBe fiber is selected because CuBe fibers have small Young's modulus and high intrinsic Q value. The properties of the CuBe fiber is also listed in Table 4.2.

A photograph of the suspension system and the test mass mirror is shown in Fig. 4.5. At the top of the suspension, a rotation stage is used with a picomotor for the remote control of

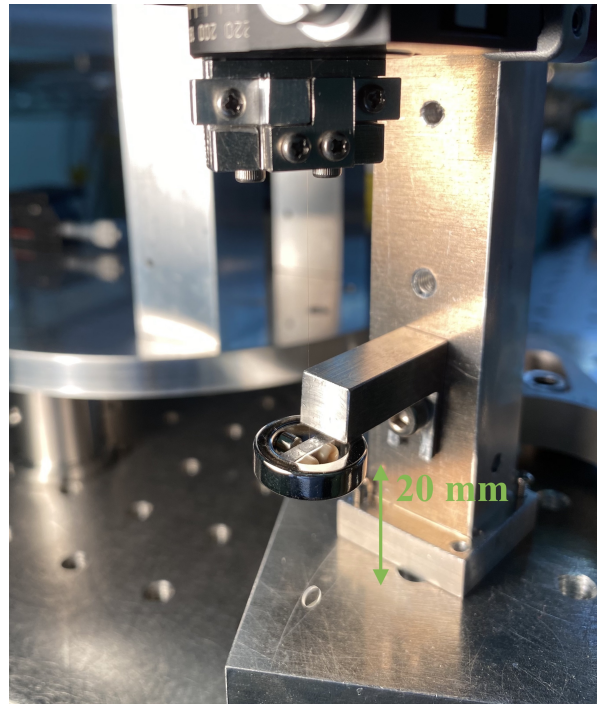


Figure 4.5.: Photograph of the suspension and the test mass mirror.

the yaw angle of the test mass mirror. The test mass mirror is placed on the platform in the vacuum chamber.

4.2.2. Controlled input mirror

The input mirror has coil-magnet actuators to control the cavity length. A half inch mirror is stuck in a brass mirror holder to compose the input mirror of 60 g. With the mirror holder, the input mirror is much heavier than the test mass mirror by three orders of magnitude. The mirror is fixed to the holder with ultra-violet curing resin. The properties of the input mirror is listed in Table 4.3.

The input mirror is also suspended as a double pendulum to isolate it from the seismic vibration. In addition, by suspending the input mirror, we can have an enough actuator range to lock the cavity. The schematic drawings of the suspension for the input mirror is shown in Fig.4.6. The brass input mirror holder has a cylindrical shape, and two grooves are carved into the side for hooking wires. Two loops of wire is clamped to the intermediate mass and hook the input mirror holder. The intermediate mass has a rectangular shape and is made of copper. Copper has a high electrical conductivity, and is suitable for magnetic damping. For the magnet damping, four neodymium magnets are placed near the intermediate mass. Piano wires of 0.1 mm diameter are used to suspend the input mirror and the intermediate mass. A

4. Experimental setup

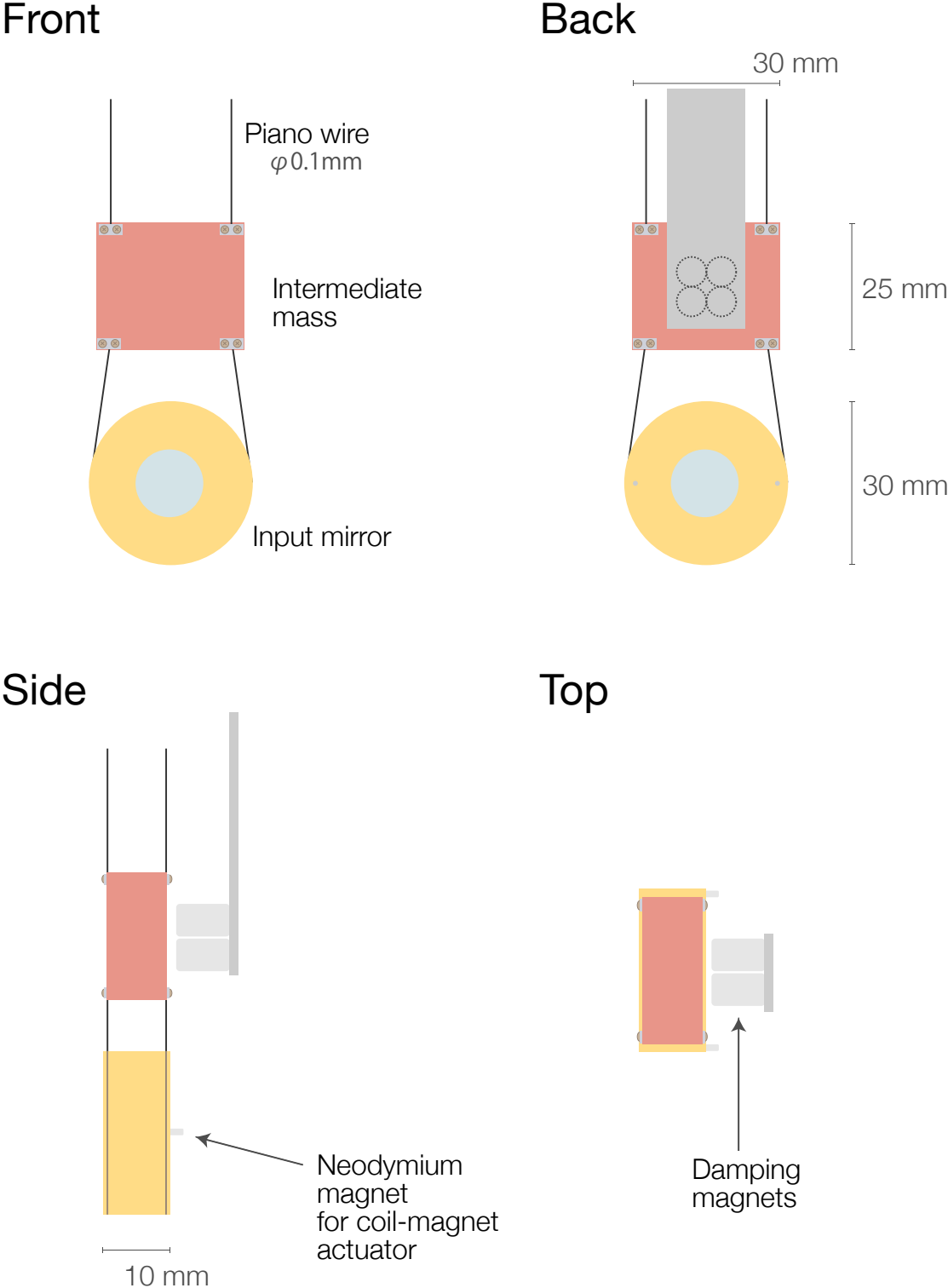


Figure 4.6.: Schematic drawings of the suspension for the controlled input mirror.

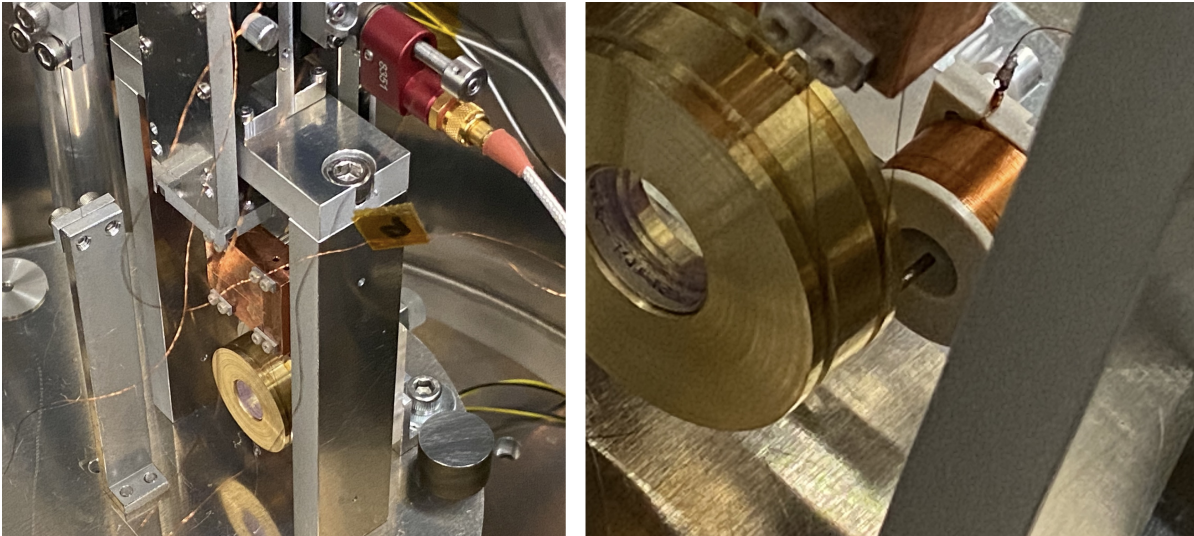


Figure 4.7.: Photographs of the controlled input mirror. The coil-magnet actuator is focused on the right panel.

piano wire has an advantage in its strength, though it can not be get ultra thin. Thin aluminum plates are screwed together to clamp the wires.

On the top of the suspension, there are two translation stages connected to the two suspension wires. By moving the stage, the pitch and yaw rotations are controlled. Picomotors are attached to the stage, and the rotational alignment of the input mirror can be adjusted remotely.

Two neodymium magnets are attached to the input mirror holder for the coil-magnet actuators. The coil-magnet actuators are used for the cavity length control and for the transfer function measurement of the rotational degree of freedom. Photographs of the controlled input mirror are shown in Fig. 4.7.

To calibrate the signal from the cavity to the displacement of the test mass mirror, the actuator efficiency need to be known in advance. Therefore, we measure the actuator efficiency of the

Table 4.3.: Properties of the input mirror.

Diameter	12.7 mm
Thickness	6.35 mm
Front surface curvature	(100.0 ± 0.5) mm
Rear surface curvature	∞ mm
Front surface reflectivity	$(99.90 \pm 0.02)\%$
Rear surface reflectivity	$< 0.25\%$

4. Experimental setup

coil-magnet actuator by building a Michelson interferometer. The controlled input mirror is placed as one end mirror of the Michelson interferometer. We feedback control the Michelson interferometer at the middle fringe with the coil-magnet actuator. The transfer function of a Michelson interferometer from the displacement of the end mirror to the output signal is determined by the laser frequency. Thus, the actuator efficiency is estimated by the feedback control gain. The measured actuator frequency is $H_{\text{act}} = (3.0 \pm 0.3) \times 10^{-4}$ N/V.

4.2.3. Cavity properties

The cavity length is decided as 110 mm. The short cavity length is advantageous in terms of frequency noise, though it must be longer than the curvatures of the cavity mirrors for the stable configuration. The resulting g factor is -0.1 . Thus the cavity is in the negative- g regime. The test mass mirror of 8 mg is much lighter than the controlled input mirror of 60 g. Therefore, the two conditions for the stable suspended linear cavity are satisfied, as explained in detail in Chapter 5. The expected finesse value is 5700, which meets the parameter of the design sensitivity. The measured cavity length is (110 ± 3) mm.

4.3. Auxiliary optics

4.3.1. Input optics

The input optics are assembled to condition the laser beams entering the cavities. The laser source is an Nd:YAG laser of the wave length 1064 nm; its maximum output power is 2 W. The laser beam passes through a Faraday isolator to dump the returning light. A part of the beam is split for the optical lever to monitor the yaw rotation of the platform. The beam for the optical lever is reflected at the mirror attached on the side of the platform. The returning light is detected by a quadrant photo detector. The signal indicates the rotational motion. A neodymium magnet is attached to the mirror on the side of the platform, and a coil is placed near the magnet to compose a coil-magnet actuator. The yaw mode of the platform is feedback controlled to keep its angle with the optical lever and the coil-magnet actuator. The unity gain frequency of the feedback control is around 1.0 Hz not to disturb a signal within the frequency range of interest.

The main beam is phase-modulated through an electro-optical modulator and amplitude-modulated through an acousto-optical modulator. After the modulations, the beam is again separated by a polarizing beam splitter; one goes to the main cavity, and the other goes to the reference cavity. From the main cavity beam, a half of the beam is picked up and monitored for the intensity stabilization. The optical path length and the positions of the lenses are tuned so

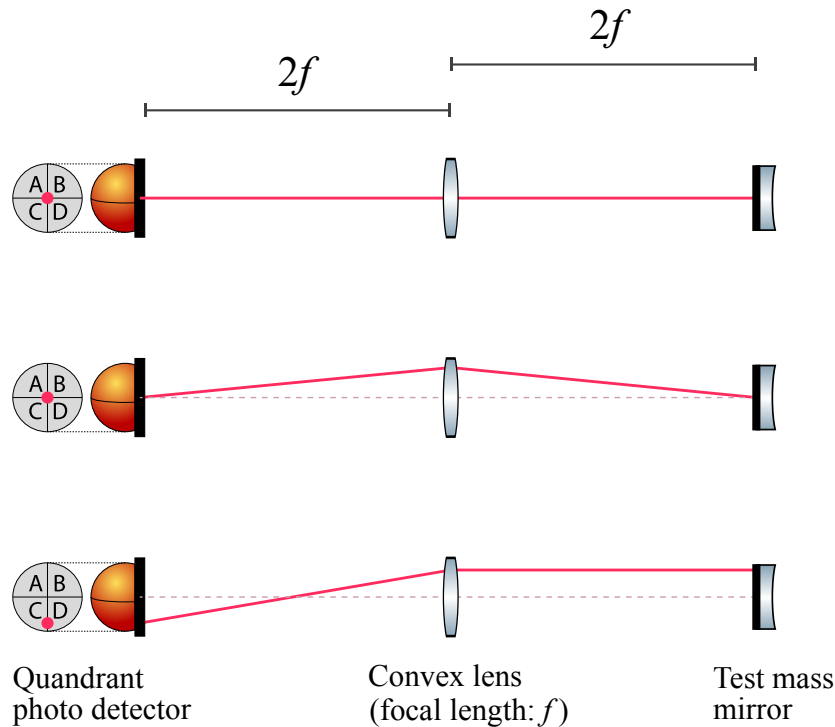


Figure 4.8.: The monitor system for the transmitted light from the main cavity. It is designed to be sensitive only to changes in the beam spot, not to beam tilt. A convex lens of the focal length f is located in the middle of the quadrant photo detector and the test mass mirror, where the beam spot is measured. The distances between the lens and the quadrant photo detector and the test mass mirror are adjusted to be $2f$. With this configuration, tilt of the beam is cancelled by the lens.

that the mode of the laser beam match the cavity mode. Two steering mirrors with picomotors are used for the path of the main cavity to align the beam to the cavity axis precisely.

4.3.2. Output optics

The output optics include two photo detectors and two CCD cameras; one is used for the transmitted light from the main cavity, and the other monitors the transmitted light from the reference cavity, which is described in the next section. The photo detectors measure the power of the laser beam, and the CCD cameras are used to monitor the beam shape and to confirm the resonance. For the main cavity, a quadrant photo detector is used to measure the beam spot as well. The beam spot can be measured by using a convex lens and a quadrant photo detector as shown in Fig. 4.8. Tilt of the laser beam is cancelled by the convex lens. Thus, we can measure only the beam spot displacement, while it is insensitive to tilt.

4.4. Feedback controls

4.4.1. Laser frequency stabilization

In optomechanical systems, the fluctuation in the laser frequency is indistinguishable from the displacement of the oscillator. The target observation bandwidth is between 120 Hz and 750 Hz. To achieve the sensitivity, the laser frequency noise should be less than $10 \text{ Hz}/f \text{ Hz}/\sqrt{\text{Hz}}$, while the naive laser frequency stability is about $10^4 \text{ Hz}/f \text{ Hz}/\sqrt{\text{Hz}}$ for a typical NPRO laser source.

Therefore, we utilize the reference cavity to attain the stability in the laser frequency. The reference cavity is a rigid cavity, and the laser frequency is fixed to the resonant frequency of the reference cavity. The laser frequency is stabilized at the level of the stability of the reference cavity. The spacer of the reference cavity is made of super invar. Super invar is a nickel-iron alloy, and is known for its uniquely low coefficient of thermal expansion. On the spacer, two high-reflective mirrors are attached with screws to comprise a high finesse cavity. The parameters of the reference cavity is shown in Table 4.4.

To fix the laser frequency to the resonant frequency of the reference cavity, a feedback control is introduced. The error signal is obtained by Pound-Drever-Hall technique. The error signal is filtered to be the feedback signal, and the feedback signal is applied to the laser source to actuate the frequency of the laser beam. Let us describe the Pound-Drever-Hall signal in more detail. The phase of the laser frequency is modulated before entering the reference cavity with electro-optical modulator. The modulation frequency is 15 MHz. With 15-MHz sine wave, we demodulate the signal that is obtained by the photo detector sensing the reflected light from the reference cavity. To respond to 15-MHz signal, we use InGaAs photodiodes (Hamamatsu Photonics G10899). The filter circuit is consists of a low-pass filter and a high-pass filter. the high-pass filter is necessary to compensate the phase delay, and the low-pass

Table 4.4.: Parameters of the reference cavity.

Finesse	5.2×10^4
Cavity length	44 mm
Free spectral range	3.4 Ghz
High reflective coating reflectivity	99.994%
Anti-reflective coating reflectivity	<0.2%
Curvature	1000 mm
Finesse (design)	5.2×10^4
Finesse (measured)	6.1×10^4

filter is necessary for a stable feedback control. The feedback signal is sent to the piezoelectric actuator that is attached to the laser crystal in the laser head.

4.4.2. Laser intensity stabilization

Laser intensity stabilization is also implemented since laser intensity fluctuation gives the classical radiation pressure fluctuation. To obtain an error signal, a part of the laser source is picked up from the input laser beam to the main cavity. As an actuator, the acousto-optical modulator in the input optics is used to modulate the intensity of the passing beam.

4.5. Environmental-noise isolation

4.5.1. Vibration isolation

The sensitive optics including the main cavity and the reference cavity are placed on the platform. The platform has to be well isolated from the seismic motion for the cavity locking and for the sensitivity. For this purpose, the platform is suspended with springs as a double pendulum. Coil springs are introduced to isolate the vertical seismic motion as well as the horizontal motion. Since it is a double suspension, the seismic noise can be reduced by $1/f^4$.

The suspension of the platform is schematically shown in Fig. 4.9. The main platform is suspended from the roof of the outer structure by a single wire. Although it is technically easier to suspend the platform with three wires, three-wire suspension can introduce a large seismic noise since the resonant frequencies of the pitch and bounce mode will get close. For the suspension, we joint piano wires of diameter 0.2 mm and coil springs with aluminum clamps. Consequently, the yaw mode of the platform is soft. Thus, we introduce an optical lever and an additional coil-magnet actuator to suppress the yaw motion of the platform.

The whole building is on three fluorine rubber piles. The outer structure is constructed with a floor, a roof and three poles. The roof suspends the intermediate mass of 1.8 kg and the damping mass of 4.4 kg. The damping mass is made of magnetized stainless steel and suspended with three piano wires and coil springs. Eight neodymium magnets are attached to the damping mass for the magnetic damping of the intermediate mass. The intermediate mass is made of copper and suspended with a piano wire and a coil spring. From the intermediate mass, the platform is suspended, and the mass of the platform is 1.8 kg.

4. Experimental setup

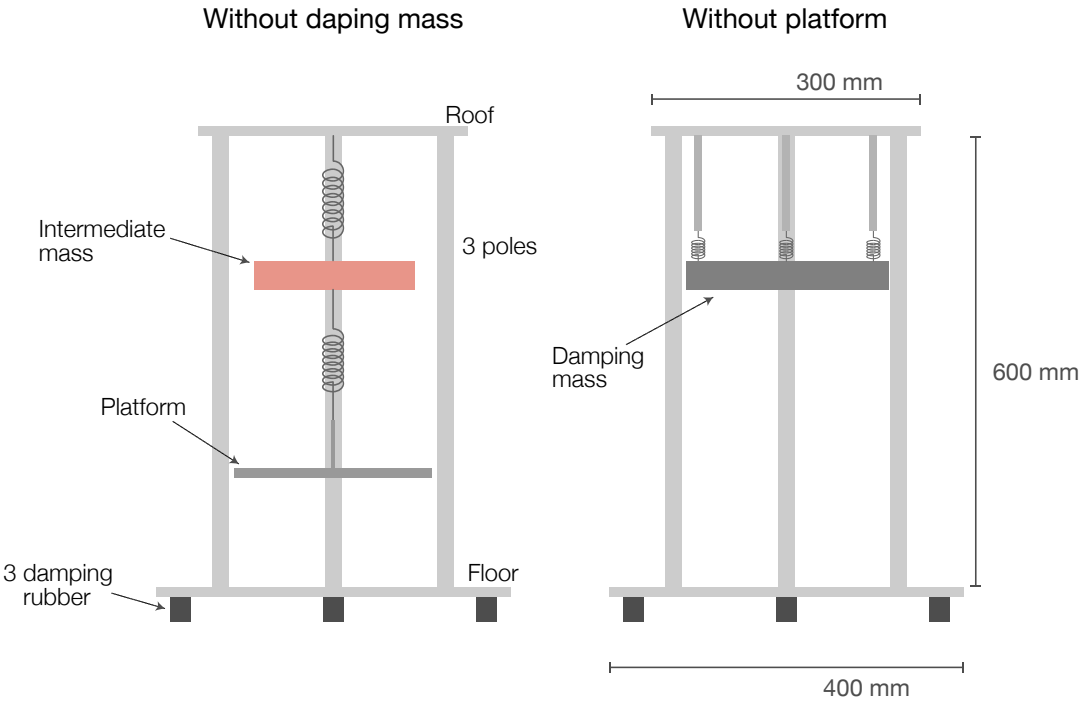


Figure 4.9.: Schematic image of the platform suspension.

4.5.2. Vacuum system

The platform where the main cavity and the reference cavity are built is suspended in the vacuum chamber to avoid the air turbulence and the noise of the residual gas. The input laser beam enters from the right-side view port window on the vacuum chamber. The view port window is anti-reflective coated to minimize the unwanted scattering of the light. The platform is located in the right side of the vacuum chamber. In the left side of the vacuum chamber, some output optics are located. The vacuum pumps and the vacuum gauge are connected to the left side of the chamber. They consist of the rotary pump of Edwards RV12 and the turbo molecular pump of Osaka vacuum TG450F. The first evacuation is done with the rotary pump, and when the pressure drops below 10 Pa, the turbo molecular pump is used to evacuate to 10^{-4} Pa.

The schematic picture of the vacuum chamber is shown in Fig. 4.10. The vacuum chamber consists of two jointed vacuum tank. The input light come from the right side of the chamber. The platform is installed in the right side chamber. In the left chamber, the vacuum pump is attached.

4.6. Summary of this chapter

For macroscopic quantum experiments, we construct a suspended linear cavity with 8-mg mirror. The light mass is advantageous in force measurements. With feedback controls and environmental-noise isolation, the design sensitivity reach quantum radiation pressure noise.

4. Experimental setup

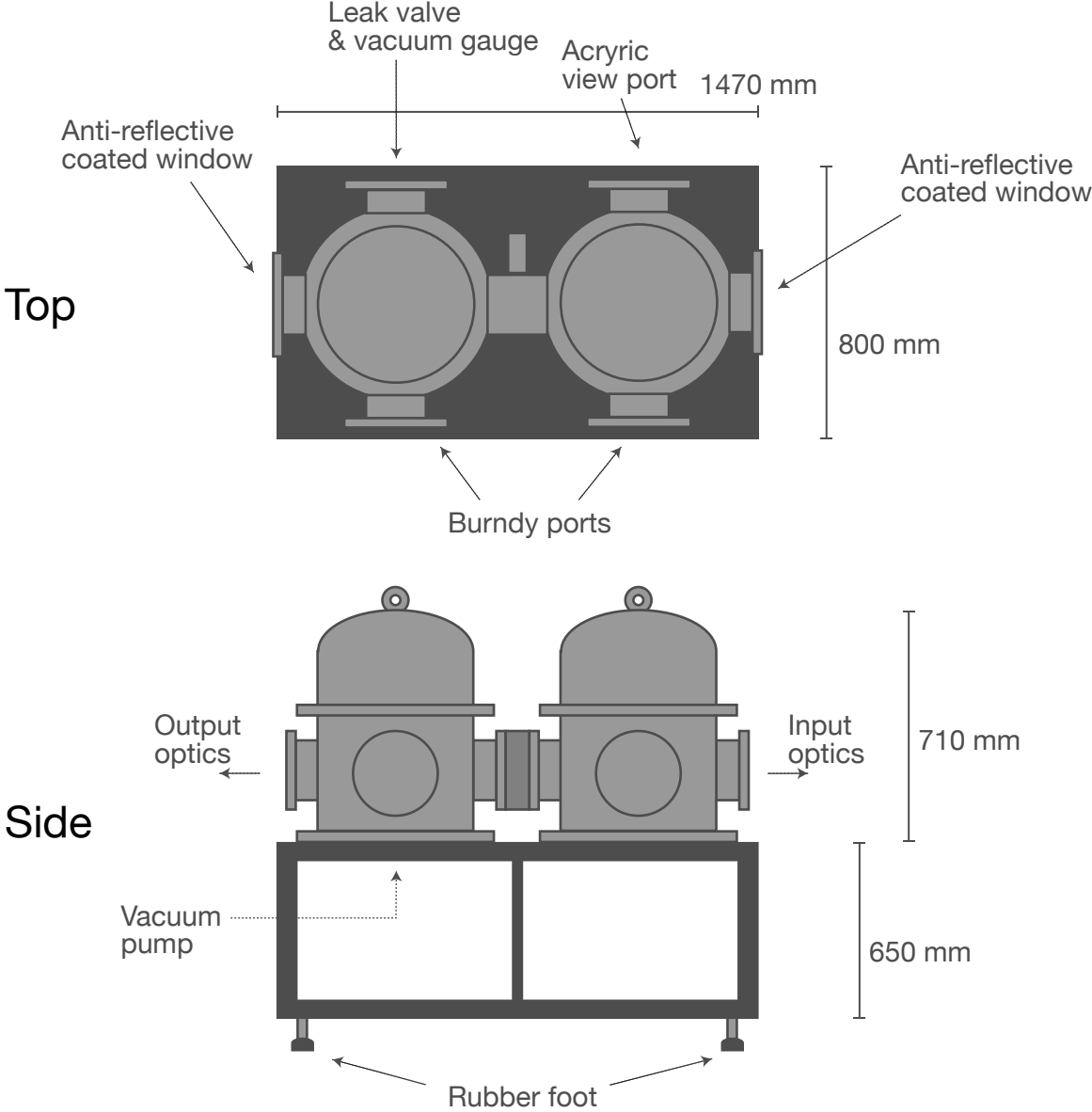


Figure 4.10.: Schematic picture of the vacuum chamber.

5. Angular trapping of a linear-cavity mirror with an optical torsional spring

5.1. Preface

Our ultimate goal is observing quantum radiation pressure fluctuation. Thus, a linear cavity is employed for our milligram-scale optomechanical system to optimize its sensitivity. As we have seen, however, a suspended linear cavity has the difficulty related to the Sidles-Sigg instability. Therefore, the configuration of the cavity is carefully designed to overcome the Sidles-Sigg instability. In this chapter, we discuss the method to realize a stable suspended linear cavity in detail. In addition, the experiment that validates the trapping configuration is also provided in this chapter. The invented configuration with the experimental validation plays a key role for milligram-scale optomechanical systems. This is a joint research by K. Komori, H. Fujimoto, Y. Michimura, M. Ando, and myself. The works covered by the present chapter are primary done by myself. Its preprint can be found in arXiv:2110.13507 [90].

5.2. Theoretical description of the trapping scheme

In this section, we analyze the rotational motion of suspended mirrors in a linear cavity while taking the effect of the radiation pressure. The calculation is based on the procedure shown in [91]. The previous works [91] assumed that the cavity mirrors had identical masses because the stability was discussed in the context of gravitational wave detectors. By considering the general case of cavity masses, we identify a stable trapping configuration for a suspended linear cavity. The following calculation clarifies that the suspended mirrors are trapped with the positive radiation pressure torque under the condition that the cavity is in the negative- g regime and one mirror is much heavier than the other one. We name the trapping effect *optical torsional spring*.

The schematic picture of a suspended linear cavity considered here is shown in Fig. 5.1.

5. Angular trapping of a linear-cavity mirror with an optical torsional spring

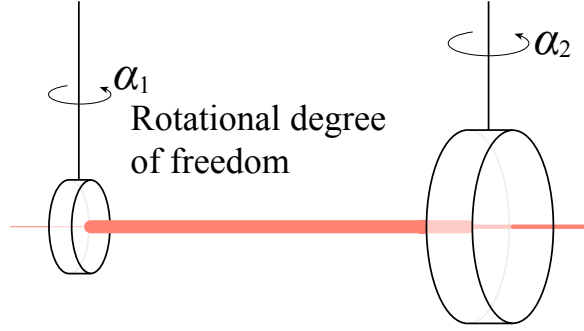


Figure 5.1.: Schematic picture of a suspended linear cavity. The rotational degrees of freedom we focus on are defined along the vertical axis. The input mirror is much heavier than the end mirror for our configuration.

Each mirror is suspended, and what we consider here is the rotational degree of freedom along its vertical axis. As shown in Fig. 5.1, we define the angles of two mirrors as α_i and the torques exerted to them as T_i ($i = 1, 2$). The equation of motion of the rotational modes of the two mirrors is given by

$$(\mathbf{K}_{\text{opt}} + \mathbf{K}_{\text{mech}} - \mathbf{I}\omega^2) \begin{pmatrix} \alpha_1 \\ \alpha_2 \end{pmatrix} = \begin{pmatrix} T_1 \\ T_2 \end{pmatrix}, \quad (5.1)$$

where

$$\mathbf{K}_{\text{mech}} = \begin{pmatrix} K_1 & 0 \\ 0 & K_2 \end{pmatrix}, \quad \mathbf{I} = \begin{pmatrix} I_1 & 0 \\ 0 & I_2 \end{pmatrix} \quad (5.2)$$

are the matrices of the mechanical restoring torques and the moment of inertia of each mirror. Here, we consider the case that the rotational motion of the mirrors are slow enough to ignore the phase delay of the light propagating inside the cavity. The optical torsional stiffness matrix is represented as [47]

$$\mathbf{K}_{\text{opt}} = \frac{2P}{c(R_1 + R_2 - L)} \begin{pmatrix} R_1(L - R_2) & R_1R_2 \\ R_1R_2 & R_2(L - R_1) \end{pmatrix}, \quad (5.3)$$

where P , R_1 , and L are the intracavity power, the radii of curvature, and the cavity length, respectively. Equation. (5.1) can be rewritten as [91]

$$\begin{pmatrix} K_1 - \beta g_2 - I_1\omega^2 & \beta \\ \beta & K_2 - \beta g_1 - I_2\omega^2 \end{pmatrix} \begin{pmatrix} \alpha_1 \\ \alpha_2 \end{pmatrix} = \begin{pmatrix} T_1 \\ T_2 \end{pmatrix}, \quad (5.4)$$

by defining

$$\beta = \frac{2PL}{c(1 - g_1g_2)}, \quad (5.5)$$

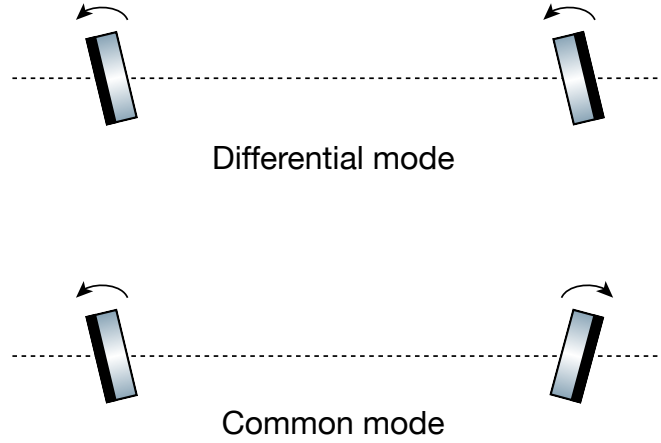


Figure 5.2.: Definition of the common mode and the differential mode of the cavity mirrors.

and $g_i = 1 - L/R_i$. g_i depends on the geometry of the cavity, and it is generally called g factor.

Hereafter, we consider a case where the mirror 2 is much heavier than the mirror 1, and the mechanical restoring torque of the mirror 1 is much smaller than that of the mirror 2. This assumption is practical for actual experiments. This optomechanical system can be a sensitive force sensor by using the lighter mirror as a test mass. At the same time, we can control the cavity length to maintain the cavity resonance by attaching actuators on the larger (heavier) mirror. Therefore, we consider the case that $I_1 \ll I_2$ and $K_1 \ll K_2$. In this case, the diagonalization of Eq. (5.4) indicates the resonant frequency of the differential mode is

$$\omega_{\text{diff}} \simeq \sqrt{\frac{K_1 - \beta g_2}{I_1}}, \quad (5.6)$$

where we define the differential mode as the diagonalized mode where the mirror 1 and 2 rotate in the same directions. We also define the common mode as the diagonalized mode of the rotation where two mirrors rotate in the different directions as shown in Fig. 5.2.

When the lighter mirror is flat ($g_1 = 1$), g_2 should be positive to satisfy optical cavity condition of $0 < g_1 g_2 < 1$. In this case, the resonant frequency rapidly goes to zero with increase of the intracavity laser power, which causes an angular instability. On the other hand, we can avoid the instability and even can stiffen the differential mode in the negative- g regime. Eq. (5.4) also indicates the resonant frequency of the common mode decreases as

$$\omega_{\text{com}} \simeq \sqrt{\frac{K_2 + \beta(1 - g^2)/g}{I_2}}. \quad (5.7)$$

Here, we consider the case that the two curvatures of the mirrors are identical ($R_1 = R_2 = R$, $g_1 = g_2 = g$) for simplicity. An important fact here is that the mechanical resonant frequency

5. Angular trapping of a linear-cavity mirror with an optical torsional spring

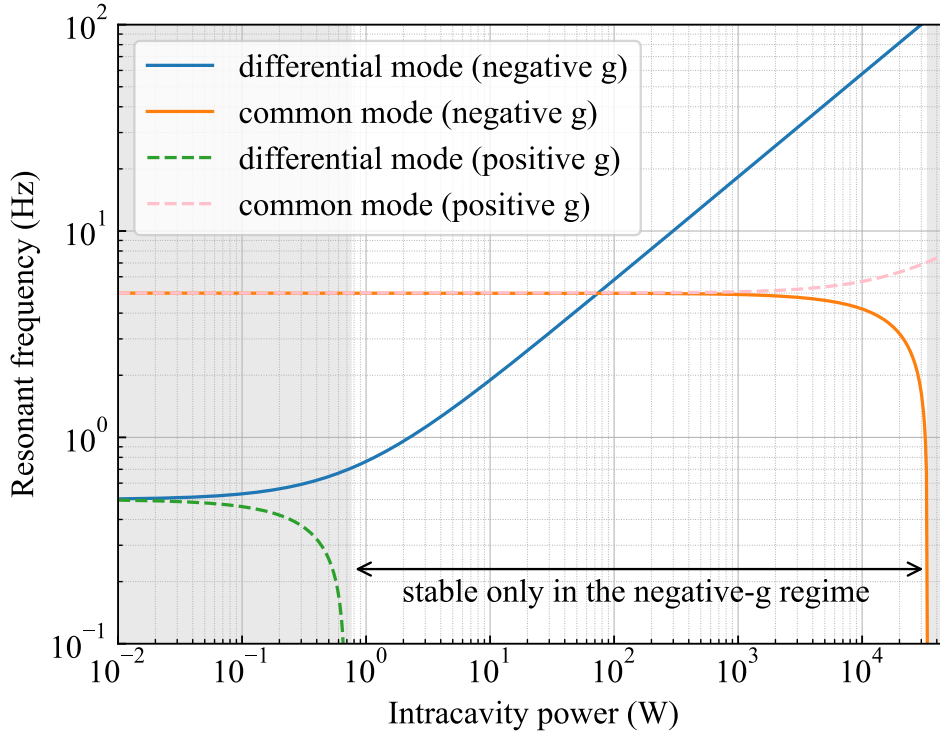


Figure 5.3.: Dependence of the resonant frequencies of differential and common modes. The negative resonant frequency implies that the mode is unstable. For comparison, both the negative- g regime ($g_1 = g_2 = -0.1$) and the positive- g regime ($g_1 = 1$, $g_2 = +0.1$) cases are plotted; other parameters are described in the main text. In the range between 0.75 W and 34 kW of the intracavity power, only the negative- g cavity is stable.

of the common mode can be high enough by using an enough heavy mirror for the mirror 2. Therefore, the decrease of the common mode resonant frequency due to the radiation pressure torque can be ignored with unbalanced-mass mirrors. In other words, the radiation pressure torque will not make the common mode unstable when one mirror is much heavier than the other. Optical spring effect in the direction of the cavity axis is well known; thus, we name the trapping effect in the rotational degrees of freedom for *optical torsional spring* after it.

Figure 5.3. shows the dependence of the resonant frequency on the intracavity power. As for this plot, we use similar parameters of our experimental setup as follows: mirror masses of $m_1 = 10$ mg and $m_2 = 10$ g, mirror radii of $r_1 = 1.5$ mm and $r_2 = 10$ mm, (momentum of inertia of $I_1 = 5.6 \times 10^{-12}$ kg m² and $I_2 = 2.5 \times 10^{-7}$ kg m²), mechanical resonant frequency of $\omega_1/(2\pi) = 0.5$ Hz and $\omega_2/(2\pi) = 5$ Hz, and the cavity length of $L = 1.1R = 11$ cm ($g = -0.1$).

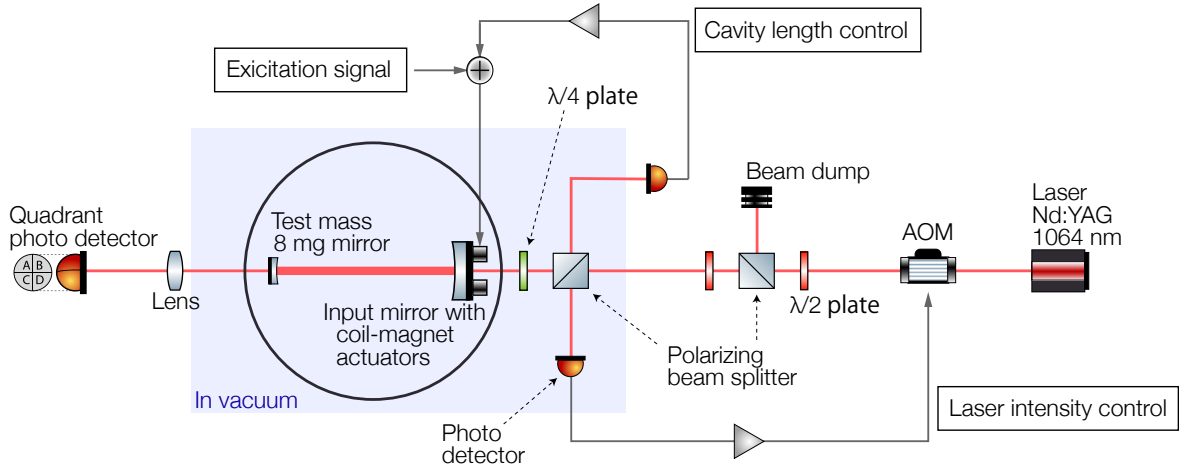


Figure 5.4.: Schematic drawing of the experimental setup for the demonstration of the optical torsional spring. For this experiment, we use a quadrant photo detector at the transmitted light from the main cavity. The beam spot on the test mass is monitored with a lens and the quadrant photo detector for the transfer function measurement. The reference cavity is not used here since the laser frequency noise does not affect the intracavity power. Therefore, the reference cavity is omitted in the diagram to emphasize this fact, though it is still there. The cavity length is feedback controlled for the continuous resonance. The laser intensity fluctuation is also suppressed by the feedback control with an acousto-optic modulator.

For comparison, we also plot the resonant frequencies of the differential and common modes for the case that the milligram-scale mirror is flat and the g factor of the heavier mirror is positive ($g_2 = +0.1$). The cavity in the negative- g regime is tolerant over the intracavity power of 10 kW, while the cavity with the flat mirror is unstable just over 0.75 W.

5.3. Experimental demonstration

We identify the stable configuration for suspended linear cavities. The configuration is a key for high sensitivities in milligram-scale optomechanical systems, and it is adopted in our experimental setup. Our experimental setup is the first realization and demonstration of the optical torsional spring. For the validation, we conduct evaluations of the optical torsional spring.

5.3.1. Method

With the experimental setup, we demonstrate that our trapping configuration works properly. The configuration utilizes the radiation pressure of the laser light inside a linear cavity. Thus, the restoring torque due to the radiation pressure also increase as the intracavity power increases. The validity of our trapping configuration is justified by observing this increase of the restoring torque due to the optical torsional spring.

The experimental setup for this demonstration is shown in Fig. 5.4. During this demonstration, we do not use the laser frequency stabilization system since the frequency noise does not affect the stability of the cavity. The instability due to the radiation pressure of the laser light inside the cavity will be an issue when the radiation pressure torque is dominant. The predominance of the radiation pressure is realized because we build a linear cavity with a tiny mirror of 8 mg that is suspended with a thin carbon fiber. The small mass allows to use the ultra thin fiber, and thus the mechanical restoring torque is much smaller than that of the radiation pressure. The carbon fiber is 6 μm in diameter and 20 mm long, and the resulting rotational resonant frequency is 0.6 Hz. The measured value is 0.64 ± 0.01 Hz. The cavity length is measured to be 110 ± 3 mm, and the radii of curvature of the mirrors are 100.0 ± 0.5 mm. The g factor of the cavity is -0.1. During this demonstration, the pressure is kept about 1 Pa to suppress acoustic disturbances. It is relatively low vacuum for the stable locking of the cavity. The pressure is tuned so that the residual gas introduces gas damping without disturbing the cavity locking.

To show the radiation pressure works as a positive restoring torque, we evaluate the resonant frequency that is described in Eq. (5.6). The resonant frequency is determined by the transfer function of the rotational motion of the mirrors. Figure 5.5 show the schematic picture of the transfer function measurement. To measure the transfer function, we apply a torque to the input mirror by injecting differential sine-wave signals into the coil-magnet actuators on the input mirror. Then, the test mass is also swung via the radiation pressure inside the cavity. The rotation of the test mass results in the changes of the beam spot on the test mass because the cavity axis changes. We observe the transmitted light from the cavity by a quadrant photo detector with a convex lens to detect the change in the beam spot. The transfer function from the injected signal to the quadrant photo detector signal of the horizontal direction includes the transfer function of the suspended mirrors [85]. Therefore, the transfer function has the characteristic form of the resonant peak. We fit the transfer function to estimate the resonant frequency. We note that the cavity length is feedback controlled to keep the resonance of the cavity during this transfer function measurement.

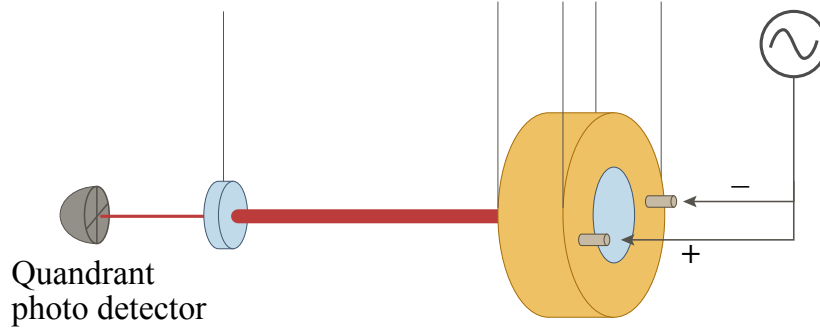


Figure 5.5.: Schematic picture of the transfer function measurement in the rotational degree of freedom. Differential sine-wave signals are injected into the coil-magnet actuators on the input mirror to excite the rotational motion of the mirrors. The transfer function from the excitation signal to the quadrant photo detector's signal is measured.

5.3.2. Results and discussion

The measured transfer functions from the excitation to the quadrant photo detector signal are plotted in Fig. 5.6. We measure them with five different intracavity powers. The peaks and the phase flips due to the resonance of the test mass are clearly observed in each measurement. We fit the gain of the transfer functions to determine the resonant frequency. The fitted parameters are resonant frequency, damping ratio of the resonance, and the overall gain factor. The fitted curves are also plotted in Fig. 5.6.

The intracavity power in each measurement is estimated with the transmitted light power by dividing the reflectivity of the test mass mirror. The uncertainty in the intracavity power is dominated by the fluctuation in the power of the transmitted light. The fluctuation in the transmitted light power is at the frequency of the excitation signal. Thus, it is inferred that the fluctuation would be due to the misalignment when the mirror is swung.

We show the dependence of the resonant frequency on the intracavity power in Fig. 5.7. The uncertainty of the resonant frequency comes from the frequency-bin width of the transfer function measurement. We also show the predicted region from the theoretical calculation using Eq. (5.6) with the parameters of the optics. The width of the region corresponds to the uncertainty of the design reflectivities of the mirrors and the uncertainty of the cavity length.

The measured dependency is consistent with the theoretical prediction. Therefore, we conclude that we observe the optical torsional spring. The results prove the configuration traps the suspended cavity mirrors, and they show the certification of the ability of accumulating intracavity power as much as the design value of 14 W for observing quantum radiation pressure fluctuation thanks to the optical torsional spring.

5. Angular trapping of a linear-cavity mirror with an optical torsional spring

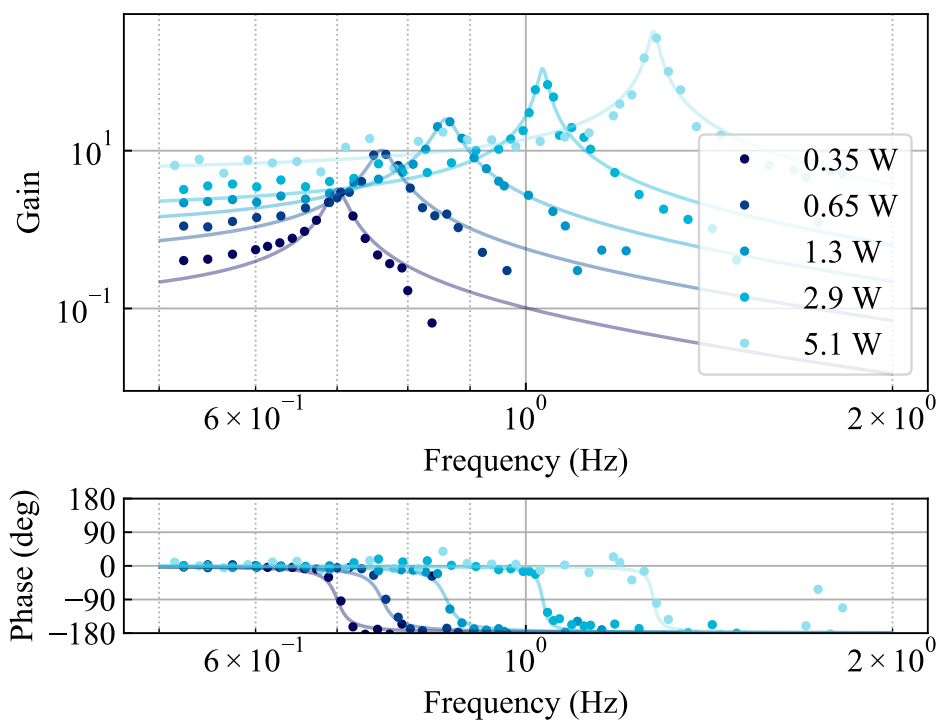


Figure 5.6.: The measured transfer functions of the five measurements of different intracavity powers. The points are the measured data, and the lines represent the fittings. The peaks and the phase flips indicate the resonant points. By the fitting, we estimate the resonant frequencies.

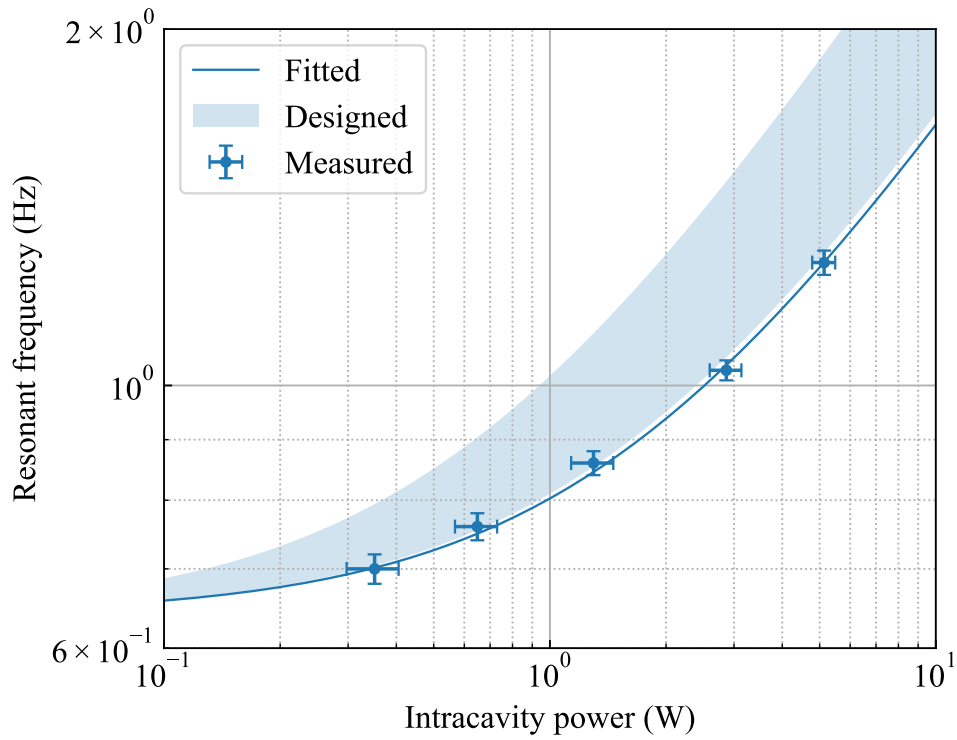


Figure 5.7.: The resonant frequencies of the differential mode in the rotational degree of freedom. The shaded region represents the theoretically predicted values with the width corresponding to the uncertainties in mirror reflectivities and the cavity length.

5.4. Summary of this chapter

We identify a configuration to trap the rotational motions of the suspended mirrors in a linear cavity. By operating a linear cavity in the negative- g regime and using unbalanced-mass mirrors, the two rotational modes of the cavity mirrors are stabilized with the radiation pressure inside the cavity. Moreover, we demonstrate the first experimental validation of the trapping with our experimental setup. We observe the rotational restoring torque on the mirror increases as the intracavity power increases. The behavior is consistent with theoretical prediction. Therefore, we confirm that the 8 mg test mass mirror gets the positive restoring torque originated from the radiation pressure of the inside laser beam. We conclude with this demonstration that we have established the stable configuration of the suspended linear cavity, and the experimental setup can accumulate enough laser power to observe quantum radiation pressure fluctuation.

6. Proof-of-principle demonstration of quantum noise cancellation

6.1. Preface

We have established the stable configuration of a suspended linear cavity. This achievement opens up new potentials for linear cavities as sensitive force sensor. As the proof of it, we demonstrate a quantum noise reduction technique with our experimental setup. In addition to proving the usefulness of the system as a force sensor, this demonstration also has the aspect of research for further sensitivity improvement after quantum radiation pressure noise limits the sensitivity.

In this chapter, we start by analyzing a method to enhance the sensitivity of a quantum optomechanical system, followed by the experimental demonstration. This is a joint work by K. Komori, S. Otabe, Y. Enomoto, Y. Michimura, M. Ando, and myself. It is published in *Phys. Rev. A Letter* **104** L031501 [92]. The theoretical description is derived with heading efforts by K. Komori. As for the experimental demonstration, all measurements shown here are conducted by myself.

6.2. Principle of quantum noise cancellation

The quantum noise can be cancelled by measuring the reflected light from a detuned linear cavity, as schematically described in Fig. 6.1. In this section, let us consider the principle



Figure 6.1.: Schematic description of quantum noise cancellation. The amplitude fluctuation in the light that directly reflected on the front mirror can negate the amplitude fluctuation in the transmitted light from the cavity.

6. Proof-of-principle demonstration of quantum noise cancellation

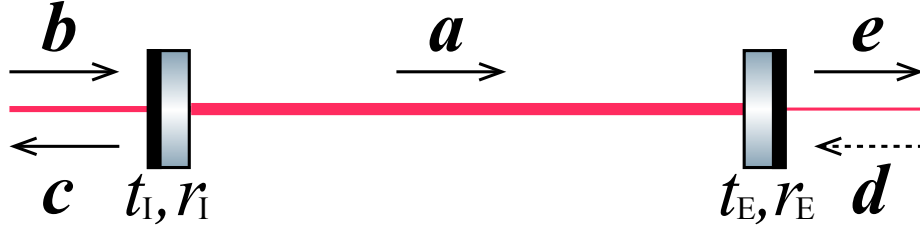


Figure 6.2.: Optical fields for the considered cavity.

of the quantum noise cancellation in a linear cavity. The end mirror behaves as an harmonic oscillator. The transmissivity and reflectivity of the end mirror are t_E and r_E , respectively. The input mirror is fixed, and its transmissivity and reflectivity are t_I and r_I . Because the system we consider is a linear cavity, the optical losses in the system can be regarded as the nonzero transmissivity of the end mirror.

To calculate the quantum noise, we use the two photon formalism [87–89] as presented in Chapter 3. In the two photon formalism, we deal with an optical field as a pair of quadratures. Thus, an optical field can be represented as a vector, $\mathbf{a} = (a_1 \ a_2)^t$, where a_1 is an amplitude quadrature and a_2 is a phase quadrature. Let us define each optical field as follows: \mathbf{a} is the optical field in the cavity, $\mathbf{b}(\mathbf{c})$ is the optical field going into (out from) the input mirror, and $\mathbf{d}(\mathbf{e})$ is the optical field going into (out from) the end mirror. The definition of the fields are shown in Fig. 6.2.

The cavity amplification matrix between the amplitude and phase of the light is represented as [92]

$$\mathbf{G} = \frac{c}{2L} \frac{1}{(\kappa - i\omega)^2 + \Delta^2} \begin{pmatrix} \kappa - i\omega & -\Delta \\ \Delta & \kappa - i\omega \end{pmatrix}, \quad (6.1)$$

where L is the cavity length, $\kappa = (t_I^2 + t_E^2) c / (4L)$ is the cavity decay rate, and Δ is the cavity detuning.

We assume the optomechanical system is macroscopic. In that case, the end mass is heavy enough to have a low mechanical resonant frequency. The frequency region of interest is above the resonant frequency. Thus, the end mirror motion is in the free-mass regime, and the displacement response to a force is $\chi_m \simeq -1/(m\omega^2)$, where m is the effective mass of the mirror.

In the case that the cavity is detuned, the phases of the optical fields are different. The difference of the phase is expressed by a rotation matrix

$$\mathbf{R}_\theta = \begin{pmatrix} \cos \theta & -\sin \theta \\ \sin \theta & \cos \theta \end{pmatrix}. \quad (6.2)$$

The intracavity field is enhanced by the cavity amplification synchronizing with the cavity displacement. The loop gain of the cavity is

$$\mathcal{A} = \begin{pmatrix} 0 & 0 \\ -\kappa_0 & 0 \end{pmatrix} \mathbf{G}, \quad (6.3)$$

where $\kappa_0 = -8\chi_m P k_0 / c$. The cavity response to the input field can be written as

$$\mathbf{H} = \frac{\mathbf{G}}{\mathbf{I} - \mathcal{A}} \quad (6.4)$$

$$= -\frac{c\omega^2}{2LM} \begin{pmatrix} \kappa - i\omega & -\Delta \\ \Delta - \iota/\omega^2 & \kappa - i\omega \end{pmatrix}, \quad (6.5)$$

where \mathbf{I} is an unit matrix, and

$$\mathcal{M} = \omega^2[(\omega + i\kappa)^2 - \Delta^2] + \Delta\iota. \quad (6.6)$$

ι in the above expression is defined as

$$\iota = \frac{4Pk_0}{mL}, \quad (6.7)$$

which indicates the optomechanical coupling strength. P is the intracavity power and k_0 is the wave number of light; $k_0 = 2\pi/\lambda$.

By calculating $\text{Re}(\mathcal{M}) = 0$, the resonant frequency of the optical spring can be obtained as

$$\omega_{\text{opt}} = \sqrt{\frac{\Delta\iota}{\kappa^2 + \Delta^2}}. \quad (6.8)$$

The input-output relations of the reflected light and the transmitted light are

$$\begin{pmatrix} c_1 \\ c_2 \end{pmatrix} = \mathbf{R}_\alpha \left\{ [t_1^2 \mathbf{H} - r_1 \mathbf{I}] \mathbf{R}_\beta \begin{pmatrix} b_1 \\ b_2 \end{pmatrix} + t_1 t_E \mathbf{H} \begin{pmatrix} d_1 \\ d_2 \end{pmatrix} + 2\chi_m A k_0 t_1 \mathbf{H} \begin{pmatrix} 0 \\ \delta F \end{pmatrix} \right\}, \quad (6.9)$$

and

$$\begin{pmatrix} e_1 \\ e_2 \end{pmatrix} = [t_E^2 \mathbf{H} - r_E \mathbf{I}] \begin{pmatrix} d_1 \\ d_2 \end{pmatrix} + t_1 t_E \mathbf{H} \mathbf{R}_\beta \begin{pmatrix} b_1 \\ b_2 \end{pmatrix} + 2\chi_m A k_0 t_E \mathbf{H} \begin{pmatrix} 0 \\ \delta F \end{pmatrix}. \quad (6.10)$$

The difference in the phase of the carriers are given by

$$\alpha = \arctan \left(-\frac{\Delta}{2\kappa_{\text{in}} - \kappa} \right), \quad (6.11)$$

$$\beta = \arctan \left(-\frac{\Delta}{\kappa} \right), \quad (6.12)$$

$$\gamma = \arctan \left(\frac{2\kappa_{\text{in}}\Delta}{2\kappa\kappa_{\text{in}} - \kappa^2 - \Delta^2} \right), \quad (6.13)$$

6. Proof-of-principle demonstration of quantum noise cancellation

where α is the phase difference between the intracavity and the reflected light, β is the phase difference between the input and the intracavity light, and $\gamma = \alpha + \beta$ is the phase difference between the input and the reflected light. The input and output coupler κ_{in} , κ_{out} are defined as $\kappa_{\text{in}} = t_1^2 \kappa / (t_1^2 + t_E^2)$, $\kappa_{\text{out}} = \kappa - \kappa_{\text{in}}$.

Here, let us consider amplitude measurements. To calculate the sensitivity of amplitude measurements, we pay attention to the amplitude quadrature. The amplitude of the reflection is given by

$$c_1 = \chi_{\text{ref}} (\delta F + \xi_{b_1} b_1 + \xi_{b_2} b_2 + \xi_{d_1} d_1 + \xi_{d_2} d_2), \quad (6.14)$$

where

$$\chi_{\text{ref}} = 2\chi_m A k_0 t_1 (H_{12} \cos \alpha - H_{11} \sin \alpha), \quad (6.15)$$

$$\xi_{b_1} = [t_1^2 (H_{11} \cos \gamma + H_{12} \cos \alpha \sin \beta - H_{21} \sin \alpha \cos \beta) - r_1 \cos \gamma] / \chi_{\text{ref}}, \quad (6.16)$$

$$\xi_{b_2} = [t_1^2 (-H_{11} \cos \gamma + H_{12} \cos \alpha \cos \beta + H_{21} \sin \alpha \sin \beta) + r_1 \sin \gamma] / \chi_{\text{ref}}, \quad (6.17)$$

$$\xi_{d_1} = \frac{t_E}{2\chi_m A k_0} \frac{H_{11} \cos \alpha - H_{21} \sin \alpha}{H_{12} \cos \alpha - H_{11} \sin \alpha}, \quad (6.18)$$

$$\xi_{d_2} = \frac{t_E}{2\chi_m A k_0}. \quad (6.19)$$

H_{ij} ($i, j = 1, 2$) is the component of the matrix \mathbf{H} . Note that $H_{11} = H_{22}$. The amplitude of the transmission is calculated as

$$e_1 = \chi_{\text{tra}} (\delta F + \eta_{b_1} b_1 + \eta_{b_2} b_2 + \eta_{d_1} d_1 + \eta_{d_2} d_2), \quad (6.20)$$

where

$$\chi_{\text{tra}} = 2\chi_m A k_0 t_E H_{12}, \quad (6.21)$$

$$\eta_{b_1} = \frac{t_1}{2\chi_m A k_0} \frac{H_{11} \cos \beta + H_{12} \sin \beta}{H_{12}}, \quad (6.22)$$

$$\eta_{b_2} = \frac{t_1}{2\chi_m A k_0} \frac{-H_{11} \sin \beta + H_{12} \cos \beta}{H_{12}}, \quad (6.23)$$

$$\eta_{d_1} = \frac{t_E^2 H_{11} - r_E}{\chi_{\text{tra}}}, \quad (6.24)$$

$$\eta_{d_2} = \frac{t_E}{2\chi_m A k_0}. \quad (6.25)$$

The power and cross spectrum of the vacuum field is written as

$$S_{a_i a_j} = \delta_{ij} = \begin{cases} 1 & (i = j) \\ 0 & (i \neq j) \end{cases}. \quad (6.26)$$

Therefore, the power spectra of the force noise as for amplitude measurements are calculated as

$$S_{F,b_1}^{\text{ref}} = |\xi_{b_1}|^2 = \frac{(\kappa^2 + \Delta^2) \{ \Delta\iota - [(\kappa - 2\kappa_{\text{in}})^2 + \Delta^2] \omega^2 \}^2}{16\iota\kappa_{\text{in}}(\kappa - \kappa_{\text{in}})^2 \Delta^2 \omega^2} S_F^{\text{SQL}}, \quad (6.27)$$

$$S_{F,b_2}^{\text{ref}} = |\xi_{b_2}|^2 = \frac{\kappa_{\text{in}} \omega^4}{\iota(\kappa^2 + \Delta^2)} S_F^{\text{SQL}}, \quad (6.28)$$

$$S_{F,d_1}^{\text{ref}} = |\xi_{d_1}|^2 = \frac{[\Delta\iota - (\kappa^2 + \Delta^2 - 2\kappa\kappa_{\text{out}}) \omega^2]^2}{4\iota\kappa_{\text{out}}\Delta^2 \omega^2} S_F^{\text{SQL}}, \quad (6.29)$$

$$S_{F,d_2}^{\text{ref}} = |\xi_{d_2}|^2 = \frac{\kappa_{\text{out}} \omega^2}{\iota} S_F^{\text{SQL}}, \quad (6.30)$$

and the power spectra of the force noise as for amplitude measurements are calculated as

$$S_{F,b_1}^{\text{tra}} = |\eta_{b_1}|^2 = \frac{\kappa_{\text{in}} (\kappa^2 + \Delta^2) \omega^2}{\iota \Delta^2} S_F^{\text{SQL}}, \quad (6.31)$$

$$S_{F,b_2}^{\text{tra}} = |\eta_{b_2}|^2 = \frac{\kappa_{\text{in}} \omega^4}{\iota(\kappa^2 + \Delta^2)} S_F^{\text{SQL}}, \quad (6.32)$$

$$S_{F,d_1}^{\text{tra}} = |\eta_{d_1}|^2 = \frac{[\Delta\iota - (\kappa^2 + \Delta^2 - 2\kappa\kappa_{\text{out}}) \omega^2]^2}{4\iota\kappa_{\text{out}}\Delta^2 \omega^2} S_F^{\text{SQL}}, \quad (6.33)$$

$$S_{F,d_2}^{\text{tra}} = |\eta_{d_2}|^2 = \frac{\kappa_{\text{out}} \omega^2}{\iota} S_F^{\text{SQL}}. \quad (6.34)$$

The difference between the reflection and the transmission measurement originates from the noise of the input amplitude fluctuation.

The SQL-normalized sensitivity of the amplitude measurements in the reflection and the transmission are the summation of the contributions of \mathbf{b} and \mathbf{d} . That is,

$$S_{\text{tot}}^{\text{ref}} = \varepsilon_1 S_{b_1}^{\text{ref}} + \varepsilon_2 S_{b_2} + S_d, \quad (6.35)$$

$$S_{\text{tot}}^{\text{tra}} = \varepsilon_1 S_{b_1}^{\text{tra}} + \varepsilon_2 S_{b_2} + S_d, \quad (6.36)$$

where ε_1 and ε_2 are the relative shot noise levels for each quadrature, and we define

$$S_{b_1}^{\text{ref}} = S_{F,b_1}^{\text{ref}} / S_F^{\text{SQL}}, \quad S_{b_1}^{\text{tra}} = S_{F,b_1}^{\text{tra}} / S_F^{\text{SQL}}, \quad (6.37)$$

$$S_{b_2} = S_{F,b_2}^{\text{ref}} / S_F^{\text{SQL}} = S_{F,b_2}^{\text{tra}} / S_F^{\text{SQL}}, \quad (6.38)$$

$$S_d = S_{F,d_1}^{\text{ref}} / S_F^{\text{SQL}} + S_{F,d_2}^{\text{ref}} / S_F^{\text{SQL}} = S_{F,d_1}^{\text{tra}} / S_F^{\text{SQL}} + S_{F,d_2}^{\text{tra}} / S_F^{\text{SQL}}. \quad (6.39)$$

The calculated spectra according to Eqs. (6.35)-(6.39) are displayed in Fig. 6.3. For this plot,

6. Proof-of-principle demonstration of quantum noise cancellation

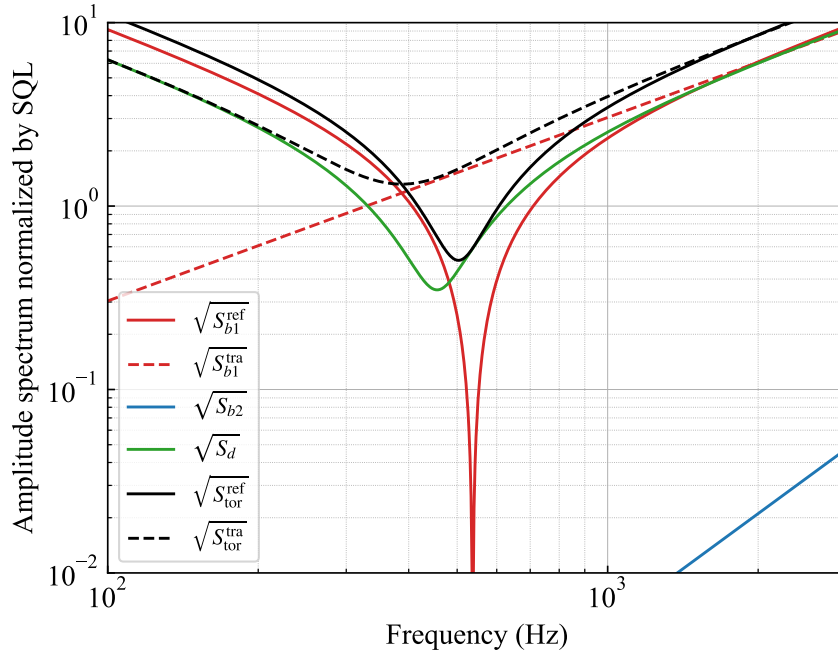


Figure 6.3.: Amplitude spectra of the amplitude and the phase fluctuations. The contribution by the input amplitude fluctuation to the reflection is plotted as a red line. The contribution by the input phase fluctuation and by the vacuum fluctuation from the output port to the reflection is shown in blue and green lines, respectively. The total sensitivity of the amplitude measurement of the reflection is plotted as a black solid line. The input amplitude and the total amplitude of the transmission are shown by red and black dotted lines, respectively.

the vacuum fluctuation is assumed ($\varepsilon_1 = \varepsilon_2 = 1$), and we use parameters of $\lambda = 1064$ nm, $L = 100$ mm, $m = 10$ mg, $\kappa/(2\pi) = 0.25$ MHz, $\kappa_{\text{in}}/\kappa = 0.8$, $\Delta = \kappa/\sqrt{3}$, and $P = 1$ W. The sensitivity of the reflection is improved beyond unity in a particular frequency band. The improvement in the sensitivity is caused by the cancellation of the amplitude fluctuation between the direct reflection and the cavity leakage. The dip frequency of the sensitivity is

$$\omega_{\text{dip}} = \sqrt{\frac{\Delta\omega}{(\kappa - 2\kappa_{\text{in}})^2 + \Delta^2}}. \quad (6.40)$$

Thus, the dip frequency is always higher than the resonant frequency of the optical spring. It is a unique feature of this quantum noise cancellation.

6.3. Proof-of-principle experiment

We have proposed the quantum noise cancellation by measuring the reflected light from a cavity. Furthermore, here we demonstrate it for the first time with our experimental setup.

6.3.1. Method

We can demonstrate the coherent cancellation analyzed in the previous section, while quantum radiation pressure fluctuation does not dominate the other classical noises in our system. As an imitation of the quantum noise, we injected a white noise to the input laser intensity through the acousto-optic modulator as shown in Fig. 6.4. The white noise is enough large so that the classical radiation pressure fluctuation drive the milligram-scale test mass dominantly. This fact is confirmed by coherence measurements between the error signal and the intensity noise. The intensity noise is evaluated by picking off a part of the laser beam just before the cavity. The injected white noise is of the order of $\sqrt{\varepsilon_1} \sim \mathcal{O}(10^3)$; the coherence is almost unity in the measurement frequency region.

As we have seen in the previous section, by detuning the cavity, the optical spring effect emerges, and the dip-shaped noise cancellation is supposed to be observed. Therefore, the main cavity is feedback controlled at a blue-detuned point for this demonstration. To get the error signal for the feedback control, we measure the reflected light amplitude with a photo detector. The error signal is the subtraction between the signal from the photo detector and the point we want to detune at. The error signal is filtered to get the feedback signal. The feedback signal is sent to the coil-magnet actuators on the input mirror. The coil-magnet actuators apply a force in the direction of the cavity axis to control the cavity length at the target detuning point. In addition to the cavity length control, we stabilize the laser frequency to highlight

6. Proof-of-principle demonstration of quantum noise cancellation

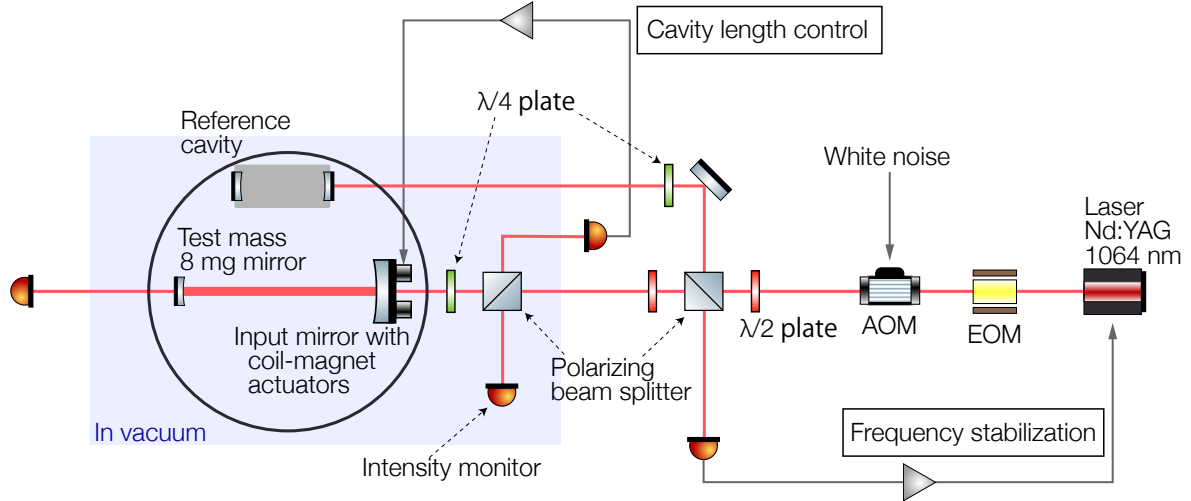


Figure 6.4.: Experimental setup for the demonstration of quantum noise cancellation.

the classical radiation pressure fluctuation. The laser frequency stabilization system described in Section 4.4.1 is operational for all the measurements. During the measurements, the air pressure is kept about 100 Pa to suppress acoustic noises. On the other hand, the air pressure is relatively high to introduce the residual gas damping to lock the main cavity at a detuned point smoothly.

6.3.2. Result

We performed measurements with four different detuning points. For each measurement, we estimate the detuning by monitoring the transmitted light. The proportion of the transmitted light power to that of on resonance indicates the detuning. As the transmitted light power of the resonance, we adopt the maximum output during the cavity scan. The uncertainties of the detuning come from the residual fluctuations of the transmitted light power.

While the measurements, the input laser power is kept constant as $P_{\text{in}} \simeq 4.7$ mW. The finesse of the cavity is measured just before the measurement, which is $\mathcal{F} = (3.0 \pm 0.3) \times 10^3$. The resulting intracavity power is $P \sim 5$ W.

The measured amplitude spectra and corresponding the open-loop transfer functions are shown in Fig. 6.5. The dip-shaped enhancement of the sensitivity is clearly observed. For each detuning point, we also measure the coherence between the intensity noise and the error signal. Let us show the measured coherence with $\delta \sim 0.90$ in Fig. 6.6 as an example. For each detuning, dips are observed in accordance with the dips in the amplitude spectra. It indi-

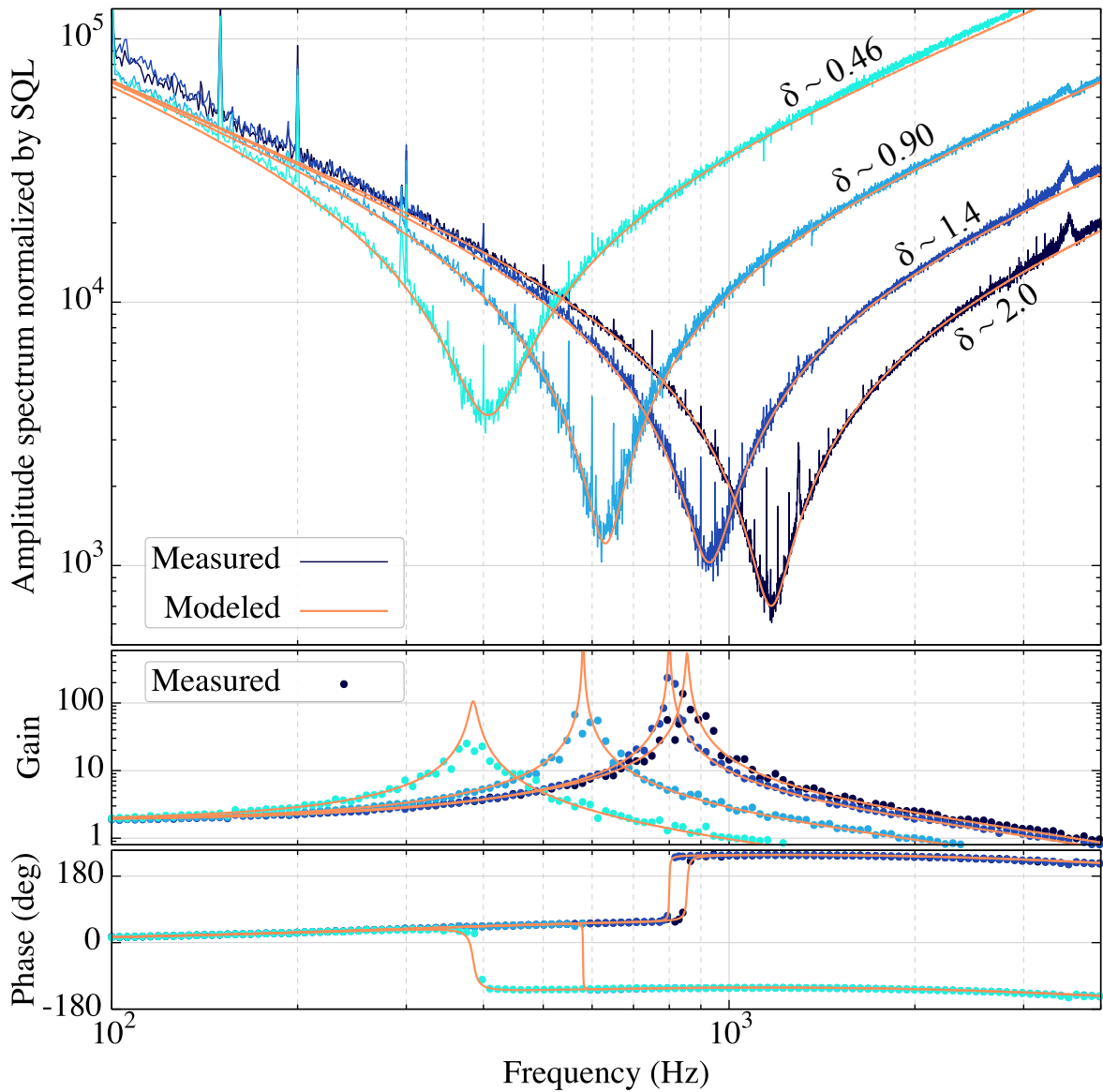


Figure 6.5.: Demonstration of the dip-shaped spectra. At the upper panel, the amplitude spectra are shown with the modeled fitting. They are normalized by the standard quantum limit. The open-loop transfer functions are shown in the middle and bottom panels. The measured values are plotted by blue lines and points. The modeled curves are plotted by orange lines. The four measurements are conducted with different detuning points. The estimated normalized detunings $\delta = \Delta/\kappa$ for each measurement are annotated besides the plotted lines.

6. Proof-of-principle demonstration of quantum noise cancellation

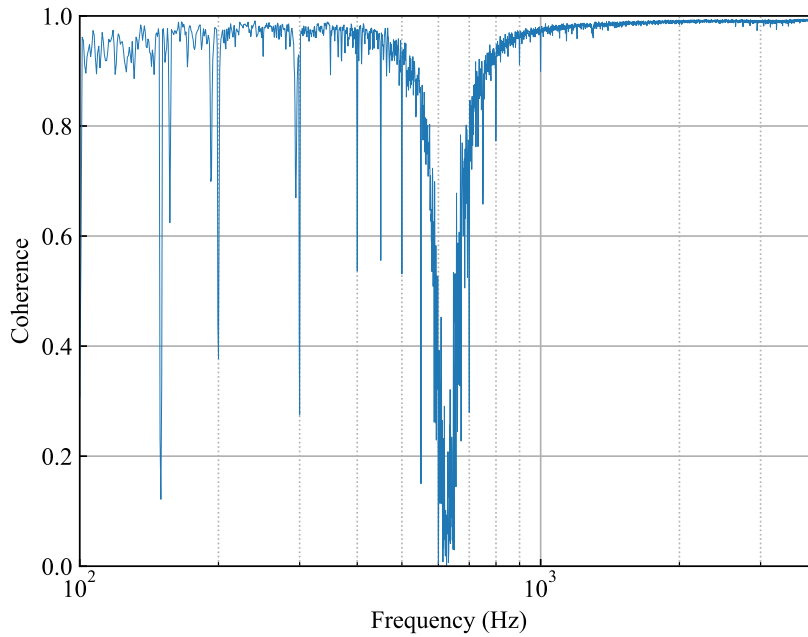


Figure 6.6.: Coherence between the injected intensity noise and the error signal.

cates that the injected intensity noise is dominating the noises as intended, and that around dip frequencies, the coherence decreases because the intensity noise is cancelled.

6.3.3. Discussion

To confirm that the observed dips in the spectra are due to the noise cancellation depicted in Section 6.2, we evaluated the frequency ratio between the dip frequency and the optical spring. The non-unity value of the frequency ratio is a feature of the noise cancellation with the reflection measurement. Moreover, the frequency ratio is a good indicator for characterization of the system because it is free from uncertainties of the intracavity power.

The frequency ratios are plotted against the normalized detunings in Fig. 6.7. To evaluate the uncertainties in the frequency ratios, let us discuss the uncertainty of the dip frequency.

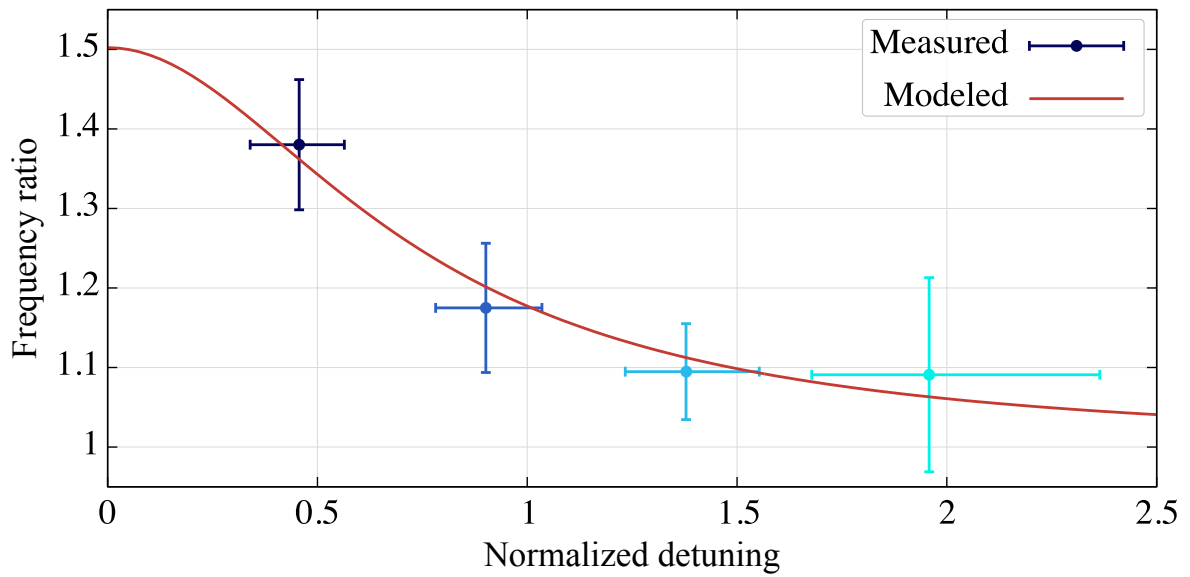


Figure 6.7.: Ratios between the optical spring frequencies and the dip frequencies. For each of measurement, the frequency ratios are calculated. They are plotted with blue points, whose colors correspond to the same colored spectra in Fig. 6.5. The red line shows the modeled curve fitted to the measured data.

Fluctuation in the dip frequency of the sensitivity

Here we discuss the uncertainty of the dip frequency in the measured spectra. The sensitivity with the injection of the dominating white intensity noise is described as

$$\sqrt{S_{b_1}^{\text{ref}}(\omega_{\text{dip,m}})} \propto \frac{|\omega_{\text{dip,m}}^2 - \omega^2|}{\omega_{\text{dip,m}}^2}, \quad (6.41)$$

when the detuning point is fixed ideally. $\omega_{\text{dip,m}}$ is the measured dip frequency. In practice, the detuning point fluctuates. As the result, the sensitivity dip gets thicker. We assume that the fluctuation of the dip frequency follows an Gaussian distribution. Let us define the central frequency to be $\omega_{\text{dip,m}}$ and the standard deviation to be $\delta\omega$. The modeled curve of the dip is described as

$$\sqrt{\left[S_{b_1}^{\text{ref}}(\omega_{\text{dip,m}} + \delta\omega) + S_{b_1}^{\text{ref}}(\omega_{\text{dip,m}} - \delta\omega) \right]} / 2, \quad (6.42)$$

which is the averaged spectrum of the two distributed spectra due to Gaussianity. We estimate the dip frequency with the uncertainty by fitting with the above model. The fitting parameters are $\omega_{\text{dip,m}}$, $\delta\omega$, and the overall factor. The dominant contribution to the uncertainty of the frequency ratio comes from the uncertainty in the dip frequency.

To construct the practical fitting model for the frequency ratio, we need to discuss the effect the mode mismatch between the cavity TEM00 mode and the input beam.

Effect of the mode mismatch

In this section, we discuss the effect of the mode mismatch. In actual experiment, the axis of the input laser beam is not perfectly identical to the axis of the cavity. In our experiment, the mode matching ratio is $\eta = 92\%$. The mismatched light cannot enter into the cavity and directly reflected on the input mirror. Thus, the mismatched light contributes as the sensing noise whose spectrum has a dip at the resonant frequency of the optical spring. Hereafter, let us consider the dip frequency of the sensitivity in case the effect of mode mismatch is included. We describe the power of the TEM00 mode for the cavity as $P_{00} = \eta P_{\text{in}}$. The mismatched light power is $P_{\text{mm}} = (1 - \eta)P_{\text{in}}$. The amplitude fluctuation of the reflection for the TEM00 mode is

$$\chi_{\text{ref}} \xi_{b_1} b'_1 = \sqrt{\frac{\kappa^2 + \Delta^2}{(\kappa - 2\kappa_{\text{in}})^2 + \Delta^2}} \frac{\Delta\omega - [(\kappa - 2\kappa_{\text{in}})^2 + \Delta^2] \omega^2}{\mathcal{M}} b'_1, \quad (6.43)$$

where b'_1 is the classical amplitude noise. The absolute value of it is in proportion to $\sqrt{P_{00}}$. The reflected field of the TEM00 mode is described by the input field $|E_{00}|$ ($\propto \sqrt{P_{00}}$) as

$$|E_{\text{ref},00}| = \sqrt{\frac{(\kappa - 2\kappa_{\text{in}})^2 + \Delta^2}{\kappa^2 + \Delta^2}} |E_{00}|. \quad (6.44)$$

The fluctuation in the power of the reflected TEM00 mode is approximately calculated as

$$\delta P_{\text{ref},00} \propto |E_{\text{ref},00} \chi_{\text{ref}} \xi_{b_1}| b'_1 \quad (6.45)$$

$$\propto \frac{\Delta\iota - [(\kappa - 2\kappa_{\text{in}})^2 + \Delta^2] \omega^2}{\Delta\iota - (\kappa^2 + \Delta^2) \omega^2} \eta P_{\text{in}}. \quad (6.46)$$

Whereas, the fluctuation in the power of the mismatched light is not affected by the cavity since the reflected light does not enter into the cavity;

$$\delta P_{\text{mm}} \propto (1 - \eta) P_{\text{in}}. \quad (6.47)$$

Therefore, the total fluctuation in the reflection light power is $\delta P_{\text{ref}} = \delta P_{\text{ref},00} + \delta P_{\text{mm}}$, and the dip frequency in the spectrum of δP_{ref} is calculated as

$$\omega_{\text{dip,m}} = \sqrt{\frac{\Delta\iota}{\kappa^2 + \Delta^2 - 4\kappa_{\text{in}}(\kappa - \kappa_{\text{in}})\eta}}. \quad (6.48)$$

Mode mismatches give a smaller dip frequency than the perfect mode matching.

The fitted curve based on the above model is also plotted in Fig. 6.7. The fitting parameters are mode matching ratio η and $\kappa_{\text{in}}/\kappa$. We confirm that the measured frequencies of the dips and the optical springs are consistent to our theoretical model. By the fitting, $\eta = 92\%$ and $\kappa_{\text{in}}/\kappa = 0.81$ are estimated.

6.4. Summary of this chapter

An optomechanical cavity is suitable for precise force measurements. Its sensitivity is fundamentally limited by the quantum noises. In this chapter, firstly, we theoretically show that the force sensitivity of the test mass mirror that is trapped by the optical spring can be improved as the dip by measuring the amplitude of the light reflected from the over coupled detuned cavity.

We use our experimental setup to demonstrate this quantum noise reduction technique. The dip-shaped improvement in the sensitivity is observed with the injected laser intensity modulation though the sensitivity is not limited by quantum noises. It is concluded that the amplitude measurement of the reflection from an optomechanical cavity is a simple way to improve its sensitivity even beyond the quantum limit.

7. Prospects for observing quantum radiation pressure fluctuation: the torsional pendulum

In Chapter 5, we have validated the stable configuration of a suspended linear cavity. In Chapter 6, we have demonstrated a quantum noise reduction technique with classical intensity noise. For macroscopic quantum experiments, the sensitivity of the system should reach the quantum radiation pressure noise. For example, the quantum noise reduction technique will be directly proved with quantum noise when the sensitivity is limited by the quantum noise. However, quantum radiation pressure fluctuation have not yet been observed over nanogram-scale optomechanical systems. In this chapter, for observing quantum radiation pressure fluctuation, we propose upgrading the simple pendulum to a torsional pendulum in our experimental setup.

7.1. Sensitivity with the simple pendulum

We evaluate the current sensitivity of our optomechanical system. The estimation reveals the limitation of the setup. In this section, let us discuss the evaluation of the setup to find ways to improve the optomechanical system.

7.1.1. Current sensitivity with the simple pendulum

The displacement spectrum of the simple pendulum is shown in Fig. 7.1. There is no noise peak that was observed in the previous work of milligram-scale optomechanics done by [86]. *Komori (2019)* [86] analyzed that since they used a triangular cavity to avoid the Sidles-Sigg instability, the thermal noise originating from the fixed mirror in the triangular cavity became its peaks. Therefore, it is inferred that the sensitivity is improved thanks to using a linear cavity in the frequency range of 300 Hz to 3 kHz.

The calibration of the measured signal to the displacement of the test mass mirror is shown in Section 7.1.3. In Fig. 7.1, the estimation of quantum radiation pressure noise and possible

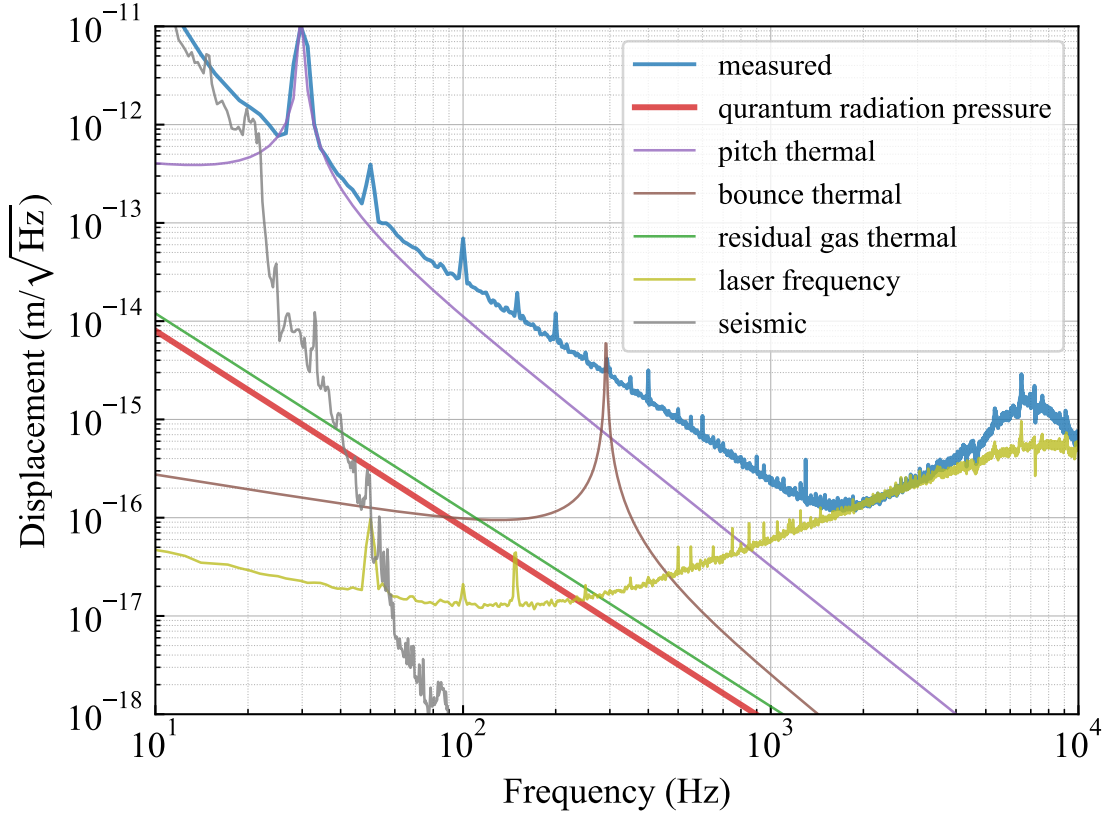


Figure 7.1.: Displacement spectrum of the simple pendulum. In addition, the estimated quantum radiation pressure noise is described. The estimated noises are also plotted.

noise sources that limit the current sensitivity are also plotted. For quantum radiation pressure fluctuation, we discuss the estimation in the next section. The evaluations of noise sources are described in Section 7.1.4.

7.1.2. Estimation of the quantum radiation pressure fluctuation

In this section, the detailed method to estimate the quantum radiation pressure fluctuation is introduced. The theoretical description of the force spectrum of quantum radiation pressure fluctuation can be rewritten with the cavity parameters by

$$S_{f, \text{qrp}} = \frac{32\hbar\omega_0\mathcal{F}^2 P_{\text{in}} \kappa_{\text{in}}}{\pi^2 c^2} \frac{1}{\kappa (1 + \delta^2)^2}, \quad (7.1)$$

where ω_0 is the laser angular frequency, \mathcal{F} is the finesse, P_{in} is the input power, κ is the total cavity decay rate of photons, κ_{in} is the decay rate of photons from the input mirror, and $\delta = \Delta/\kappa$ is the normalized detuning. In general, laser power measurements tend to have a large systematic error of about 5 %. This is because of the large errors in the responsibility of the photo detector and the estimation of $\kappa_{\text{in}}/\kappa$. Furthermore, the input power is effectively reduced when the mode matching is not perfect. Mode matching ratio on the cavity resonance also has the systematic error because the alignment is slightly changed due to the constant radiation pressure when the cavity accumulates the laser power.

To avoid these systematic errors, we use a method to estimate quantum radiation pressure fluctuation by focusing on the optical spring frequency. The optical spring constant is given by

$$K_{\text{opt}} = \frac{16\omega_0 \mathcal{F}^2 P_{\text{in}} \kappa_{\text{in}}}{\pi^2 c^2 \kappa} \frac{\delta}{(1 + \delta^2)^2}. \quad (7.2)$$

Thus, by using the optical spring frequency $\omega_{\text{opt}}/2\pi = K_{\text{opt}}/m$, the force spectrum of quantum radiation pressure fluctuation is simplified as

$$S_{f, \text{qrp}} = \frac{2\hbar}{\delta} m \omega_{\text{opt}}^2, \quad (7.3)$$

where m is the mass of the oscillator. The optical spring frequency can be estimated with small systematic errors by measuring the open-loop transfer function of the cavity length control. Therefore, we use Eq. (7.3) to estimate the quantum radiation pressure fluctuation in our experiment.

7.1.3. Calibration

The optomechanical system is feedback controlled to keep the resonance of the cavity. The error signal is the signal we observe, and it includes information of the displacement of the test mass mirror. In this section, we describe the calibration method from the signal to the test mass mirror's displacement.

The block diagram is useful to represent feedback controlled systems. In a block diagram, each transfer function is represented as a block, and interactions between them are represented by arrows. The basics of block diagram is introduced in Appendix A.

As for the cavity length, there are two feedback loops. One is the feedback loop of the optical spring, and the other is the active-feedback loop that we introduce to control the cavity length. We define the transfer functions as follows: H_{pend} is for the test mass mirror, H_{opt} is for the optical spring, H_{cav} is for the cavity, H_{PD} is for the photo detector, H_{filter} is for the filter, H_{act} is for the actuator attached on the controlled input mirror, and H_{con} is for the controlled input mirror.

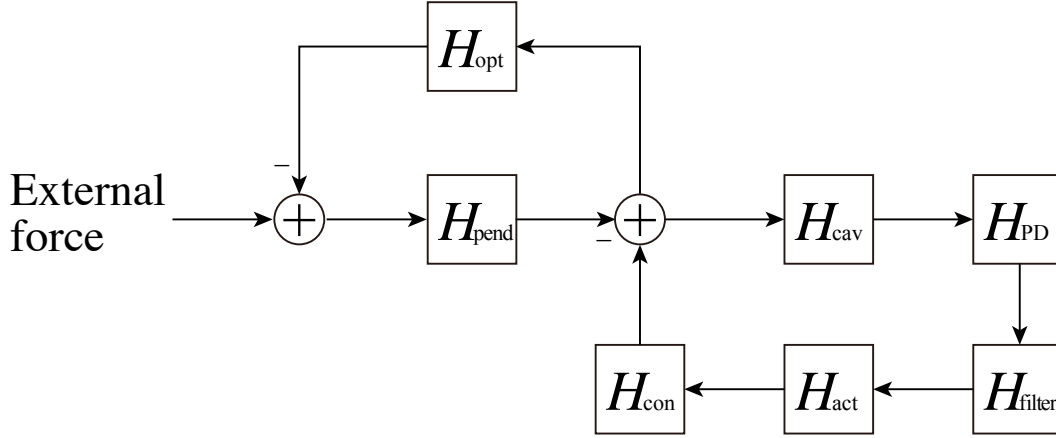


Figure 7.2.: Block diagram of the optomechanical system with the feedback controlling.

For the cavity length, two loops should be considered. The optical spring works as a feedback control as well as the active feedback control.

Our optomechanical system is represented by the block diagram shown in Fig. 7.2. The two open-loop transfer functions are defined as $G_1 = H_{\text{pend}}H_{\text{opt}}$ and $G_2 = H_{\text{cav}}H_{\text{PD}}H_{\text{filter}}H_{\text{act}}H_{\text{con}}$, respectively.

We calibrate the error signal in the unit of voltage to the displacement of the test mass mirror. By the calculation based on the block diagram, the displacement of the cavity mirror x_{dis} is expressed by

$$x_{\text{dis}} = \left| \frac{1 + G_0}{G_0} H_{\text{filter}} H_{\text{act}} H_{\text{con}} \right| V_{\text{error}}, \quad (7.4)$$

where we define $G_0 = G_2/(1 + G_1)$. The transfer function of the filter is measured independently, and the actuator efficiency is measured in advance with the Michelson interferometer as mentioned in Section 4.2.2. The transfer function (susceptibility) of the controlled input mirror is determined by the mass. To measure the open-loop transfer functions, we inject sine waves of various frequencies into the cavity length control loop after the filter. By taking the ratio of the signals before and after the injected point, the open-loop transfer function G_0 can be measured. Therefore, the calibration of Eq. (7.4) is completed.

We note that the optical spring frequency is also determined by the open-loop transfer function measurement. The resonance observed in the open-loop transfer function corresponds to the optical spring frequency since it is in proportion to

$$G_0 \propto \frac{1}{\omega_{\text{opt}}^2 - \omega^2}, \quad (7.5)$$

where the cavity mirrors are in the free-mass regime.

7.1.4. Noise analysis

As we have seen in Fig. 7.1, quantum radiation pressure fluctuation is covered with other classical noises. We evaluate possible noises in the followings.

Thermal noises of the test mass mirror

From the frequency of the peak, we conjecture that the thermal noise of the pitch mode and bounce mode in the test mass mirror contributes. The material properties indicate that the bounce mode and the pitch mode should be at 300 Hz and 30 Hz, respectively. In particular, the thermal noise of the pitch mode is dominant in the low frequency region.

Residual gas thermal noise

The residual gas thermal noise is calculated with the measured pressure of 9.8×10^{-5} Pa. As Fig. 7.1 shows, the residual gas thermal noise is slightly above the quantum radiation pressure noise. The pressure satisfies the requirement for the design sensitivity. By increasing the input laser power, the quantum radiation pressure can be enhanced to stand out.

Laser frequency noise

The measured frequency noise is above the design value by a factor of 10 in 100 Hz band. This is because the open-loop gain of the feedback control is not enough at the high frequency range. An open-loop gain of 100 is expected for the design sensitivity. However, the oscillation of the feedback control loop limits the gain.

Seismic noise

We assume the vibration isolation by the factor of $1/f^4$ since the system is on the double suspension. The seismic noise in the experimental space is measured with a geophone, and estimate the contribution to the test mass mirror. The result infers that the seismic noise is not limit the current sensitivity.

Not identified noise

In 100 Hz range, there is a noise that has a dependency of $1/f^2$. Because of the dependency, it has the possibility of thermal noise in viscous-damping model. If the pitch thermal noise follows the viscous-damping model, the observed noise level can be explained. As a candidate, the thermal noise in the pitch mode that originates from the adhesive at the wire-to-mirror

connection can follow the viscous-damping model. However, it is not able to identify the noise source so far.

7.2. Upgrading with the torsional pendulum

The noise analytics gives us a possible solution for the better sensitivity, which is a torsional pendulum. In this section, we discuss the possibility of upgrading our optomechanical system with a torsional pendulum.

7.2.1. Idea of using a torsional pendulum

The pioneering work of an optomechanical torsional pendulum was done by *Komori et al.* in 2019 [73]. They used a thin fused silica plate as the test mass, and the silica plate was suspended as a torsional pendulum. By constructing triangular cavities on both edges of the pendulum, they realized an optomechanical torsional pendulum. We perceive that the combination of the idea and our linear cavity can build a more sensitive system. In the following section, firstly, we introduce the advantages of a torsional pendulum as an optomechanical oscillator.

7.2.2. Advantages of an optomechanical torsional pendulum

The key advantages of a torsional pendulum as an optomechanical oscillator is its low noises. The thermal noise is low because of its low resonant frequency, and some classical common noises are suppressed due to the common mode rejection.

Low thermal noise

The thermal noise of the pendulum is in proportion to $\sqrt{\omega_m \phi}$, where ω_m is the resonant frequency of the pendulum and ϕ ($1/Q$) is the loss angle. In general, although a torsional pendulum has larger loss angle than a simple pendulum, the resonant frequency of the torsional pendulum can be lower than that of the simple pendulum. The resonant frequency of a typical simple pendulum is a few Hz, and its Q value is on the order of 10^5 at best. On the other hand, although the Q value of an torsional pendulum is on the order of 10^3 , the resonant frequency can be below 0.1 Hz. Therefore, the resulting thermal noise can be lower in the torsional pendulum than the simple pendulum because the resonant frequency has the second order dependency. The low thermal noise is a characteristic advantage of a torsional pendulum.

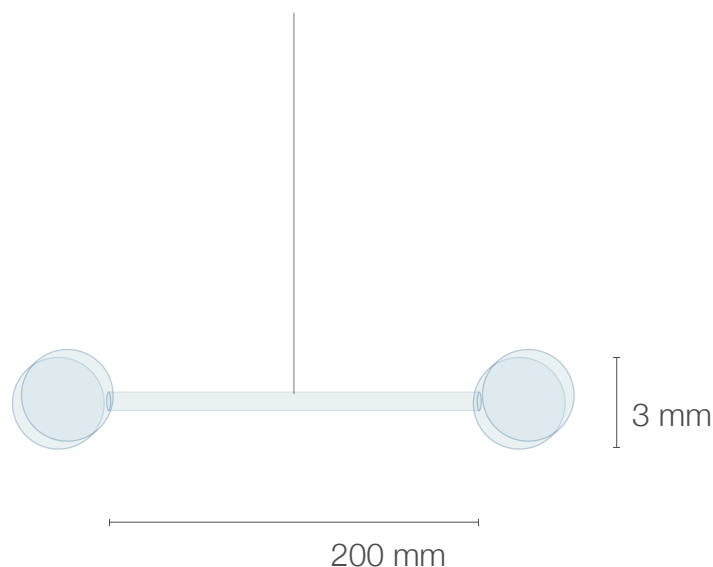


Figure 7.3.: Schematic drawing of the torsional pendulum. The both edges have the 8-mg mirrors to construct the linear cavities. The two mirrors are connected to each other by a glass pipe, forming the torsional pendulum.

Common mode rejection

For an optomechanical torsional pendulum, the angle is read out by measuring the displacement of both the arm. Since the differential signal of the two cavities is measured to sense the rotational motion of the torsional pendulum, noises that contribute equally to both cavities are cancelled. This common mode rejection is an advantage of an optomechanical torsional pendulum. For example, the frequency noise and the pitch thermal noise will be common mode noises by using a common laser source for the cavities.

7.2.3. Design sensitivity with the torsional pendulum

The torsional pendulum is designed to be compatible with the linear cavity composed of the simple pendulum as shown in Fig. 7.3. For a torsional pendulum, we measure the rotational motion of it. The linear cavities on the edges of the torsional pendulum sense the rotation of the pendulum by subtracting the signals of the cavities. The design sensitivity with the torsional pendulum is shown in Fig. 7.4. The parameters for the design are listed in Table 7.1. Quantum radiation pressure fluctuation can be observed wider range of the frequencies with better signal to noise ratio than the simple pendulum. We have notes for the following two types of noise.

7. Prospects for observing quantum radiation pressure fluctuation: the torsional pendulum

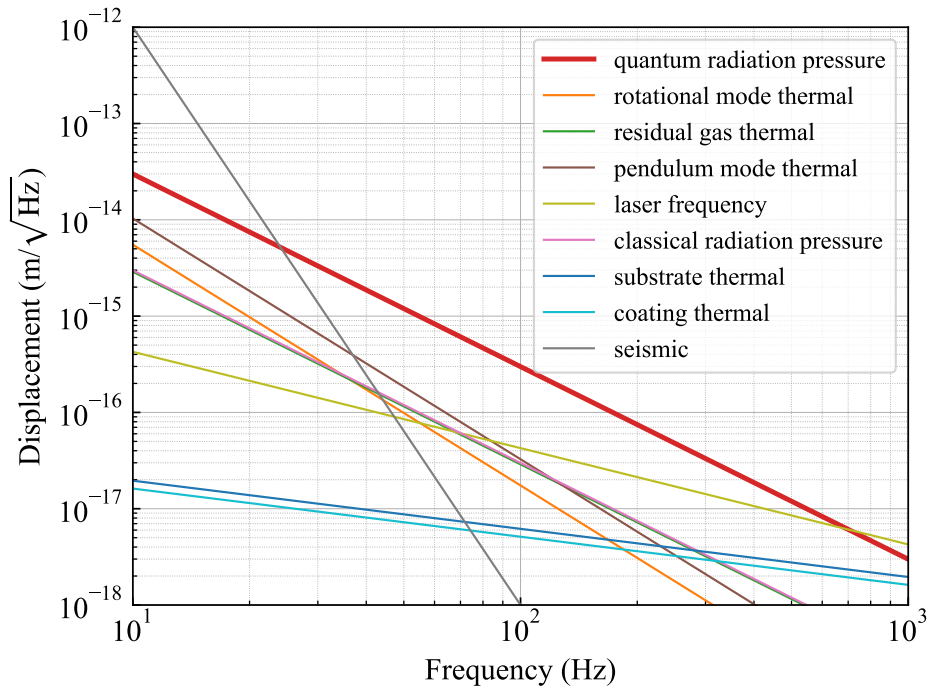


Figure 7.4.: Design sensitivity with the torsional pendulum.

Noises that contribute to both cavities independently

When a noise contributes to both cavities independently, the resulting sensitivity will be improved by the factor of $1/\sqrt{2}$ due to the subtraction of the signals from the two cavities. The noises are, for example, the mirror substrate thermal noise, mirror coating thermal noise.

Noises that is suppressed by the common mode rejection

Noises that contribute to both cavities identically are cancelled by the subtraction. In reality, it is not exactly identical, thus the noises are reduced by a certain factor. The reducing factor due to the common mode rejection is called common mode rejection ratio. The typical value of the common mode rejection ratio is 10 to 100. Here, we assume the common mode rejection ratio γ_{CMRR} is 10. Therefore, we can relax our requirement of the frequency noise by the factor of 10. As the result, our current reference cavity can be for the upgrading. The pitch mode thermal noise will be the common mode noise. Furthermore, the suspension point of the torsional pendulum is lower than the simple pendulum. Thus, we assume that the pitch thermal noise can be reduced by the factor of 10.

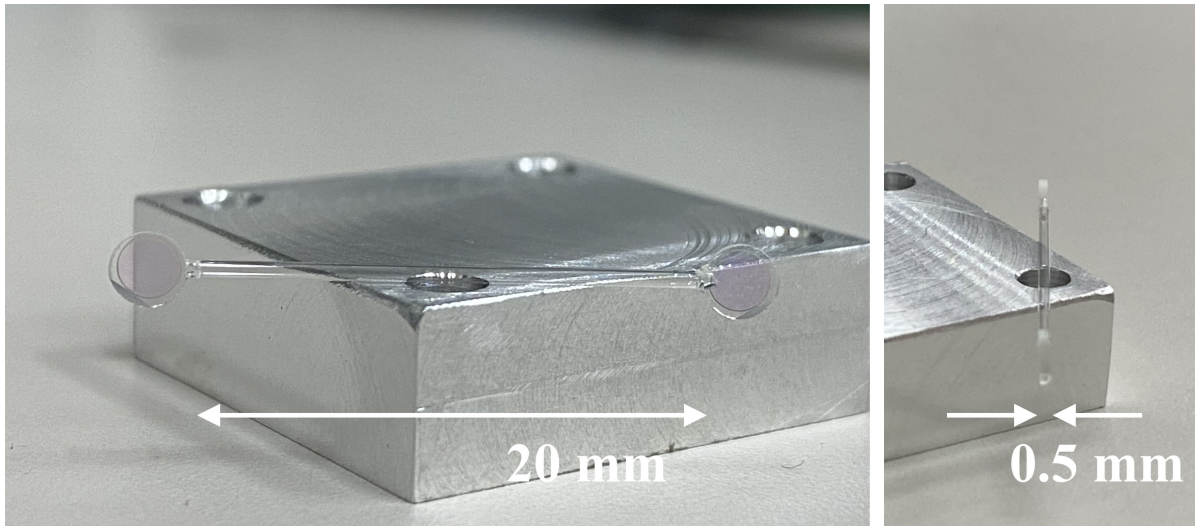


Figure 7.5.: Pictures of the torsional pendulum.

7.3. Towards experimental realization

We have seen the promise of the optomechanical torsional pendulum with linear cavities. The decisive difference from the current setup is the torsional pendulum itself. Therefore, the development of the torsional pendulum is of paramount.

7.3.1. Development of the torsional pendulum

As the final part of the dissertation, we introduce the development of the torsional pendulum. To make the torsional pendulum as designed, we use two 8-mg mirrors that is identical to the simple pendulum. For the glass pipe to connect the two mirrors, a 20 mm long glass pipe made by Nakahara Opto-Electronics Laboratories Inc. is selected. The outer diameter is 0.7 mm, and the inner diameter is 0.6 mm. The thickness is chosen to be the thinnest to reduce the mass of the torsional pendulum, while allowing it to be handled without breaking.

The epoxy resin is used for connecting the 8-mg mirrors and the glass pipe. The epoxy resin is grouped in chemical reaction harden type. In making the optomechanical pendulum, we have to be careful with the frosting with the resin due the volatilization of solvents. The epoxy is an adhesive that cures without frosting because the hardening process is chemical reactions without volatilization. The epoxy resin is advantageous also because of its small volume change and its strength. The pictures of the torsional pendulum that is successfully made with the 8-mg mirrors and the glass pipe are shown in Fig. 7.5.

7.4. Summary of this chapter

We evaluate the current sensitivity with our setup and examine the noise sources. The results infer that the issues will be able to be solved by upgrading the pendulum to the torsional pendulum. We redesign our system with the newly designed torsional pendulum and show the sensitivity. Furthermore, we develop the torsional pendulum. The development is a crucial step towards observing quantum radiation pressure with a milligram-scale optomechanical system.

Table 7.1.: Parameters for the design sensitivity towards observation of the quantum radiation pressure fluctuation with the torsional pendulum.

Test mass mirror		
mass		8 mg
diameter		3 mm
radius of curvature		100 mm
reflectivity		99.99%
Rotational Q value		2×10^3
Pendulum Q value		10^5
beam radius		0.21 mm
Young's modulus	substrate	73 GPa
	SiO ₂	73 GPa
	TiO ₂ :Ta ₂ O ₅	140 GPa
Poisson ratio	substrate	0.17
	SiO ₂	0.17
	TiO ₂ :Ta ₂ O ₅	0.28
loss angle	substrate	1×10^{-5}
	SiO ₂	1×10^{-4}
	TiO ₂ :Ta ₂ O ₅	4×10^{-4}
refractive index	substrate	1.45
	SiO ₂	1.45
	TiO ₂ :Ta ₂ O ₅	2.07
Torsional bar length		20 mm
Input mirror		
mass		60 g
radius of curvature		100 mm
reflectivity		99.9%
Cavity		
cavity length		110 mm
finesse		5000
intracavity power		14 W
Common mode rejection ratio		10
Laser		
wavelength		1064 nm
input power		10 mW
frequency noise		$100 \text{ Hz}/f \text{ Hz}/\sqrt{\text{Hz}}$
temperature		300 K
air pressure		10^{-4} Pa

8. Conclusion

8.1. Summary

Milligram-scale optomechanical systems offer an unique way to elucidate macroscopic quantum phenomena, which have been never observed. It is not clear that quantum mechanics is valid for all the mass scale and how to incorporate the gravitational effect. While theoretical approaches have been made for a long time, recent progress in experimental techniques gives a fare opportunity of realizing macroscopic quantum systems to test them. Milligram-scale optomechanical systems are the representative candidates for the realization of macroscopic quantum systems. The mass of the oscillator is much heavier than the system where quantum phenomena have been observed. At the same time, milligram-scale optomechanical systems have a potential to reach quantum regime. Here, we adopt quantum radiation pressure fluctuation as a criteria of reaching the quantum regime.

On the other hand, milligram-scale optomechanical systems are suitable for the platform to test advanced technologies in gravitational wave detectors. The sensitivity of the modern and future gravitational wave detectors are limited by quantum noise. Quantum noise is a fundamental noise, and it can not be reduced by classical manipulations. Therefore, the advanced techniques to reduce quantum noise is central issue. While various theoretical proposals were made, a number of them have yet to be demonstrated experimentally. Modern gravitational wave detectors are in the large scale projects, and validating of the advanced techniques before the actual installation is important. Thus, milligram-scale optomechanical systems can be used as preferable research platform.

For mechanical oscillators, pendulums are often used in milligram-scale optomechanical systems. Pendulums are robust against environmental noises. The sensitivity is further enhanced by coupling a strong optical field to the pendulum. To do this, optical cavities are usually used with a suspended mirror as the pendulum. However, the strong radiation pressure inside a cavity can destabilize the rotational degrees of freedom for cavity mirrors. In particular, either of rotational degrees of freedom is unstable in linear cavities. This instability, called Sidles-Sigg instability, limits the maximum power that the cavity can accumulate. Consequently, it limits the sensitivity of the optomechanical system. Although, more complicated

8. Conclusion

systems such as triangular cavities can avoid Sidles-Sigg instability, they are disadvantageous in that they have to be coupled more to the environmental disturbance. Thus, a stable suspended linear cavity has been desired.

In the dissertation, we identify the stable configuration of a suspended linear cavity. When a linear cavity is built with unbalanced-mass mirrors and in the negative- g regime, the rotational degrees of freedom will not be unstable. This is because the common mode, which is destabilized by radiation pressure in the negative- g regime is mechanically stiff due to the unbalanced masses. Furthermore, the differential mode is even stabilized with the increase in the intracavity power. This effect is named optical torsional spring. We find that with this system, the limitation by Sidles-Sigg instability can be removed, and the sensitivity will be optimum.

We realize a suspended linear cavity with 8 mg test mass mirror with the configuration. The sensitivity is designed to reach quantum radiation pressure fluctuation for macroscopic quantum experiments by utilizing the light mass of the mirror. The mass of 8 mg is the smallest for a suspended mirror with curvature. As the validation of our trapping scheme, the rotational stiffness of the cavity mirrors is evaluated with variable intracavity powers. The results indicate that the optical torsional spring works as the theoretical prediction without inconsistency. Therefore, we conclude that the proposed configuration for a suspended linear cavity is established.

With the optomechanical system, we demonstrate a quantum noise reduction technique. It shows the usefulness of milligram-scale optomechanical systems. We inject classical intensity noise, which imitates quantum noise. The coherent cancellation in the noise is clearly observed, and we characterize the behavior of the dip-shaped reduction to confirm the theoretical model. This is the first demonstration of the technique.

We analyze the noise sources for the current setup to search for upgrading of the system. Replacing the simple pendulum with a torsional pendulum is our upgrade plan, and the advantages and the expected sensitivity are discussed. The advantages for torsional pendulums are its low thermal noise and the common mode rejection. To realize the upgrade, the development of the torsional pendulum is crucial. We report the success of making the pendulum as the last part of the dissertation.

Through the experiments with the suspended linear cavity, we validate the identified configuration and present the benefit of milligram-scale optomechanical systems.

8.2. Future prospects

The final goal of this research is observing quantum radiation pressure fluctuation for macroscopic quantum experiments. Towards the goal, we show the feasibility of the upgrade with

the torsional pendulum. Consequently, the realization of the optomechanical system with the developed torsional pendulum is the future prospect.

The suspension system for the test mass need not to be changed. On the other hand, the suspension system for the controlled input mirror should be revised to inject two input laser beams for both arms. Accordingly, the input optics have to be modified.

The simultaneous locking of the cavities is expected to be technically difficult. However, the previous work [73] succeeded in the simultaneous locking with an optomechanical torsional pendulum of the milligram scale.

Although the technical difficulties remain, the stability of the key role is elucidated in the dissertation. Therefore, it is inferred that the path of the realization is well set.

8.3. Conclusion

This work establishes a class of milligram-scale optomechanical systems, which is a suspended linear cavity. The cavity mirrors are trapped with the optical torsional spring effect. Therefore, the sensitivity can be optimized in a linear cavity, which is suitable to precise measurements.

Thus, this work has expanded the use of linear cavities. At the same time, it has paved the way for realization of macroscopic quantum experiments, and, ultimately, the elucidation of the fundamental problems in physics.

A. Classical feedback-control theory

In this work, we make use of feedback controls. In this chapter, we review the basics of classical feedback-control theory.

A.1. Linear system

A.1.1. Definition

Let us consider a system with an input $x_i(t)$ and an output $y_i(t)$ as follows:

$$x_i(t) \rightarrow y_i(t). \quad (\text{A.1})$$

When this input-output relation is linear, i.e., for any constants a and b ,

$$ax_1(t) + bx_2(t) \rightarrow ay_1(t) + by_2(t), \quad (\text{A.2})$$

then the system is a linear system. For example, a system consisting of operators as constant multiplication, differentiation, and integration on the input is a linear system.

A.1.2. Transfer function

In a linear system with an input $x_i(t)$ and an output $y_i(t)$, by considering the Laplace transform:

$$X(s) = \int_0^t x(t)e^{-st} dt, \quad (\text{A.3})$$

the input-output relationship of this system can be expressed with the following form:

$$Y(s) = H(s)X(s). \quad (\text{A.4})$$

$H(s)$ is called the transfer function of this linear system.

A.1.3. Block diagram

Linear systems are often represented using a diagram called block diagram. In a block diagram, the transfer function is drawn as a block, and the inputs and outputs are represented by lines with arrows, as shown in Fig. A.1.



Figure A.1.: Block diagram of a linear system.

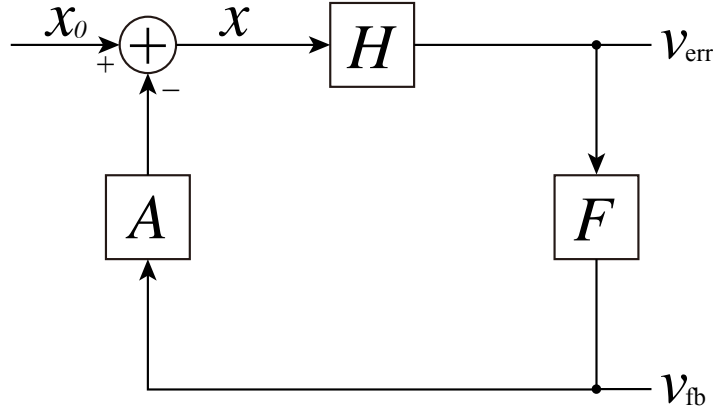


Figure A.2.: Block diagram representing the feedback control system.

A.2. Feedback control

Let us consider feedback control by a linear system. Specifically, we consider the system shown in Fig. A.2, which consists of sensor S , filter F , and actuator A . Although the specific form of each transfer function is not assumed here, in general, the physical quantity x to be controlled is detected by the sensor, and the signal passes through the filter that characterizes the control. The filtered signal is fed back by the actuator. By this feedback control, the original variation x_0 is suppressed to the residual variation x . The signal $v_{\text{err}} = Hx$ is called the error signal. The signal $v_{\text{fb}} = FHx$ returned to the actuator is called the feedback signal.

The block diagram is used to calculate the residual variation x . It shows

$$x = x_0 - AFHx, \quad (\text{A.5})$$

and, therefore, x is expressed by

$$x = \frac{1}{1 + G}x_0, \quad (\text{A.6})$$

where the open-loop transfer function of the feedback loop is defined by $G = AFH$. By making the open-loop gain $|G|$ sufficiently large, the residual variation can be suppressed.

One of the criteria to judge whether a feedback control is stable or not is the Nyquist stability criterion. According to the Nyquist criterion, a feedback control is stable when the phase

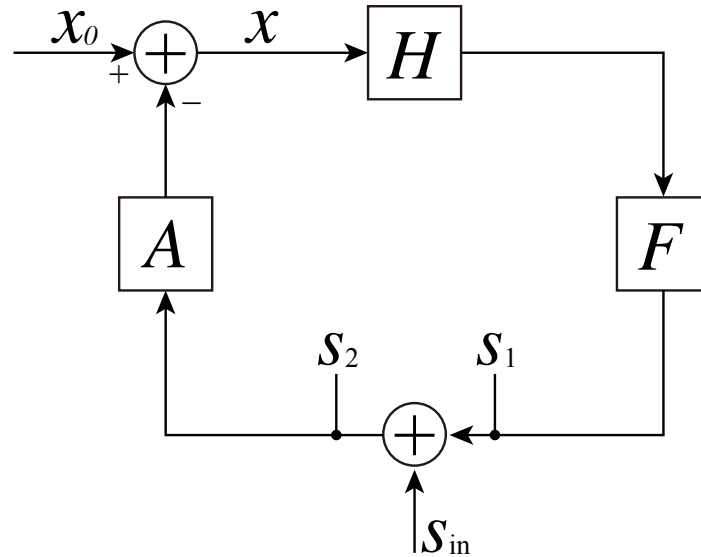


Figure A.3.: Measurement of the open-loop transfer function.

margin is greater than zero [93]. The phase margin is defined by the phase difference of $\arg G$ from -180 degrees at the frequency where the gain of the open loop transfer function becomes unity, i.e., $|G| = 1$. The frequency of the unity gain is often called the unity gain frequency (UGF).

A.3. Measuring the open-loop transfer function

One way to measure the open-loop transfer function is to inject a reference signal into the feedback loop and measure the ratio of the signals before and after the injected point. Let us consider a feedback loop consisting of a sensor S , a filter F , and an actuator A as shown in Fig. A.3. A reference signal s_{in} is injected between the filter and the actuator. Actually, the identical open-loop transfer function can be obtained wherever the reference signal is injected in the loop.

During the injection, the signal in the loop x will be

$$x = x_0 - A(FHx + s_{in}). \quad (\text{A.7})$$

Therefore, the signals before and after the injected point are described by

$$s_1 = \frac{FHx_0 - Gs_{in}}{1 + G}, \quad (\text{A.8})$$

$$s_2 = \frac{FHx_0 + s_{in}}{1 + G}. \quad (\text{A.9})$$

A. Classical feedback-control theory

If the injected signal is large enough as $s_{\text{in}} \ll FHx_0$, the ratio of them will be

$$\frac{s_1}{s_2} = \frac{FHx_0 - Gs_{\text{in}}}{FHx_0 + s_{\text{in}}} \simeq -G. \quad (\text{A.10})$$

It shows that the open-loop transfer function G is measured by taking the ratio of the signals before and after the injected point.

Bibliography

- [1] W. Gerlach and O. Stern, *Der experimentelle nachweis der richtungsquantelung im magnetfeld*, *Zeitschrift für Physik* volume **9** (1922) 349.
- [2] M. Born, *Zur Quantenmechanik der Stoßvorgänge*, *Z. Phys.* **37** (1926) 863–867.
- [3] P. Kusch and H. M. Foley, *The Magnetic Moment of the Electron*, *Phys. Rev.* **74** (1948) 250.
- [4] J. S. Schwinger, *On Quantum electrodynamics and the magnetic moment of the electron*, *Phys. Rev.* **73** (1948) 416–417.
- [5] Y. Fein, P. Geyer, P. Zwick, *et al.*, *Quantum superposition of molecules beyond 25 kDa*, *Nat. Phys.* **15** (2019) 1242–1245.
- [6] G. Jaeger, *What in the (quantum) world is macroscopic?*, *American Journal of Physics* **82** (2014) 896–905.
- [7] M. B. Green and J. H. Schwarz, *Anomaly Cancellation in Supersymmetric D=10 Gauge Theory and Superstring Theory*, *Phys. Lett. B* **149** (1984) 117–122.
- [8] D. J. Gross, J. A. Harvey, E. J. Martinec, and R. Rohm, *The Heterotic String*, *Phys. Rev. Lett.* **54** (1985) 502–505.
- [9] J. H. Schwarz, *Physical States and Pomeron Poles in the Dual Pion Model*, *Nucl. Phys. B* **46** (1972) 61–74.
- [10] P. Candelas, G. T. Horowitz, A. Strominger, and E. Witten, *Vacuum Configurations for Superstrings*, *Nucl. Phys. B* **258** (1985) 46–74.
- [11] M. B. Green and J. H. Schwarz, *Supersymmetrical String Theories*, *Phys. Lett. B* **109** (1982) 444–448.
- [12] W. Nahm, *Supersymmetries and their Representations*, *Nucl. Phys. B* **135** (1978) 149.

Bibliography

- [13] E. Bergshoeff, E. Sezgin, and P. K. Townsend, *Supermembranes and Eleven-Dimensional Supergravity*, *Phys. Lett. B* **189** (1987) 75–78.
- [14] E. Witten, *String theory dynamics in various dimensions*, *Nucl. Phys. B* **443** (1995) 85–126, arXiv:hep-th/9503124.
- [15] A. Sen, *GRAVITY AS A SPIN SYSTEM*, *Phys. Lett. B* **119** (1982) 89–91.
- [16] A. Ashtekar, *New Variables for Classical and Quantum Gravity*, *Phys. Rev. Lett.* **57** (1986) 2244–2247.
- [17] A. Ashtekar, *New Hamiltonian Formulation of General Relativity*, *Phys. Rev. D* **36** (1987) 1587–1602.
- [18] K. G. Wilson, *Confinement of Quarks*, *Phys. Rev. D* **10** (1974) 2445–2459.
- [19] C. Rovelli and L. Smolin, *Knot Theory and Quantum Gravity*, *Phys. Rev. Lett.* **61** (1988) 1155.
- [20] C. Rovelli and L. Smolin, *Loop Space Representation of Quantum General Relativity*, *Nucl. Phys. B* **331** (1990) 80–152.
- [21] C. Rovelli and L. Smolin, *Discreteness of area and volume in quantum gravity*, *Nucl. Phys. B* **442** (1995) 593–622, arXiv:gr-qc/9411005. [Erratum: *Nucl.Phys.B* 456, 753–754 (1995)].
- [22] T. Thiemann, *The Phoenix project: Master constraint program for loop quantum gravity*, *Class. Quant. Grav.* **23** (2006) 2211–2248, arXiv:gr-qc/0305080.
- [23] J. Engle, R. Pereira, and C. Rovelli, *Flipped spinfoam vertex and loop gravity*, *Nucl. Phys. B* **798** (2008) 251–290, arXiv:0708.1236 [gr-qc].
- [24] A. Einstein, *Die grundlage der allgemeinen relativitätstheorie*, *Annalen der Physik* **49** (1916) 769–822.
- [25] A. Bassi, A. Großardt, and H. Ulbricht, *Gravitational Decoherence*, *Class. Quant. Grav.* **34** (2017) 193002, arXiv:1706.05677 [quant-ph].
- [26] L. Diósi, *Gravitation and quantummechanical localization of macroobjects*, *Phys. Lett. A* **105** (1984) 199–202, arXiv:1412.0201 [quant-ph].
- [27] R. Penrose, *On gravity's role in quantum state reduction*, *Gen. Rel. Grav.* **28** (1996) 581–600.

- [28] G. C. Ghirardi, A. Rimini, and T. Weber, *A Unified Dynamics for Micro and MACRO Systems*, *Phys. Rev. D* **34** (1986) 470.
- [29] A. Bassi, K. Lochan, S. Satin, T. P. Singh, and H. Ulbricht, *Models of Wave-function Collapse, Underlying Theories, and Experimental Tests*, *Rev. Mod. Phys.* **85** (2013) 471–527, arXiv:1204.4325 [quant-ph].
- [30] M. R. Andrews, C. G. Townsend, H.-J. Miesner, D. S. Durfee, D. M. Kurn, and W. Ketterle, *Observation of interference between two bose condensates*, *Science* **275** (1997) 637–641.
- [31] M. Aspelmeyer, T. J. Kippenberg, and F. Marquardt, *Cavity Optomechanics*, *Rev. Mod. Phys.* **86** (2014) 1391, arXiv:1303.0733 [cond-mat.mes-hall].
- [32] H. Miao, D. Martynov, H. Yang, and A. Datta, *Quantum correlation of light mediated by gravity*, *Phys. Rev. A* **101** (2020) 063804, arXiv:1901.05827 [quant-ph].
- [33] D. Kafri, J. M. Taylor, and G. J. Milburn, *A classical channel model for gravitational decoherence*, *New J. Phys.* **16** (2014) 065020, arXiv:1401.0946 [quant-ph].
- [34] J. Schmöle, M. Dragosits, H. Hepach, and M. Aspelmeyer, *A micromechanical proof-of-principle experiment for measuring the gravitational force of milligram masses*, *Class. Quant. Grav.* **33** (2016) 125031, arXiv:1602.07539 [physics.ins-det].
- [35] C. Marletto and V. Vedral, *Gravitationally-induced entanglement between two massive particles is sufficient evidence of quantum effects in gravity*, *Phys. Rev. Lett.* **119** (2017) 240402, arXiv:1707.06036 [quant-ph].
- [36] S. Bose, A. Mazumdar, G. W. Morley, H. Ulbricht, M. Toroš, M. Paternostro, A. Geraci, P. Barker, M. S. Kim, and G. Milburn, *Spin Entanglement Witness for Quantum Gravity*, *Phys. Rev. Lett.* **119** (2017) 240401, arXiv:1707.06050 [quant-ph].
- [37] A. Belenchia, R. M. Wald, F. Giacomini, E. Castro-Ruiz, v. Brukner, and M. Aspelmeyer, *Quantum Superposition of Massive Objects and the Quantization of Gravity*, *Phys. Rev. D* **98** (2018) 126009, arXiv:1807.07015 [quant-ph].
- [38] A. Einstein, *Näherungsweise integration der feldgleichungen der gravitation*, *Sitzungsber. K. Preuss. Akad. Wiss.* **1** (1916) 688.
- [39] A. Einstein, *Über gravitationswellen*, *Sitzungsber. K. Preuss. Akad. Wiss.* **1** (1918) 154.

Bibliography

- [40] W. M. Farr, S. Stevenson, M. Coleman Miller, I. Mandel, B. Farr, and A. Vecchio, *Distinguishing Spin-Aligned and Isotropic Black Hole Populations With Gravitational Waves*, *Nature* **548** (2017) 426, arXiv:1706.01385 [astro-ph.HE].
- [41] **LIGO Scientific, Virgo** Collaboration, B. P. Abbott *et al.*, *Binary Black Hole Population Properties Inferred from the First and Second Observing Runs of Advanced LIGO and Advanced Virgo*, *Astrophys. J. Lett.* **882** (2019) L24, arXiv:1811.12940 [astro-ph.HE].
- [42] D. Gerosa and E. Berti, *Are merging black holes born from stellar collapse or previous mergers?*, *Phys. Rev. D* **95** (2017) 124046, arXiv:1703.06223 [gr-qc].
- [43] M. Zevin, C. Pankow, C. L. Rodriguez, L. Sampson, E. Chase, V. Kalogera, and F. A. Rasio, *Constraining Formation Models of Binary Black Holes with Gravitational-Wave Observations*, *Astrophys. J.* **846** (2017) 82, arXiv:1704.07379 [astro-ph.HE].
- [44] C. Caprini and D. G. Figueroa, *Cosmological Backgrounds of Gravitational Waves*, *Class. Quant. Grav.* **35** (2018) 163001, arXiv:1801.04268 [astro-ph.CO].
- [45] S. Hild *et al.*, *Sensitivity Studies for Third-Generation Gravitational Wave Observatories*, *Class. Quant. Grav.* **28** (2011) 094013, arXiv:1012.0908 [gr-qc].
- [46] **LIGO Scientific** Collaboration, B. P. Abbott *et al.*, *Exploring the Sensitivity of Next Generation Gravitational Wave Detectors*, *Class. Quant. Grav.* **34** (2017) 044001, arXiv:1607.08697 [astro-ph.IM].
- [47] J. A. Sidles and D. Sigg, *Optical torques in suspended Fabry–Perot interferometers*, *Phys. Lett. A* **354** (2006) 167–172.
- [48] J. Aasi *et al.*, *Advanced LIGO*, *Classical and Quantum Gravity* **32** (Mar, 2015) 074001.
- [49] F. Acernese *et al.*, *The advanced virgo detector*, *Journal of Physics: Conference Series* **610** (May, 2015) 012014.
- [50] K. Somiya, *Detector configuration of KAGRA—the japanese cryogenic gravitational-wave detector*, *Classical and Quantum Gravity* **29** (Jun, 2012) 124007.
- [51] D. Carney, A. Hook, Z. Liu, J. M. Taylor, and Y. Zhao, *Ultralight dark matter detection with mechanical quantum sensors*, *New J. Phys.* **23** (2021) 023041, arXiv:1908.04797 [hep-ph].

- [52] F. Monteiro, G. Afek, D. Carney, G. Krnjaic, J. Wang, and D. C. Moore, *Search for composite dark matter with optically levitated sensors*, *Phys. Rev. Lett.* **125** (2020) 181102, arXiv:2007.12067 [hep-ex].
- [53] Y. Michimura, T. Fujita, S. Morisaki, H. Nakatsuka, and I. Obata, *Ultralight vector dark matter search with auxiliary length channels of gravitational wave detectors*, *Phys. Rev. D* **102** (2020) 102001, arXiv:2008.02482 [hep-ph].
- [54] S. Morisaki, T. Fujita, Y. Michimura, H. Nakatsuka, and I. Obata, *Improved sensitivity of interferometric gravitational wave detectors to ultralight vector dark matter from the finite light-traveling time*, *Phys. Rev. D* **103** (2021) L051702, arXiv:2011.03589 [hep-ph].
- [55] J. Manley, M. D. Chowdhury, D. Grin, S. Singh, and D. J. Wilson, *Searching for vector dark matter with an optomechanical accelerometer*, *Phys. Rev. Lett.* **126** (2021) 061301, arXiv:2007.04899 [quant-ph].
- [56] K. Nagano, H. Nakatsuka, S. Morisaki, T. Fujita, Y. Michimura, and I. Obata, *Axion dark matter search using arm cavity transmitted beams of gravitational wave detectors*, *Phys. Rev. D* **104** (2021) 062008, arXiv:2106.06800 [hep-ph].
- [57] Y. Levin, *Internal thermal noise in the LIGO test masses: A Direct approach*, *Phys. Rev. D* **57** (1998) 659–663, arXiv:gr-qc/9707013.
- [58] F. Bondu, P. Hello, and J. Y. Vinet, *Thermal noise in mirrors of interferometric gravitational wave antennas*, *Phys. Lett. A* **246** (1998) 227–236.
- [59] G. M. Harry *et al.*, *Thermal noise in interferometric gravitational wave detectors due to dielectric optical coatings*, *Class. Quant. Grav.* **19** (2002) 897–918, arXiv:gr-qc/0109073.
- [60] P. R. Saulson, *Thermal noise in mechanical experiments*, *Phys. Rev. D* **42** (1990) 2437–2445.
- [61] W. Marshall, C. Simon, R. Penrose, and D. Bouwmeester, *Towards quantum superpositions of a mirror*, *Phys. Rev. Lett.* **91** (2003) 130401, arXiv:quant-ph/0210001.
- [62] H. Müller-Ebhardt, H. Rehbein, R. Schnabel, K. Danzmann, and Y. Chen, *Entanglement of macroscopic test masses and the Standard Quantum Limit in laser interferometry*, *Phys. Rev. Lett.* **100** (2008) 013601, arXiv:quant-ph/0702258.

- [63] M. Bailes *et al.*, *Ground-Based Gravitational-Wave Astronomy in Australia: 2019 White Paper*, arXiv:1912.06305 [astro-ph.IM].
- [64] K. Goda, O. Miyakawa, E. E. Mikhailov, S. Saraf, R. Adhikari, K. McKenzie, R. Ward, S. Vass, A. J. Weinstein, and N. Mavalvala, *A Quantum-Enhanced Prototype Gravitational-Wave Detector*, *Nature Phys.* **4** (2008) 472–476, arXiv:0802.4118 [quant-ph].
- [65] **LIGO Scientific** Collaboration, J. Abadie *et al.*, *A Gravitational wave observatory operating beyond the quantum shot-noise limit: Squeezed light in application*, *Nature Phys.* **7** (2011) 962–965, arXiv:1109.2295 [quant-ph].
- [66] **LIGO Scientific** Collaboration, J. Aasi *et al.*, *Enhancing the sensitivity of the LIGO gravitational wave detector by using squeezed states of light*, *Nature Photon.* **7** (2013) 613–619, arXiv:1310.0383 [quant-ph].
- [67] **LIGO Scientific** Collaboration, H. Yu *et al.*, *Quantum correlations between light and the kilogram-mass mirrors of LIGO*, *Nature* **583** (2020) 43–47, arXiv:2002.01519 [quant-ph].
- [68] **Virgo** Collaboration, F. Acernese *et al.*, *Quantum Backaction on kg-Scale Mirrors: Observation of Radiation Pressure Noise in the Advanced Virgo Detector*, *Phys. Rev. Lett.* **125** (2020) 131101.
- [69] N. Matsumoto, M. Sugawara, S. Suzuki, N. Abe, K. Komori, Y. Michimura, Y. Aso, S. B. Cataño Lopez, and K. Edamatsu, *Demonstration of displacement sensing of a mg-scale pendulum for mm- and mg- scale gravity measurements*, *Phys. Rev. Lett.* **122** (2019) 071101, arXiv:1809.05081 [quant-ph].
- [70] A. Pontin, M. Bonaldi, A. Borrielli, L. Marconi, F. Marino, G. Pandraud, G. A. Prodi, P. M. Sarro, E. Serra, and F. Marin, *Quantum nondemolition measurement of optical field fluctuations by optomechanical interaction*, *Phys. Rev. A* **97** (2018) 033833, arXiv:1611.00917 [quant-ph].
- [71] N. Matsumoto, Y. Michimura, G. Hayase, Y. Aso, and K. Tsubono, *Classical Pendulum Feels Quantum Back-Action*, *Phys. Rev. A* **92** (2015) 033825, arXiv:1312.5031 [quant-ph].
- [72] N. Matsumoto, Y. Michimura, Y. Aso, and K. Tsubono, *An optically trapped mirror for reaching the standard quantum limit*, *Opt. Express* **22** (2014) 2915, arXiv:1405.4906 [physics.optics].

- [73] K. Komori, Y. Enomoto, C. P. Ooi, Y. Miyazaki, N. Matsumoto, V. Sudhir, Y. Michimura, and M. Ando, *Attonewton-meter torque sensing with a macroscopic optomechanical torsion pendulum*, *Phys. Rev. A* **101** (2020) 011802, arXiv:1907.13139 [quant-ph].
- [74] S. Sakata, O. Miyakawa, A. Nishizawa, H. Ishizaki, and S. Kawamura, *Measurement of angular antispring effect in optical cavity by radiation pressure*, *Phys. Rev. D* **81** (2010) 064023.
- [75] T. Corbitt, C. Wipf, T. Bodiya, D. Ottaway, D. Sigg, N. Smith, S. Whitcomb, and N. Mavalvala, *Optical Dilution and Feedback Cooling of a Gram-Scale Oscillator to 6.9 mK*, *Phys. Rev. Lett.* **99** (2007) 160801.
- [76] A. R. Neben, T. P. Bodiya, C. Wipf, E. Oelker, T. Corbitt, and N. Mavalvala, *Structural thermal noise in gram-scale mirror oscillators*, *New J. Phys.* **14** (2012) .
- [77] **LIGO Scientific** Collaboration, B. Abbott *et al.*, *Observation of a kilogram-scale oscillator near its quantum ground state*, *New J. Phys.* **11** (2009) 073032.
- [78] J. Chan, T. P. M. Alegre, A. H. Safavi-Naeini, J. T. Hill, A. Krause, S. Gröblacher, M. Aspelmeyer, and O. Painter, *Laser cooling of a nanomechanical oscillator into its quantum ground state*, *Nature* **478** (2011) 89–92.
- [79] J. D. Teufel, T. Donner, D. Li, J. W. Harlow, M. S. Allman, K. Cicak, A. J. Sirois, J. D. Whittaker, K. W. Lehnert, and R. W. Simmonds, *Sideband cooling of micromechanical motion to the quantum ground state*, *Nature* **475** (2011) 359–363.
- [80] R. W. Peterson, T. P. Purdy, N. S. Kampel, R. W. Andrews, P. L. Yu, K. W. Lehnert, and C. A. Regal, *Laser Cooling of a Micromechanical Membrane to the Quantum Backaction Limit*, *Phys. Rev. Lett.* **116** (2016) 063601.
- [81] D. Kelley, J. Lough, F. Mangaña Sandoval, A. Perreca, and S. W. Ballmer, *Observation of photo-thermal feed-back in a stable dual-carrier optical spring*, *Phys. Rev. D* **92** (2015) 062003, arXiv:1507.02979 [physics.optics].
- [82] E. Hirose, K. Kawabe, D. Sigg, R. Adhikari, and P. R. Saulson, *Angular instability due to radiation pressure in the LIGO gravitational wave detector*, *Appl. Opt.* **49** (2010) 3474, arXiv:0909.0010 [gr-qc].
- [83] L. Barsotti, M. Evans, and P. Fritschel, *Alignment sensing and control in advanced LIGO*, *Class. Quant. Grav.* **27** (2010) 084026.

Bibliography

- [84] Y. Enomoto, K. Nagano, M. Nakano, A. Furusawa, and S. Kawamura, *Observation of reduction of radiation-pressure-induced rotational anti-spring effect on a 23 mg mirror in a Fabry-Perot cavity*, *Class. Quant. Grav.* **33** (2016) 145002.
- [85] K. Nagano, Y. Enomoto, M. Nakano, A. Furusawa, and S. Kawamura, *Mitigation of radiation-pressure-induced angular instability of a Fabry-Perot cavity consisting of suspended mirrors*, *Phys. Lett. A* **380** (2016) 3871–3875.
- [86] K. Komori, *Optomechanical Torsion Pendulum for Measurement of Quantum Radiation Pressure Fluctuation*. PhD thesis, University of Tokyo, 2019.
- [87] C. M. Caves and B. L. Schumaker, *New formalism for two-photon quantum optics. 1. Quadrature phases and squeezed states*, *Phys. Rev. A* **31** (1985) 3068–3092.
- [88] B. L. Schumaker and C. M. Caves, *New formalism for two-photon quantum optics. 2. Mathematical foundation and compact notation*, *Phys. Rev. A* **31** (1985) 3093–3111.
- [89] T. Corbitt, Y. Chen, and N. Mavalvala, *Mathematical framework for simulation of quantum fields in complex interferometers using the two-photon formalism*, *Phys. Rev. A* **72** (2005) 013818, arXiv:quant-ph/0502088.
- [90] T. Kawasaki, K. Komori, H. Fujimoto, Y. Michimura, and M. Ando, *Angular trapping of a linear-cavity mirror with an optical torsional spring*, arXiv:2110.13507 [quant-ph].
- [91] L. Barsotti and M. Evans, “Modeling of alignment sensing and control for advanced ligo.” Ligo-t0900511-v4 section 3, 2009.
- [92] K. Komori, T. Kawasaki, S. Otabe, Y. Enomoto, Y. Michimura, and M. Ando, *Improving force sensitivity by amplitude measurements of light reflected from a detuned optomechanical cavity*, *Phys. Rev. A* **104** (2021) L031501, arXiv:2105.10510 [quant-ph].
- [93] G. H. Fett, *Feedback Control Systems*. Prentice Hall, 1954.